Università degli studi di Roma

"La Sapienza"

"Vito Volterra" Doctoral School in Astronomical, Chemical, Earth, Mathematical and Physical Sciences

Fluid-rock interactions and their implications on carbonate reservoir characterization.

A dissertation in

Geologia del Petrolio (GEO/03),

presented by

Roberta Ruggieri

Submitted to the Department of Earth Science

in fulfilment of the requirements

for the degree of

Doctor of Philosophy.

Rome

March 2021

Fluid-rock interactions and their implications on carbonate reservoir characterization.

PhD Thesis Sapienza – University of Rome

Author’s email: Roberta.ruggieri@uniroma1.it

The dissertation of Roberta Ruggieri was reviewed and approved by:

Prof. Fabio Trippetta
Associate Professor of Structural Geology
Department of Earth Sciences
Sapienza University of Rome, Italy
Dissertation Advisor

Prof. Fabrizio Balsamo
Associate Professor of Structural Geology
Department of Chemistry, Life Sciences and Environmental Sustainability
University of Parma, Italy
External Reviewer

Prof. Andrea Luigi Paolo Bistacchi
Associate Professor of Structural Geology
Department of Earth and Environmental Sciences
University of Milano-Bicocca, Italy
External Reviewer

Abstract

The objective of my research has been to define the interactions between fluid and rock properties at different environmental conditions and observation scale to reduce the uncertainty in the carbonate reservoir characterization.

Here, I integrate field observations, subsurface data, petrophysical and frictional laboratory measurements focusing on carbonate-bearing rocks to better constrain factors controlling fluid-rock interactions with applications to active petroleum systems. In particular, I focus on the Burano-Bolognano carbonate petroleum system that extends from the northern sector of the Majella mountain to the Cigno/Vallecupa oil fields, in Abruzzo Region (Central Italy).

This area is of particular interest because of the following reasons:

- It has received great attention by oil companies in the past for its structural, stratigraphic, and geodynamic evolution, which led it to be an important target for hydrocarbon exploration during the past century. For this reason, it is characterized by a public dense dataset of wells, reports, maps, etc.
- It allows to study all petroleum system elements (with the exception of the source rock), such as: reservoir, seal, traps, and migration pathways at field scale.
- It allows to understand the influence of subsurface fluids on the petrophysical properties of carbonate reservoir rocks since the outcropping portions of reservoir interval are both clean and hydrocarbon-saturated. This allows measuring and comparing the variations of petrophysical properties between hydrocarbon-bearing and hydrocarbon-free samples.
- It is regarded as an analogue of a faulted and fractured reservoir for other carbonate petroleum systems worldwide and in particular in the Adriatic area.

The results of my research quantify the influence of fluid properties in changing of the petrophysical and frictional properties of the bearing-carbonate rocks. The presence of viscous fluids, such as heavy hydrocarbons, at ambient temperature defines an increase of the wave velocities respect to those of the unsaturated samples and determines a possible strengthening and stiffening of the reservoir rock. With increasing temperature, distinct downward trends are recorded, especially for the P-wave velocities. Moreover, the presence of fluids along faults promotes a slow slip behaviour, which was more marked with the presence of clay minerals along fault surface.

Finally, starting from these results, I simulate the evolution of the Burano-Bolognano petroleum system and the related fluids movements, inferring that within this petroleum system the vertically hydrocarbon migration is driven by fractures/faults and the subsequently lateral migration determinates a gradual oil biodegradation with an increase of its density.

Riassunto

L'obiettivo della mia ricerca di dottorato è stato quello di investigare le interazioni tra le proprietà del fluido e della roccia a diverse condizioni e scale di osservazione al fine di ridurre l'incertezza nella caratterizzazione di un sistema petrolifero impostato in litologia carbonatica.
Nel presente lavoro integro osservazioni condotte sul campo, dati del sottosuolo, misure di laboratorio per la caratterizzazione delle proprietà petrofisiche e di attrito, condotte su rocce carbonatiche per meglio vincolare i fattori che controllano le interazioni tra fluido-roccia con applicazioni ai sistemi petroliferi attivi. In particolare, mi concentro sul sistema petrolifero carbonatico, denominato Burano-Bolognano, che si estende dal settore settentrionale della montagna della Majella ai giacimenti petroliferi, più a nord, di Cigno e Vallecupa, nella regione Abruzzo (in Italia centrale).
Questa zona è di particolare interesse per i seguenti motivi:

- In passato ha ricevuto grande attenzione da parte delle compagnie petrolifere per la sua evoluzione strutturale, stratigrafica e geodinamica, che l'hanno portata ad essere un importante obiettivo per l'esplorazione di idrocarburi nel secolo scorso. Per questo motivo è caratterizzata da un denso dataset pubblico di pozzi, relazioni, mappe, ecc.
- Consente di studiare tutti gli elementi di un sistema petrolifero (ad eccezione della roccia madre), come serbatoio, seal, trappole e percorsi di migrazione su scala dell'affioramento.
- Permette di studiare l'influenza dei fluidi del sottosuolo sulle proprietà petrofisiche delle rocce del reservoir carbonatico poiché quest'ultimo affiora in porzioni sia pulite che sature di idrocarburi. Ciò, quindi, consente di misurare e confrontare le variazioni delle proprietà petrofisiche tra campioni impregnati di idrocarburi e campioni senza idrocarburi.
- La Majella rappresenta un analogo esumato di un giacimento, caratterizzato anche da faglie e fratture, per altri sistemi petroliferi impostati in litologie carbonatiche presenti in tutto il mondo e in particolare nell'area adriatica.

I risultati della mia ricerca definiscono l'influenza delle proprietà dei fluidi sul cambiamento delle proprietà petrofisiche e di attrito delle rocce carbonatiche. La presenza di fluidi viscosi, come gli idrocarburi pesanti, determina un aumento delle velocità delle onde rispetto a quelle dei campioni insaturi e determina un possibile rinforzo e irrigidimento della roccia a temperatura ambiente.

Con l'aumento della temperatura, invece, sono registrati differenti diminuzione della velocità delle onde acustiche, in modo particolare per le velocità dell'onda P.

D'altra parte, ho osservato che la presenza di fluidi nelle zone di faglia definisce uno scivolamento lento e continuo, che risulta essere più marcato dalla presenza di minerali argillosi lungo la superficie della faglia.

Infine, partendo da questi risultati, effettuo una simulazione dell'evoluzione del sistema petrolifero Burano-Bolognano e la relativa migrazione dei fluidi, osservando che all'interno del sistema petrolifero studiato la migrazione degli idrocarburi è principalmente verticale e guidata da fratture, mentre la successiva migrazione laterale determina una graduale biodegradazione dell'olio con un aumento della densità dell'olio dai campi petroliferi di Cigno e Vallecupa a gli idrocarburi affioranti sulla montagna della Majella.

Preface

The present dissertation is submitted for the degree of Doctor of Philosophy at the University of Rome, Sapienza. This project is a result of collaborations with the Sapienza Department of Earth Sciences, INGV (Istituto Nazionale di Geofisica e Vulcanologia) and ENI oil company.

Overall, this research addresses to improve the carbonate reservoir characterization by characterizing the influence of fluid properties on reservoir rocks, especially when the infilling material is a heavy hydrocarbon. To this aim, I conducted an accurate characterization of the petrophysical properties and the interactions between reservoir carbonate rocks and fluids. Then, I built three-dimensional static and two-dimensional dynamic reservoir models improving the knowledge about the geological evolution of the petroleum system and the related movements of fluids.

The work is organized in three chapters and four appendices. Before getting into the details, I provide a general introduction on the central topic of this research. Then, I present the research objectives with the most relevant implications of this project. In the successive chapters, I outline methods, results, and analysis of the detailed scientific studies, which have already presented or submitted in the following publications:

- Ruggieri, R., & Trippetta, F. (2020). *Petrophysical properties variation of bitumen-bearing carbonates at increasing temperatures from laboratory to model*. Geophysics, 85(5), 1-52.

- Ruggieri, R., Scuderi, M. M., Tinti, E., Trippetta, F., Collettini, C., Brignoli, M., Mantica, S., Petroselli, S., Osculati, L. & Volonté, G. (2021). *The role of shale content and pore-water saturation on frictional properties of simulated carbonate faults*. Tectonophysics (in press).

- Trippetta, F., Ruggieri, R., Brandano, M., & Giorgetti, C. (2020). *Petrophysical properties of heavy oil-bearing carbonate rocks and their implications on petroleum system evolution: Insights from the Majella Massif*. Marine and Petroleum Geology, 111, 350-362.

- Lipparini, L., Trippetta, F., Ruggieri, R., Brandano, M., & Romi, A. (2018). *Oil distribution in outcropping carbonate-ramp reservoirs (Maiella Mountain, Central Italy): Three-dimensional models constrained by dense historical well data and laboratory measurements.* AAPG Bulletin, 102(7), 1273-1298.

The manuscript on the development of three-dimensional regional static and two-dimensional dynamic models of the Burano-Bolognano petroleum system in the Abruzzo Region, that extends from the norther sector of the Majella Mountain to the Cigno/Vallecupa oil fields, is currently being prepared for submission:

- Ruggieri R., Trippetta F., *Quantitative dynamic modelling of an active carbonate-bearing petroleum system constrained by subsurface, outcrop and laboratory data*. (In preparation)

TABLE OF CONTENTS

Introduction

A "*Petroleum System"* is a geologic system that encompasses the hydrocarbon source rocks and all related oil and gas reserves, and which includes all of the geologic elements and processes that are essential if a hydrocarbon accumulation is to exist (Magoon and Dow, 1994). A petroleum system model is a reconstruction of the space-time history at reservoir to basin scales that aims to understand and predict the interrelated processes and elements, , preferably through 3D representation of geological data (Hantschel and Kauerauf, 2009).

The Petroleum System Modelling (PSM) could be thus used as a predictive tool to evaluate and understand the evolution of a petroleum system, as well as a key tool in the exploration risk assessment for all essential elements (source, reservoir, seal and overburden rocks) and processes (trap formation, and hydrocarbon generation and accumulation) of the petroleum system. PSM uses forward deterministic computations to simulate the thermal histories of the rocks and the related generation, migration, and accumulation of hydrocarbons, that are modelled from past to present using inferred starting conditions such as the reservoir characteristics (Peters et al., 2012).

Reservoir characterization is an essential process to construct the best possible quantitative representation of a reservoir incorporating all the characteristics of petroleum system rocks. For this reason, reservoir characterization is based on the integration of different data derived by several disciplines, including geology, geophysics, petrophysics, and petroleum engineering. Moreover, an accurate reservoir characterization is a key step in developing, monitoring, and managing reservoir and optimizing production. However, the construction of a complete PSM requires the integration and coupling of at least two basic models: static and dynamic. In the modelling exercise, it is then useful to start by providing a simple model of reservoir at a given time point, known as "static model".

A static reservoir study typically involves four main stages (Cosentino, 2001):

1. *Structural modelling*
2. *Stratigraphic modelling*
3. *Lithological modelling*
4. *Petrophysical modelling*

Briefly, during the first stage a geometrical and structural reservoir models are constructed from reservoir to regional scale by defining a map of the reservoir's structural top and by interpreting the faults within a reservoir. Subsequently, a depositional scenario is determined using the well data, and a certain number of lithological types (basic facies) are defined based on lithologic, sedimentologic and petrophysical properties. At the last stage, when the geometrical and structural reservoir models are developed, the volume of reservoir model is described by a spatial distribution of the petrophysical properties, such as porosity, fluid saturation, density, permeability, and acoustic response. Among them, porosity and permeability are two most important properties of reservoir rocks. Porosity is a measure of the potential storage volume of hydrocarbons and permeability is a measure of the ease with which fluids can flow through reservoir rocks. These properties are influenced by primary features, such as mineral composition of the host rock, fabric, diagenetic processes, burial (Croizé et al., 2010; Hairabian et al., 2014; Smeraglia et al., 2014) and any secondary features, such as faults, fractures, stylolites (Agosta et al., 2007; Baud et al., 2016; Cilona et al., 2012; Heap et al., 2019; Lavenu et al., 2014; Michie and Haines, 2016; Rustichelli et al., 2016) and by the presence of an infilling materials (Nicolas et al., 2016) that may have been introduced during the whole diagenetic and tectonic history of the reservoir rock. In particular, laboratory experiments on core plugs show that the presence of infilling fluids influences the fracturing mode through physical and chemical interactions with matrix (e.g., dissolution), the mechanical processes, including fault slip behaviour (De Paola et al., 2009; Mao et al., 2009; Ruggieri et al., under review) and the petrophysical properties of rocks (Smeraglia et al., 2014; Trippetta et al., 2013, 2020; Brandano et al., 2020; Ruggieri and Trippetta, 2020). This highlights the importance of an accurate reservoir characterization on both clean and fluid-filled rocks.

The complete characterization of the reservoir petrophysical properties thus represents on one hand the final stage of the static modelling and on the other hand the basis for the dynamic description of fluid-rock interactions (Lucia, 2007). Laboratory experimental measurements on core plugs are consequently a fruitful tool to characterize the fluid properties in order to reduce the uncertainty about reservoir identification and to constrain the hydrocarbon migration within reservoir system.

Fluid-flow simulation is then employed to derive the dynamical properties of a given hydrocarbon reservoir that vary in space and time. In fact, in a petroleum system hydrocarbon, fluids migrate from the low porosity, fine-grained source rock, where they are generated, to higher porosity reservoir rocks, where they may form a highly concentrated hydrocarbon

accumulation (England et al., 1987). These hydrocarbon movements, defined as primary and secondary migration, respectively, are still under discussion and not very well understood. Moreover, the simulation case study for heavy oil is a challenge due to their high viscosity determining a different behaviour respect to light oil. Consequently, the study of the effect in fluid properties variation, such as oil viscosity and their interactions with reservoir rocks, is essential to improve the exploration and production of heavy oil reservoirs, as well as the assessment of exploration risk.

During the last decade, a broad attention is given at carbonate rocks to learn more about the characterization of reservoir properties and their variation due to the presence of infilling materials, such as heavy hydrocarbons. Conversely to sandstone reservoirs, which have been extensively studied due to the large presence of clastic reservoir filled by hydrocarbons all around the world (Aydin, 2000), carbonate reservoirs are still poorly understood. This is because carbonate reservoirs are generally characterized by high heterogeneities related to fabric, texture, fractures that usually characterize such type of reservoirs (Anselmetti et al., 1997; Anselmetti and Eberli, 1993; Cilona et al., 2012; Eberli et al., 2003; Rustichelli et al., 2016; Trippetta et al., 2013; Brandano et al., 2020).

Notwithstanding the key role of the petrophysical properties in reservoir characterization, these properties of hydrocarbon-filled reservoirs are far less known, in particular when the infilling material is represented by heavy oil. Therefore, an accurate study of the petrophysical properties of heavy oil-bearing carbonates is particularly relevant to improve exploration and production of these reserves because the estimated volume of technically recoverable heavy oil and natural bitumen in known accumulations is about equal to the Earth's remaining conventional (light) oil reserves (Meyer and Attanasi, 2007). Additionally, carbonate reservoirs contain about 60% of the world's oil reserves (Sayers, 2008). This caused growing interest in carbonate reservoirs in the last years. Moreover, cases of induced seismicity have been documented along carbonate faults during modern energy production worldwide, i.e., in southern Italy in Val D'Agri oil field (Improta et al., 2017), in Oklahoma (e.g. Keranen et al., 2014) and in Canada (Eyre et al., 2019). Therefore, understanding what type of slip behaviour will be generated upon fault reactivation, whether the fault will fail by earthquake rupture, by accelerated but slow shear slip, or by aseismic creep is one of the primary objectives to mitigate the seismic risk associated to underground fluid injection during production (Scuderi and Collettini, 2018). To answer these questions, frictional properties, such as strength, stability, and healing (ensemble of re-strengthening processes that

occur after slip) should be characterized performing friction tests on fault gouges at different boundary conditions. In addition, it is well known that the permeability of fault zone depends on structural architecture of the fault itself and on the petrophysical properties of fault-related rocks. Thus, the analysis of fault systems is a crucial issue in reservoir characterization and modelling of fluid flow behaviour (e.g., Balsamo and Storti, 2010; Bistacchi et al., 2020). The presence of faults within reservoir has implications in understanding how hydrocarbons can migrate into the reservoir because fault zones can behave either as hydraulic seal, leading to the identification of possible different reservoir levels (Caine et al., 1996), or as conduits, where porous volumes are connected and fluids are drained along high-permeability corridors (Moretti, 1998; Géraud et al., 2006). On the other hand, several geological field observations have documented that in mature carbonate fault zones it is possible to observe the presence of clay patches (Tesei et al., 2013; Smeraglia et al., 2017; Collettini et al., 2019) that influence the fault-rock mechanical properties, such as slip behaviour and permeability (Faulkner and Rutter, 2003). As mentioned above, permeability is a key property in the petrophysical characterization and in fluid flow simulation and, it also depends on textural and hydraulic properties of the pore network, such as pore size distribution, pore shape, and tortuosity as well as heterogeneities such as faults (Lucia, 2007; Balsamo and Storti, 2010).

In this project, I had the opportunity to conduct an accurate study of the petrophysical properties and their influence in fluid flow behaviour on both bearing-carbonate rocks and their infilling material in the heavy-oil state that were directly collected from the reservoir intervals outcropping at subsurface, in central Italy. The research activities have been focused on the Majella reservoir, which offers the unique opportunity to study outcropping porous carbonate reservoir portions both clean and filled by heavy-oil overlaid by marly levels that act as seal (Agosta et al., 2009; Scrocca et al., 2013; Iadanza et al., 2015; Brandano et al., 2016; Lipparini et al., 2018). Thus, the carbonate system outcropping in the Majella mountain allows the direct investigation of elements, such as reservoir and seal rocks together with geological processes, such as tertiary migration due to the geologically recent exhumation and erosion (Bigi et al., 2013; Ghisetti and Vezzani, 2002; Masini et al., 2011; Patacca et al., 2008; Vezzani et al., 2010). Bearing in mind that outcrop analogues have a fundamental role in hydrocarbon exploration and reservoir modelling to reduce the distance between seismic and well log/core scales, the Majella reservoir represents a very useful exhumed analogue for larger carbonate-bearing petroleum systems in central Italy and all around the world.

Thesis Objectives and Implications

The present thesis strives to integrate field observations, subsurface data and petrophysical laboratory measurements focusing on carbonate-bearing rocks to better constrain factors controlling fluid-rock interactions within an onshore petroleum system in Abruzzo Region. To achieve this goal, I need to: (a) make detailed estimates of the properties of the subsurface fluids (e.g., viscosity, density) and the petrophysical properties of rocks which contain them (e.g., porosity, permeability, acoustic response, saturation); (b) develop an accurate geological/geophysical reservoir model. I worked extending the three-dimensional reservoir model towards a regional scale and investigating on the correlation between fluid properties and their relative migrations through the development of two-dimensional fluid-flow simulations.

However, from a broad point of view, this project aims to define the coupling effects of petrophysical and mechanical properties of reservoir rocks and fluid properties at reservoir scale. The assessment of how fluid properties, presence of structural heterogeneities (i.e., fractures and faults) can influence the evolution of a petroleum system, from a hydrocarbon generation within the source rock to the entrapment of hydrocarbons into the reservoir rocks, is the specific goal of this research. The study of the fluid-rock interactions has numerous scientific and industrial applications, for instance:

(1) earthquake field, because fluids play a key role in the faulting processes and during the seismic activities (i.e., induced seismicity);

(2) oil and gas field. Fluid properties are of economic interest in petroleum exploration and in controlling hydrocarbons migration within the petroleum system during production.

Over these three years of research, I have planned and executed several consecutive works, from classical geological correlation works based on well data, to field observations and laboratory measurements on core plugs, to advanced three-dimensional modelling and simulation exercises, through the use of dedicated software, such as Petrel and PetroMod, both trademarks of Schlumberger.

Thesis Overview

The thesis begins with an introduction to make a good starting point for the reading of the next chapters. It is a broad overview on the most important topics at which this project results aims to contribute, such as reservoir characterization, petrophysical modelling and fluid flow simulations. Then it is followed by three chapters in which I present the scientific results of my PhD project. In Appendices I report supplementary materials of details about the research and the list of all experiments. The chapters of this thesis are described as follows.

In Chapter 1, I experimentally investigate the role of hydrocarbons in changing the petrophysical properties of rocks by merging laboratory measurements, outcrops characterization, and subsurface data focusing on a carbonate-bearing reservoir (Bolognano Formation) of the Majella mountain, in central Italy. Firstly, I have carried out density and viscosity measurements of the residual bitumen, extracted by HCl dissolution of the carbonate hosting rock. Then, I have characterized in the laboratory density, porosity, compressive strength, Young's modulus, Poisson's ratio, and acoustic response of both clean and heavy oil-bearing carbonate rocks of the Bolognano Formation as a function of pressure and temperature. In this chapter, I propose a theoretical model to estimate the P-wave velocity at different conditions of temperature, porosity, and bitumen content. Moreover, I also have analyzed several structural scanlines in the northern flank of the Majella (Central Italy) area to compare with laboratory results at larger scale data.

In Chapter 2, I explore the role of increasing shale content on the frictional properties of simulated carbonate faults under room-dry and $CaCO_3$-pore fluid conditions since faults can likely across carbonate reservoirs and can experience induced seismicity during the modern energy production. The role of clay content in the frictional properties of the calcite-shale rich faults is of particular interest since numerous faults cut across sedimentary sequences, composed of carbonates and clay rich sediments. Therefore, heterogeneous fault zone structure, consisting of thick portions dominated by clay lithologies, and principal slipping zones formed within carbonate has been invoked to be responsible for weak faults and to produce a complex slip behaviour. In these experiments, I have conducted velocity-stepping tests (0.1-300 μm/s) and slide-hold-slide tests (30-3000 s of hold) to evaluate how various amounts of clay influence frictional stability and frictional healing, respectively. In addition, I have collected post experimental gouge samples for microstructural investigations to link mechanical with microstructural data. On the basis of experimentally dataset, I provide a possible explanation

of the complex slip behaviour of carbonate-bearing faults due to the presence of clay mineral..

In Chapter 3, I present the development of three-dimensional geological model of the petroleum system in onshore Abruzzo region, by merging well data, subsurface observations, and laboratory measurements. This petroleum system, that I named the Burano-Bolognano petroleum system, extends from the northern sector of the Majella mountain to the Cigno and Vallecupa oil fields, located about 10 km NNW from the Majella.. Starting from the geological/geophysical model, I simulate the fluid flow which takes place in an interconnected grid of porous spaces within reservoir rocks for the Burano-Bolognano petroleum system. Moreover, I analyze the influence of fluid properties, i.e., density, on fluid flow behaviour and I constrain the time of the hydrocarbon migration within reservoir rocks. Finally, on the basis of simulation models, performed with PetroMod, I propose a conceptual model through which I hypothesize how the Burano-Bolognano petroleum system has worked during geological times, knowing the actual hydrocarbon distributions.

At the end of the thesis, I present a summary of the final conclusions and recommendations of this research project.

In Appendices A, B and C auxiliary materials are available for each chapter in order to provide to the reader with an exhaustive dataset derived from this research.
Finally, Appendix D is the complete list of the measurements and experiments that I performed during my PhD at the HP-HT Laboratory of INGV, in Rome.

Chapter 1

Petrophysical properties of heavy oil-bearing carbonate rocks: insights of the Majella Mountain

Abstract

The study of the petrophysical properties of reservoir rocks is one of the most important goal in reservoir characterization allowing to understand and reduce uncertainty in reservoir modelling. Thus, in this Chapter I outline the role of hydrocarbons in changing the petrophysical properties of rocks focusing on a carbonate-bearing reservoir (Bolognano Formation) of the Majella mountain. I have characterized in the laboratory density, porosity, compressive strength, Young's modulus, and Poisson's ratio of both clean and heavy oil-bearing samples at increasing confining pressure and the acoustic response with increasing temperature. Moreover, I have conducted density and viscosity measurements on the residual Heavy Hydrocarbon (HHC), extracted by HCl dissolution of the hosting carbonate rock. Laboratory data show that porosity and the presence of HHCs within the samples affect seismic waves velocity. In particular, Vp and the derived dynamic Young's modulus generally decrease with increasing porosity for clean samples and, for a fixed porosity, tend to increase with the presence of heavy-oil. Cyclic loading-unloading experiments show that the average compressive strength is 25 MPa and 38 MPa and average static Young's modulus are 5.7 GPa and 9.9 GPa, for clean and HHC-bearing samples, respectively. Then, acoustic velocity data point out an inverse relationship with temperature and exhibit a distinct trend with increasing temperature depending on the amount of HHC content. I also propose a theoretical model to predict the P-wave velocity change at different initial porosities for HHC-saturated samples, suggesting that the velocity change is mainly related to the absolute volume of HHC. These laboratory data have been integrated with field work, consisting in measuring fracture orientation in 11 outcrops of the same lithology. The field data show that both heavy oil-bearing and clean outcrops are characterized by two main trends (NW-SE and NNE-SSW) and heavy-oil-bearing outcrops are much less fractured than clean outcrops.

1.1 Heavy oil and bitumen as new hydrocarbon reserves

Unconventional oils, like heavy oil and bitumen, are emerging as an alternative hydrocarbon reserve since conventional oil is depleting nowadays. As for conventional oil, acoustic surveys represent the most important methodologies used in heavy oil exploration, in reservoir characterization and in recovery processes monitoring (Lines et al., 2005a; Javanbakhti et al., 2018). Heavy oils are defined as having high density, high viscosity, and API gravity less than 10° (Schmitt, 1999; Hinkle and Batzle, 2006; Han et al., 2006; Meyer et al., 2007). These physical properties are strongly temperature dependent as well as the physical properties of rocks hosting heavy oils (Chopra et al., 2010; Javanbakhti et al., 2018). Therefore, bitumen, as the most viscous hydrocarbon, is in a solid state at room temperature and softens quickly when heated. Since variations in seismic properties of a reservoir can be directly correlated to fluid changes (Adam et al., 2009), an accurate study of modifications in the petrophysical properties of HHC-bearing rocks as a function of temperature is particularly relevant for a better interpretation of seismic data. Acoustic laboratory measurements on core plugs are of fundamental help in establishing the relationships between different physical properties of bitumen and hosting rocks, which in turn enhance reservoir characterization and hydrocarbon recovery. Therefore, the understanding of the petrophysical processes that acted in hydrocarbon-filled rocks and their effect on the reservoir mechanical properties is of great interest in petroleum geology for both scientific and industrial fields.

Numerous laboratory investigations have been performed in literature on heavy oil and heavy oil mixed with typically unconsolidated sand (e.g., Tosaya et al., 1987; Wang and Nur, 1988; Batzle et al., 2006; Han et al., 2006, 2007, 2008; Kato et al., 2008; Wolf, 2010; Yuan et al., 2015a; Li et al., 2016), and report both P- and S-wave velocities as function of temperature, pressure, and frequency. Tosaya et al. (1987) and Wang and Nur (1988) perform laboratory experiments on several heavy oils and tar sand samples, demonstrating that the seismic velocity and attenuation are temperature dependent. Batzle et al. (2006) and Han et al. (2006) investigate the influence of viscosity and temperature on the seismic properties of heavy oil samples, defining different temperatures at three fluid states: glass, quasi-solid and liquid. Li et al. (2016) conducted acoustic measurements on heavy oil-saturated sand samples and heavy oil itself, showing that the elastic properties of heavy oil sands are strongly correlated to the properties of heavy oil itself, which in turn is influenced by temperature and pressure conditions.

Other laboratory measurements have been also conducted on bitumen saturated carbonates (e.g., Rabbani et al., 2014, 2016; Chen et al., 2015a; Yuan et al., 2015b, 2017, 2018). However, a full characterization of hydrocarbon-filled carbonate reservoirs is still far to be completed due to the high heterogeneity that characterizes this type of rocks. Moreover, Yuan et al. (2018) point out that, to correctly assess the influence of bitumen on acoustic properties it is necessary to compare the properties of the carbonate samples with and without bitumen. To make this comparison, hence, normally bitumen-saturated samples are cleaned to directly investigate the properties of clean carbonate samples. However, the cleaning procedure is seldom completely efficient and some remaining bitumen in pore space can affect the results (Yuan et al., 2018).

Instead of using artificially cleaned samples, in this research I benefit of a set of samples that outcrops naturally in saturated and unsaturated conditions. The investigated carbonate samples naturally exhibit several heavy hydrocarbons saturation degrees, allowing a detailed analysis on acoustic response of hydrocarbon-filled carbonate rocks. I have been thus able to compare the petrophysical properties of natural hydrocarbon-bearing carbonates and hydrocarbon-free samples, collected from the same depositional facies. These samples were collected in the northern flank of the Majella mountain (in central Italy), where several oil seeps of asphalt and bitumen (HHC) crop out (Figure 2.1) within the Bolognano Fm (Brandano et al., 2016; Lipparini et al., 2018). Here, I investigated how the petrophysical properties of the HHC-bearing carbonate samples are influenced by the presence of heavy-oil at increasing temperature and confining pressure.

With this aim, I completely characterized the physical properties of residual HHC, extracted by dissolution of the hosted carbonate rocks and the acoustic properties of HHC-bearing carbonate samples. Then, I developed a theoretical model which can be a useful tool for geophysical research to anticipate and/or understand a change in seismic response of carbonate reservoir at different conditions of temperature, porosity, and hydrocarbon saturation and, thus, determinate an adequate interpretation of seismic sections. I tested P-wave velocity model over the entire temperature range at different initial porosity, HHC content and/or saturation. Finally, I combined laboratory measurements, field observations, and subsurface data in order to constrain the role of hydrocarbons in changing the petrophysical properties of rocks and to apply these results at the scale of the entire petroleum system.

1.2 Geological setting

The Majella mountain is a N–S/NW–SE oriented thrust-related anticline, located in the Central Apennine. It records a carbonate succession from Upper Jurassic to Miocene, topped by siliciclastic sediments of Messinian to early Pleistocene age (Donzelli, 1968; Crescenti et al., 1969). The evolution of the Oligo-Miocene ramp ended with the Messinian event of the Mediterranean Basin, which resulted in the deposition of an effective regional seal interval such as evaporites, marls and evaporitic carbonates (Crescenti et al., 1969). Starting from Early Pliocene the Majella area was then involved in the foredeep deformation of the Apennine orogen (e.g. Cosentino et al., 2010; Scisciani et al., 2002). According to previous studies, the current structural elevation of the Majella massif, almost 3000 above sea level, was reached only in the latest stages of orogen-related deformation, during early Pleistocene, possibly due to a strong uplift passively produced by the growth of a deeper-seated back-thrust located in the footwall of the Majella basal thrust (Patacca et al., 2008). Other authors (Masini et al., 2011) proposed that the Majella Mountain structure resulted from Messinian–Early Pliocene extension and subsequent Late Pliocene shortening.

The study area is the northern sector of the Majella mountain and here most of the faults strike primarily northwest (Figure 1.1), showing mainly pure normal displacements, with some oblique-slip normal faults recognized (Agosta et al., 2010). The individual structures are up to a few kilometres long and are characterized by apparent displacements on the order of tens of meters (Giorgioni et al., 2011).

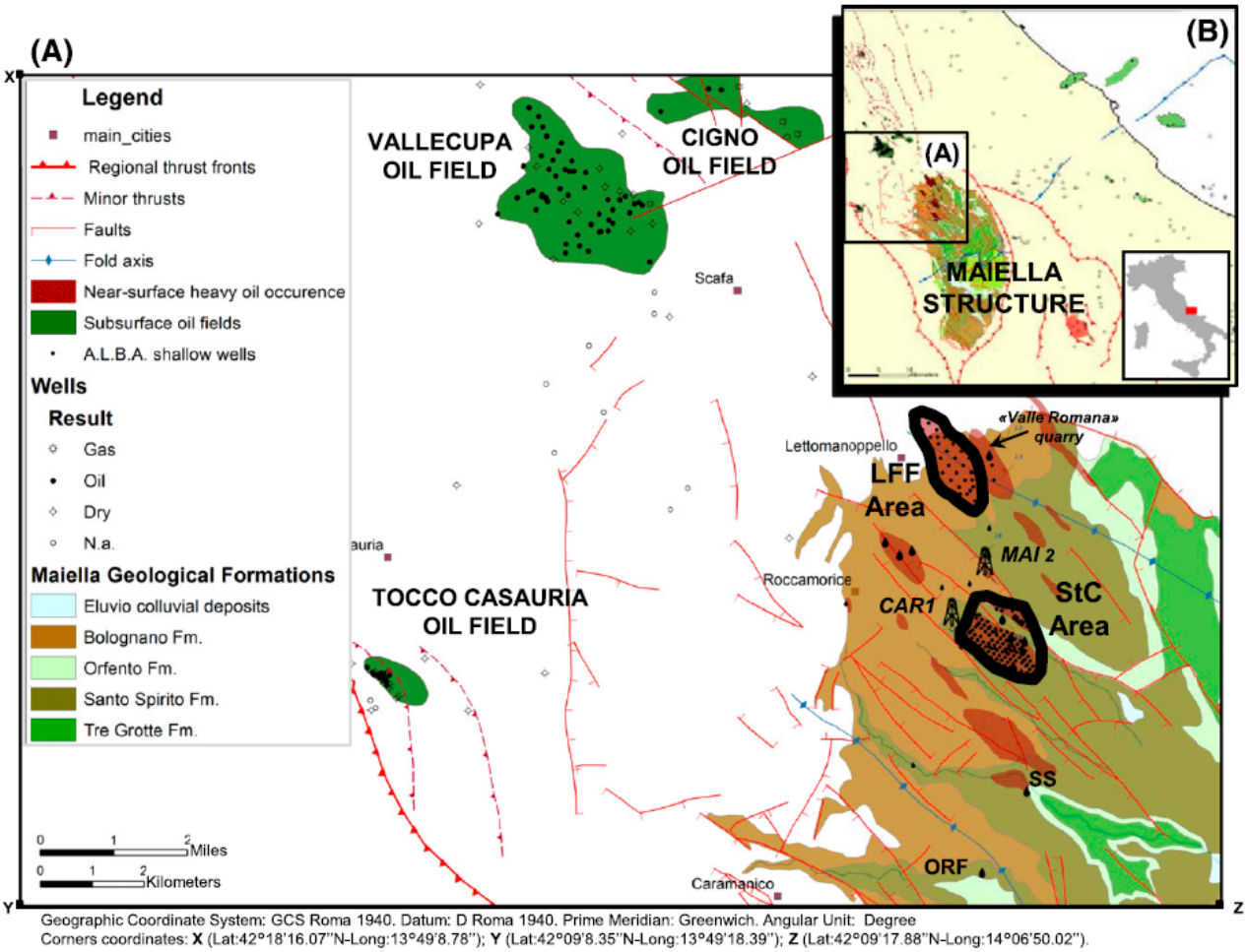

Figure 1.1: *(A) Study area and hydrocarbon occurrences in the subsurface (in green) and near surface (in brown), including the oil-bearing outcrops of the northwestern flank of the Majella structure. Surface geology and main tectonic elements are reported after Vezzani and Ghisetti (1998), and subsurface maps are reported after Visibility of Petroleum Exploration Data in Italy Project (2012). The two key areas investigated by Azienda Lavorazione Bitumi Asfalti (ALBA) historical drilling over the northwestern flank of the Majella are highlighted by the dense wells pattern (black dots) and indicated as Lettomanoppello–Fonte di Papa–Fonticelle (LFF) area and Sterparo–Cerratina (StC) area. (B) Regional view, showing the whole Majella structure (in colour), the main Apenninic related thrusts (in red), and the main hydrocarbon fields known in the area, both onshore and offshore. Geographic reference coordinate system and corner coordinates are reported at the bottom.*

From the petroleum geology perspective, the northern sector of the Majella structure is particularly interesting because several seeps of asphalts and bitumens can be found at surface (Figure 1.2a, b), mainly associated to the Bolognano Fm, but locally also within the older reservoirs of the Santo Spirito (Eocene) and Orfento (Upper Cretaceous) Formations (Scrocca et al., 2013). In the past, these near-surface hydrocarbon accumulations have been extensively

investigated and exploited in historical time, until the beginning of twentieth century, through a board mining system. Then, during the 1960 exploitation from this area was stopped and with the new modern exploration efforts started to investigate deeper preserved sub-surface structures. These new exploration efforts led to some midsize discoveries of oil-bearing Bolognano carbonates, such as in the Tocco Casauria, Vallecupa, and Cigno oil fields (Figure 1.1), now depleted and abandoned (Visibility of Petroleum Exploration Data in Italy Project, 2012). In more recent years, some additional oil accumulations within the Bolognano reservoirs were discovered also to belong to a wider petroleum system that extends also in adjoining onshore Abruzzo and Molise regions and offshore areas in the Central Adriatic Sea, such as Ombrina Mare and Katia oil fields (Mattavelli and Novelli, 1990; Zappaterra, 1994; Cazzini et al., 2015; Scrocca et al., 2013).

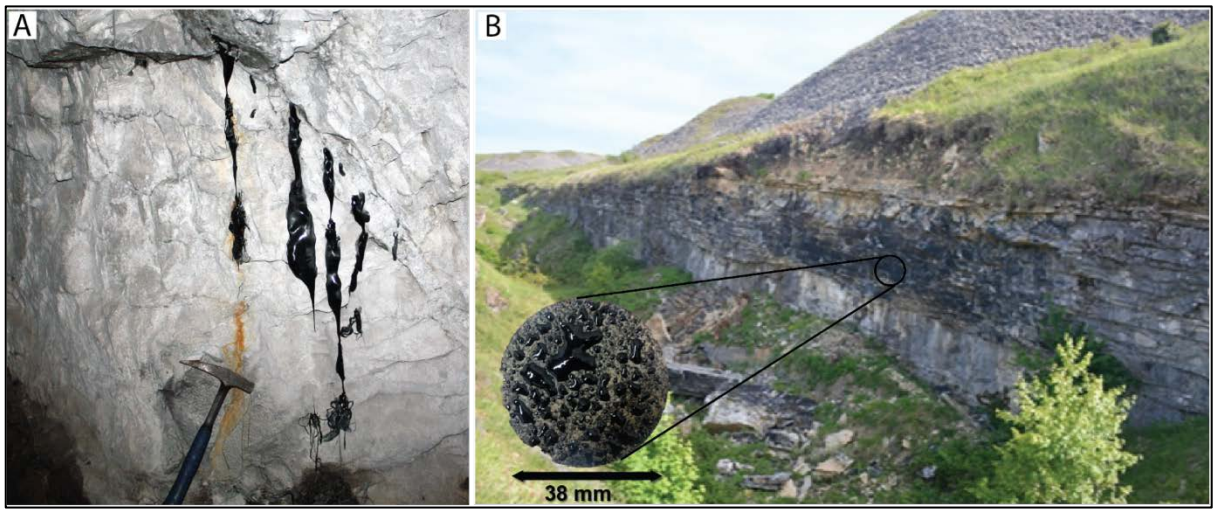

***Figure 1.2**: Evidences of seeps of asphalts and bitumens found at surface along the NW flank of the Majella. (A) Example of the leaked bitumen from fractures in a tunnel of the mining site. (B) Outcrop of the bitumen-bearing Bolognano Formation in historical and abandoned exploitation site, known as 'Acquafredda'. I reported a detail of the bitumen-bearing core plug sample collected from the outcrop.*

From the sedimentological perspective, the Bolognano Fm are characterized by carbonate ramp shallow water deposits developed during the Oligo-Miocene (Chattian to early Messinian) and this formation is made up by fragments of larger benthic foraminifera and other bioclastic fragments, such as echinoids, red algae, mollusks (Brandano et al., 2016). These foraminifera and bioclastic fragments determinate grain-supported levels with a low content of mud and silt fraction alternating with marls and marly limestones. Consequently, the Bolognano Fm represents the main reservoir interval of the whole area with a well-connected high primary porosity and the marly levels act as intermediate seals (Brandano et al., 2013). Particularly, in

the Bolognano Fm several authors are recognized five different lithofacies associations, as reported in Table 1.1 (Crescenti et al., 1969; Mutti and Bernoulli, 2003; Brandano et al., 2013, 2016).

Lithofacies associations of the Bolognano fm	Interval Time	Thickness (m)	Main Charcateristics
Lithothamnium limestone	Tortonian to early Messinian	35-50	Tight interval or fractured reservoir
Hemipelagic marls (Orbulina marls)	Late Burdigalian to Serravallian	60-100	Intermediate seal
Lepidocyclina Calcarenite 2 or upper bryozoan limestone	Late Aquitanian to Burdigalian	40-80	Upper reservoir
Cherty hemipelagic marly Limestone	Late Chattian to Aquitanian	5-20	Low-porosity interval
Lepidocyclina Calcarenites 1 or lower bryozoan limestone	Late Rupelian to Chattian	15-25	Lower reservoir

Table 1.1*: Summary Stratigraphic Succession. Nomenclature and main reservoir intervals are indicated, including interval thickness and geological age, following both Mutti and Bernoulli (2003) and Brandano et al., (2016). Porosities are derived from integrating laboratory measurements, porosity-derived three-dimensional models, and the available well composite logs and reports in the study area.*

The basal unit is represented by ***Lepidocyclina Calcarenites 1*** (late Rupelian to Chattian in age), a carbonate ramp deposits with a constant thickness of approximately 20 m in the studied area. It is characterized by porosity between 8 and 25% and in this unit little manifestations of hydrocarbons are presented. It is also called *lower bryozoan lmst*, following Mutti and Bernoulli, (2003). This lower reservoir interval is overlaid by bioturbated, bioclastic planktonic foraminiferal marly limestones, called ***Cherty hemipelagic marly Limestone*** (late Chattian to Aquitanian in age) with a thickness ranging between 5 and 20 m. Even if it is characterized by very low to zero hydrocarbon saturation, it does not appear to act as an effective seal within the hydrocarbon-bearing column. In the exploration wells, drilled about 10 kilometres to the NW (Vallecupa and Cigno Oil fields), this thin interval is not recognized, either because it is not distinguishable by logs or because it is absent. This interval is overlaid by another cross-bedded unit, the ***Lepidocyclina Calcarenite 2*** (late Aquitanian to Burdigalian in age) that shows similar compositional and sedimentologic characters of the basal *Lepidocyclina Calcarenites 1*. This unit represents the upper reservoir interval with a thickness from 40 to 80 m and it is characterized by high porosity, spanning between 9 and 28% resulted almost connected from laboratory measurements. This interval is also known in literature as "*upper bryozoan lmst*" (Mutti and Bernoulli, 2003). Above this main reservoir interval of the studied area, a seal interval was recognized, called ***Hemipelagic marls*** (late Burdigalian to Serravallian in age)

with a thickness of 60-100 m. This interval is described by literature as made of "*hemipelagic marls*", with remnants of Pectins and Echinoids. This unit is known also as *Orbulina marls* (Mutti and Bernoulli 2003). In the subsurface to the NW, this unit is known either as "Roiano" (in the "Vallecupa" field) or "Orte" (in the "Cigno" and "Tocco Casauria" oil fields) marls, with quite homogeneous constant thickness reported of about 90 m. Along most of the NW flank of the Majella, field observations and historical data confirm its effective sealing capacities, but in the Vallecupa and Cigno oil fields its sealing capacities can be destroyed by fracturing, allowing hydrocarbons to migrate upward into the above ***Lithothamnium limestone*** (Tortonian to early Messinian in age). This last shallow water unit consists of up to 30 m of limestones to marly limestones with abundant red algal nodules. In the studied area, this unit represents a completely dry interval, likely due to its very low porosities. Whereas it can be a reservoir of interest when showing secondary porosity enhancement by natural fractures in the "Cigno" and "Vallecupa" oil fields. Here, this unit is reported to represent a productive reservoir with porosities of about 7% due to fractures and also it is equivalent to what has been called either the "Orte" (in the "Alanno" oil field) or "Tocco" (in the "Cigno" and "Tocco Casauria" oil fields) marly limestone interval, with thickness between 35 and 50 meters.

However, in the NW sector of the Majella mountain the Lepidocyclina limestone unit is of particular interest because within this interval wide bitumen impregnations are found at the outcrop scale. This interval, mainly Lepidocyclina limestone 2, is characterized by both high primary and secondary porosity that is mostly connected as showed by laboratory measurements.

1.3 Material and methods

1.3.1 Investigated Materials

During the field work I collected large blocks strictly pertaining to the Lepidocyclina calcarenite 2 in the NW sector of the Majella Mountain (Figure 1.3). Two groups of this unit samples were investigated:

- Clean rocks (without heavy-oil)
- Heavy Hydrocarbon (HHC)-bearing rocks with different saturations.

From large blocks I have prepared a total of 46 sub-core cylindrical samples with dimensions of 38 mm in diameter and from 38 to 90 mm in length, with their end faces ground flat and parallel to better than ±0.02 mm. The investigated facies (Lepidocyclina calcarenite 2) of the Bolognano fm were tested both perpendicular and parallel to bedding, however no laminations have been observed as confirmed by thin section analyses. Around 30 thin sections (Figure 1.4 a, b) have been prepared with blue methylene to recognize the microfacies, estimate the initial and residual porosity and the HHC saturation degree by image analysis.

Thin section analysis (Figure 1.4) highlights a general composition dominated by coarse-grained skeletal debris and a texture ranging from grainstones to packstones. The skeletal components are represented mainly by lepidocyclina specimens (Nephrolepidina and Eulepidina) together with celleporid bryozoans and echinoid plates. Accessory components are serpulid fragments, mollusk fragments, and small benthic and planktonic foraminifers. Matrix is generally scarce and consists of calcisiltite. The main cements are represented by calcite microspar infilling primary interparticle pores, blocky spar in intraskeletal pores and secondary mouldic pores. Syntaxial cement is common and overgrows on echinoid plates (Figure 1.4a, b) (Brandano et al., 2016). The analyzed thin sections show, thus, that most of the sampled reservoir is made by coarse-grained bioclastic grainstones and packstones, with both inter- and intra-granular primary porosity recognized mostly connected. Moreover, no diffused micro-fractures are observed, with very few exceptions. It is worth noting that clean (Figure 1.4a) and HHC-bearing (Figure 1.4b) are characterized by identical features in terms of bioclasts, cements and type of pores, excluding any possible differential weathering effect. The only difference is the presence of a variable content of heavy hydrocarbons.

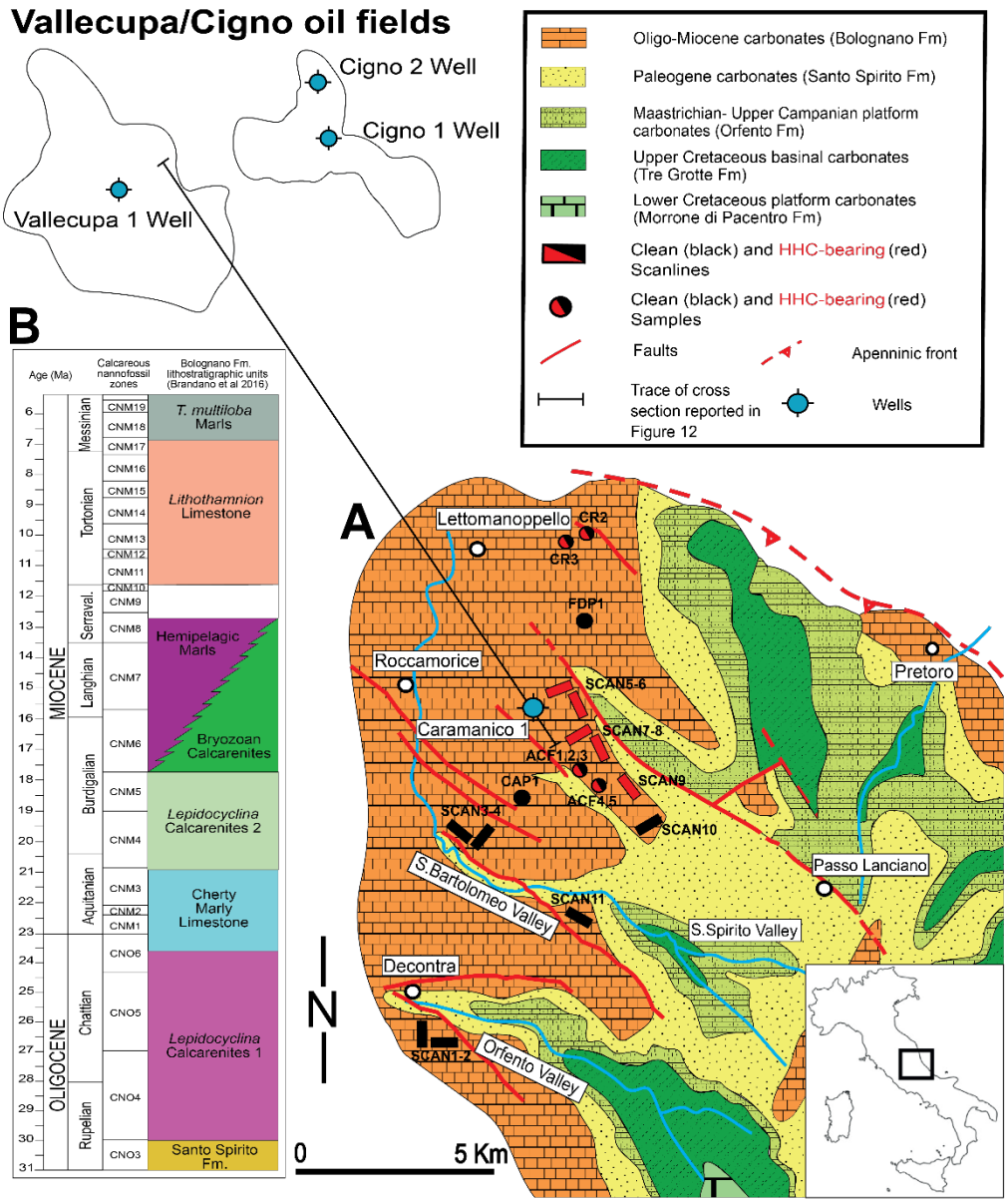

***Figure 1.3**: (A) Geological map of the Majella mountain with highlighted sampling points. (B) Detailed chronostratigraphy and lithostratigraphy of the Bolognano Fm (modified after Brandano et al., 2016).*

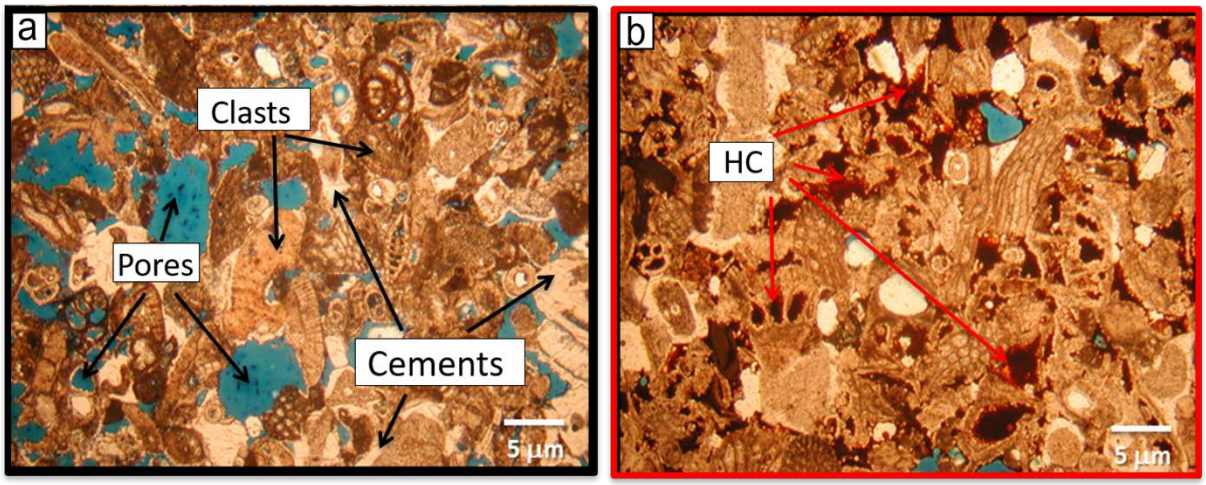

***Figure 1.4**: Thin sections of Lepidocyclina calcarenite 2 are representative microstructures of the tested materials. (a) clean sample showing a bioclastic grainstone with evident inter- and intra-skeletal pores, and syntaxial cement developed on echinoid plates and spines; (b) hydrocarbon bearing sample showing the same assemblage of clean sample with pores filled by hydrocarbon in form of heavy-oil.*

1.3.2 Laboratory methodology

The petrophysical properties of the collected large bitumen-bearing blocks of the Bolognano Fm were investigated at HP-HT laboratory of the Istituto Nazionale di Geofisica e Vulcanologia (INGV), in Rome. A petrophysical characterization was initially performed at ambient pressure and temperature on all samples that had been dried in an oven at 30° C for a minimum of 24h. This modest temperature allowed to avoid any possibility of thermal cracking and HHC leakage prior to the measurements.

Each sample was characterized in terms of density and porosity by using a helium pycnometer (AccuPyc II 1340). This instrument allows to measure volume of intact and pulverized samples with the accuracy of ± 0.001%. The bulk density was calculated as dry weight/volume ratio of the intact sample, the grain density was defined as weight/volume ratio of the matrix obtained pulverized the samples by hand and the connected porosity was calculated by dividing the difference between geometrical volume (V_g) of the sample, measured by using precision caliper, and the volume measured by pycnometer (V_{pyc}) with the geometrical volume (V_g), following the equation:

$$Effective\ Porosity = \left(\frac{V_g - V_{pyc}}{V_g}\right) 100 \qquad (1.1)$$

The total porosity is calculated as:

$$Total\ Porosity = \left(\frac{{}^{w_{tp}}/_{\rho_{bulk}} - Vol_p}{{}^{w_{tp}}/_{\rho_{bulk}}}\right)100 \quad (1.2)$$

where w_{tp} and Vol_p are the weight and the volume of the powder, and ρ_{bulk} is the bulk density (defined as the weight of the sample divided by its total volume), while non-effective porosity can by calculated as the difference between total porosity and effective porosity.

Elastic wave velocity measurements were made axially on dry samples. A 900 V pulse generator was used to excite a 1 MHz resonant frequency piezoelectric transmitting transducer (on the top of the sample for signal emission). The waves, propagated through the sample, were captured using an identical receiving transducer (on the bottom of the sample for signal reception). After preamplification, signals were displayed and recorded on a digital storage oscilloscope (Figure SA.1 in Appendix A). For the instrument limitations, I investigated individually the influence of the confining pressure and temperature on compressional and shear wave velocity.

On 18 core samples, I investigated how temperature affects compressional- and shear-wave velocities. At the end of the initial petrophysical characterization of these samples (porosity and density measurements), a small hole (~3.5 mm in diameter) has been drilled in the center of the top of nine samples intended for temperature measurements allowing to introduce the thermocouple (Figure 1.5a)

For reproducibility and comparison purposes, all samples followed the same experimental procedure in both acoustic velocity and temperature measurements. This procedure is characterized by the subsequent steps:

1. All samples were first jacketed with polyolefin heat-shrink and sealed using plastic strip (Figure 1.5b).
2. Samples were heated in an oven at maximum temperature of 90° C for 48 hours to facilitate the HHC heating without HHC leakage.
3. Samples were removed from the oven and the first acoustic velocity measurement was recorded immediately once sample was positioned between the two piezoelectric transducers.
4. P- and S- wave velocities were digitally recorded at pre-set time intervals that started when sample was removed from the oven (reference time). Then, the time intervals were set up with progressive increments: 1 minute for the first nine acoustic velocity

measurements, 2 minutes for the following six measurements, 5 minutes for the next five measurements and 10 minutes for the last three ones.

The temperature measurements were recorded simultaneously with the acoustic velocities by using a K-type thermocouple. The thermocouple consists of two metal conductors: one is a nickel-chromium positive conductor and the another is a nickel-aluminum negative conductor. At laboratory conditions, the decreasing temperature was acquired automatically at a frequency of 1 Hz for about sixty minutes after the reference time. Since the reference time was the same for the acoustic velocities and the temperature measurements and assuming the same behaviour for the two samples, I have been able to plot temperature against acoustic waves for each couple-samples.

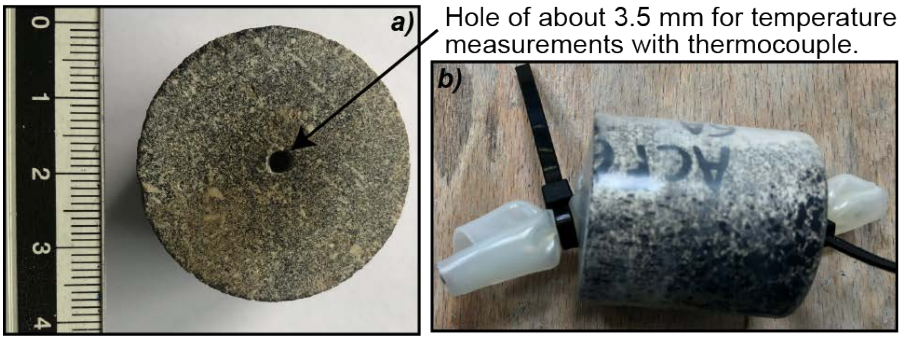

Figure 1.5: *An example of HHC-bearing carbonate sample investigated in this study. a) Cylindrical specimen with a small hole (~3.5 mm in diameter) drilled in the center of the top of 9 samples for temperature measurements. b) Example of specimen were jacketed with polyolefin heat-shrink, sealed using plastic strip and heated in an oven at maximum temperature of 90° C for 48 hours for both acoustic velocity and temperature measurements.*

Since the presence of HHC as an infilling material influences the petrophysical properties of hosting carbonate rocks, the physical properties of HHC were primarily characterized. Therefore, I carried out density and viscosity measurements on residual HHC samples, which were extracted from HHC-bearing rocks after HCl dissolution of the carbonate matrix (Figure 1.6a, b). Density was obtained by dividing the mass of HHC with its volume, measured by using the helium pycnometer at ambient conditions. Viscosity was determined using a rheometer AntonPaar Physica MCR301, equipped with parallel-plate geometry setup. This geometry is characterized by two plates (~ 2 mm in diameter): the lower plate is fixed and heated at the test temperature, while the upper plate can rotate. Since the investigated HHC was in a solid state, before of the viscosity measurement, I have heated the HHC sample at the same temperature at which viscosity was measured. After ten minutes, the heated HHC sample was removed from

the oven and was sandwiched in between the parallel plates. Once the lower plate had reached the test temperature, a rotational speed was applied and the viscosity measurements were performed in a wide range of the shear rates from 0.1 to 100 s^{-1}. These viscosity measurements were acquired at two temperatures (90° C and 110° C), which is further discussed below.

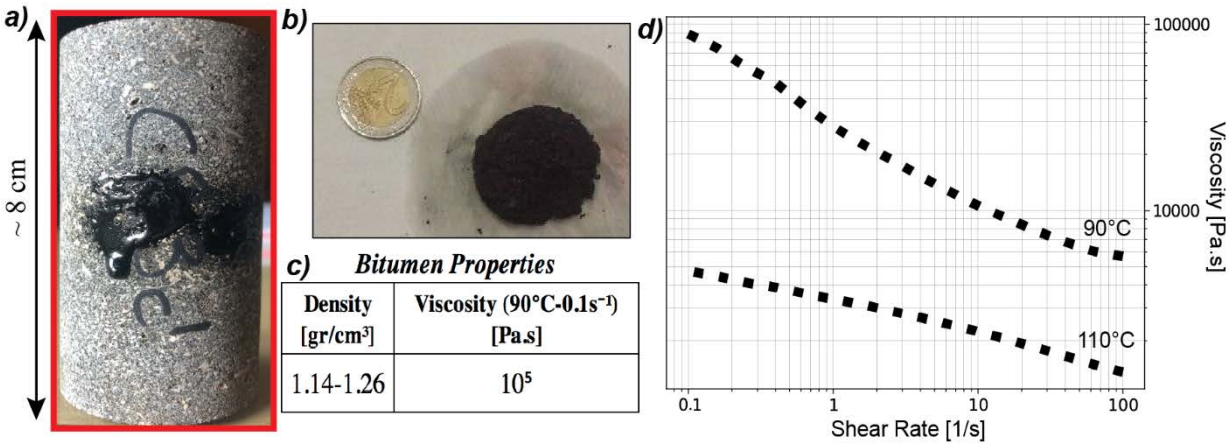

***Figure 1.6**: Physical and rheological properties of the extracted Majella bitumen. a) An example of HHC-bearing carbonate sample with bitumen leakage. b) The residual bitumen extracted from HHC-rich plug after HCl dissolution of the carbonate matrix. c) Density and viscosity measurements for residual bitumen samples. d) Plot of viscosity measurements as a function of shear rate for two investigated temperatures (90° C and 110° C).*

On 22 samples I performed velocity measurements by using the servo-controlled permeameter, at ambient temperature and at increasing confining pressure, from ambient up to 100 MPa using silicone oil (Figure 1.7).

Finally, uniaxial compression tests were conducted on 6 cylindrical samples (38 mm in diameter and 90 mm in length), with a length: diameter larger than 2.5:1 (Paterson and Wong, 2005) in a servo-controlled deformation apparatus, BRAVA (Collettini et al., 2014b) (Figure 1.8). This apparatus is equipped with a 1.5 MN uniaxial load frame. The axial load is measured through a load cell with 0.03 kN accuracy. The axial displacement is controlled and measured through a LVDT sensor with 0.1 μm accuracy. Experiments were performed at room temperature. Loading and unloading cycles with increasing amplitude were imposed to the samples. Samples were first loaded to a maximum stress of 2 MPa at a constant strain rate of 7.0×10−6 s−1, and then unloaded at the same rate to 1 MPa. In each subsequent cycle the maximum stress was increased by ~ 5 MPa until failure occurred.

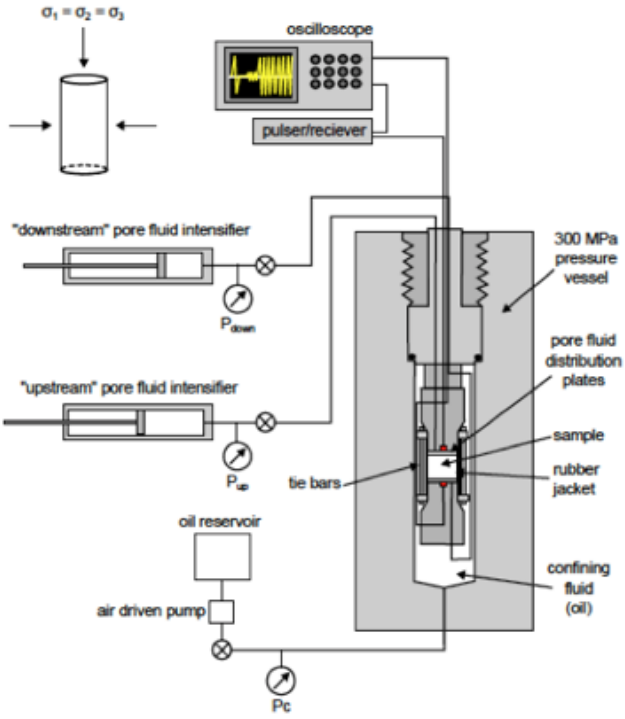

***Figure 1.7**: Schematic diagram of the servo-controlled permeameter (Heap et al., 2014) equipped with transducers for measurements of Vp, Vs and permeability up to confining pressures of 100 MPa. Standard sample size is 38 mm diameter by 38 mm long.*

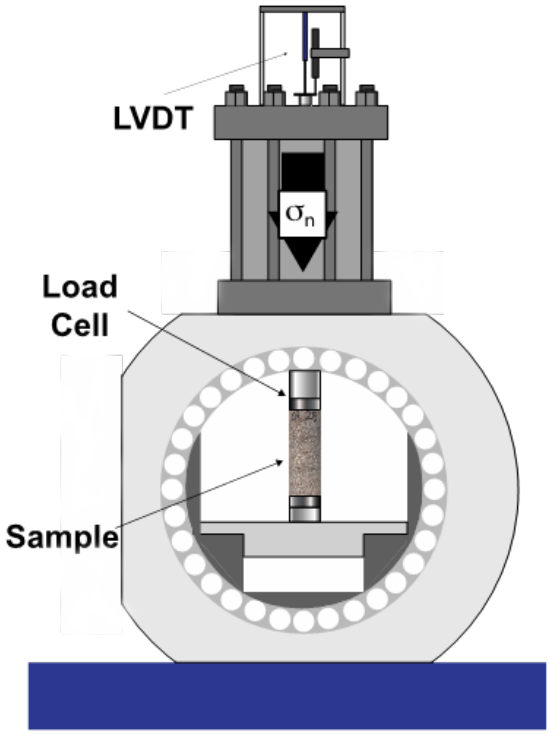

***Figure 1.8**: Schematic diagram of the BRAVA rock deformation apparatus (Collettini et al., 2014b) with uniaxial configuration. Standard sample size is 38 mm diameter by 90 mm long.*

1.4 Results

1.4.1 Bitumen characterization

Here I report results of the physical characterization of infilling HHC extracted after HCl dissolution of the carbonate matrix. Its measured values of density and viscosity are reported in Figure 1.7c. Measured density values go from 1.14 to 1.26 g/cm^3. From density measurements, I calculated the API (American Petroleum Institute) gravity for the investigated HHC that resulted to be ≤ -5°. These results are in agreement with those from Batzle et al. (2006), who measured similar density (1.12 g/cm^3) and the same API gravity (API= -5°) for extra-heavy oil samples from Texas oil field. For the extracted HHC, I also measured viscosity and it is reported in Figure 1.7d, against shear rate for the two investigated temperature (90° C and 110° C). For the limitation of the laboratory instrument, I performed viscosity measurements starting from 90° C, since below this temperature, HHC could not be placed on the lower plate of the rheometer due to its solid state. As expected, viscosity measurements depict a strong dependence with temperature (e.g., Zhao & Machel, 2012). Basically, an increasing temperature from 90° to 110 °C causes a reduction of one order of viscosity magnitude, from 8.89 x 10^4 to 4.74 x 10^3 Pa·s at the initial shear rate of 0.1 s^{-1}.

1.4.2 Sample characterization

Here I report results of the initial petrophysical characterization of all samples made at ambient pressure and temperature, listed in Tables 1.2-1.3-1.4. The investigated samples with HHC can be considered as a three-phase system, which is composed by matrix, HHC in a solid state and unfilled pores. The density (grain and bulk) and total porosity measurements of the cylindrical samples are summarized in Tables 1.2-1.3-1.4 for both HHC-bearing and clean samples. The rock grain density is very homogeneous for all the clean samples, resulting in 2.69 to 2.71 g/cm^3 (white squares in Figure 1.9), in good agreement with literature data for pure calcite rocks (Jaeger et al., 2007; Mavko et al., 2009; Gudmundsson, 2011). On the other hand, the grain density for HHC- bearing rocks varies between 2.43 and 2.67 g/cm^3 (gray squares in Figure 1.9), showing a clear effect of the bitumen in the powder. and these values are lower compared to the density of matrix for clean samples.

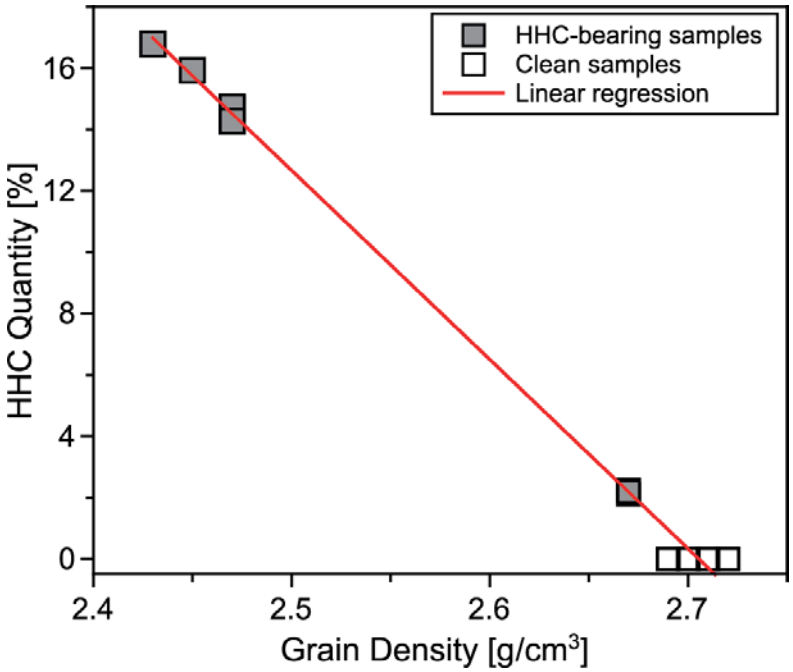

***Figure 1.9**: Relationship between bitumen content and grain density of the investigated samples. For clean samples (white squares), the grain density values span from 2.69 to 2.71 g/cm^3, whereas HHC-rich samples (gray squares) are characterized by a lower grain density (from 2.67 to 2.47 g/cm^3) proportionally to the amount of bitumen content.*

Total porosity (effective and non-effective porosity) evaluated with the pycnometer is in the range of 9–30.5% for clean samples and it is almost entirely effective porosity. Lower values have been measured for total porosity (8.1-19.27%) for HHC-bearing samples (Tables 1.2-1.3-1.4). The difference between clean and HHC-bearing samples is clearly related to the presence of an infilling material, i.e., bitumen (also highlighted by thin section analysis, Figure 1.4), that affects the porosity evaluation since HHC-filled pore space was measured by the pycnometer as part of the solid-matrix phase. In fact, the porosity evaluated by the pycnometer for HHC-bearing samples represents only the "residual porosity" being part of the original porosity filled by HHCs. HHC-bearing samples can be thus considered as a three-phase system, made of rock matrix, HHC-filled pores and unfilled pores, of which total volume, weight and density can be measured.

To understand the influence of HHC on the petrophysical properties, the original porosity and consequently, the HHC content were calculated for each HHC-bearing sample. By only considering the grain density, that is calculated from pulverized portions of samples, each sample becomes a two-phase system made of carbonate rock matrix and HHCs. Since the rock matrix for all samples is represented by pure calcite, the density of the carbonate-matrix portion

can be inferred from clean samples measurements (where it is almost constantly 2.71 g/cm^3). By measuring the density of the bitumen obtained by HHC-rich plugs after carbonate dissolution with HCl (1.14 g/cm^3), I could calculate the total HHC volume of each sample as follows.

Starting from the equation:

$$\rho_{mr} = (\rho_{mx} * \delta_{mx}) + (\rho_{HC} * \delta_{HC}) \quad (1.3)$$

being the portion of matrix $\delta_{mx} = (1 - \delta_{HC})$ and rearranging it derives that:

$$\delta_{HC} = \frac{(\rho_{mr} - \rho_{mx})}{(\rho_{HC} - \rho_{mx})} \quad (1.4)$$

where δ_{HC} is the portion (volume per unit, that goes from 0 to 1) of hydrocarbons respect to the pulverized part of the sample, while ρ_{mr} , ρ_{mx} and ρ_{HC} represent the measured grain density, the matrix density, and the bitumen density. Multiplying the obtained δ_{HC} by 100 I obtained the percentage of HC ($\delta_{HC\%}$) respect to the matrix. Being $\delta_{mx\%}$ the percentage of matrix respect to the total volume of the sample calculated as

$$\delta_{mx\%} = 100 - \text{Total porosity} \quad (1.5)$$

and by using the equation:

$$\delta_{HC\%} : 100 = \varphi_{HC} : \delta_{mx\%} \quad (1.6)$$

I obtained φ_{HC} that represents the porosity (expressed in percentage) filled by HCs. Then by summing the total porosity (the residual effective porosity plus the non-effective porosity) measured by the pycnometer with the calculated HC-filled porosity, I calculated the original total porosity of each sample (total corrected porosity) reported in Tables 1.3-1.4, following a very similar methodology respect to that reported by Lipparini et al. (2018) and Yuan et al. (2018). Consequently, the HHC content results in average values of 2.2% (low HHC-bearing samples) and 15% (high HHC-bearing samples) for the investigated samples. Thus, I calculated the original porosity of samples before the migration of HHC, which is obtained by summing measured porosity and HHC content (Tables 1.3-1.4). As expected, these values are in the highest range, between about 30% and 16%, and the samples with a lower value of grain density show a higher HHC content, reflecting a clear relationship between the measured grain density and HHC quantity, observed in Figure 1.9. Furthermore, data show that HHC content does not appear systematically correlated with porosity in the Bolognano samples. In fact, some collected samples (e.g., SSL2a and SSL2b in Table 1.2) are characterized by very high porosity

(up to 27%) without presence of HHC. Whereas bulk densities of HHC-bearing samples are from 2.06 to 2.34 g/cm^3 and corrected porosities are from 15.2 to 30.9% showing no relation with the quantity of HHCs. On the other hand, clean samples exhibit bulk densities in the range of 1.87–2.46 g/cm^3 and total porosities in the range of 9.3–30.5% where higher density corresponds linearly to lower porosity.

Properties of Clean Samples*

Sample	Bulk Density [g/cm³]	Grain Density [g/cm³]	Total Porosity [%]	HHC Content [%]	Vp [km/s]	Vs [km/s]	Vp /Vs
ACF2a	2.46	2.71	9.5	0	4.99	2.58	1.93
ACF2b	2.46	2.71	9.03	0	5.19	2.89	1.80
ACF3b	2.40	2.70	11.6	0	4.77	2.47	1.93
ACF4a'	2.40	2.70	11.6	0	4.56	2.35	1.94
ACF4b	2.41	2.70	11.1	0	4.76	2.45	1.94
ACF4c	2.38	2.70	12.1	0	4.40	2.25	1.96
FDP1a'	2.46	2.71	9.3	0	4.79	2.50	1.92
FDP1c'	2.25	2.71	11.75	0	4.33	2.27	1.91
CAP1d	2.26	2.71	16.6	0	4.12	2.09	1.97
SSL2a	1.99	2.70	27.0	0	3.46	1.81	1.91
SSL2b'	2.02	2.70	26.0	0	3.69	1.92	1.92
CB1c	2.12	2.70	25.20	0	3.59	1.82	1.97
CB3b	2.05	2.72	24.41	0	3.36	1.69	1.99
CR2c	1.87	2.69	30.5	0	3.24	1.64	1.98

Table 1.2: *Summary of the physical properties of the Bolognano samples. This table is related to the properties of the clean samples. I reported bulk and grain density, total porosity measured by using helium pycnometer, and the acoustic velocities recorded at ambient temperature and pressure during the pressurization cycle.*

Properties of HHC-Bearing Samples

Sample	Bulk Density [g/cm³]	Grain Density [g/cm³]	Total Porosity [%]	HHC content [%]	Total corrected Porosity [%]	At ambient Temperature Vp [km/s]	Vs [km/s]	Vp /Vs
ACF1-1	2.32	2.67	13.7	2.24	15.94	4.28	2.19	1.95
ACF1-2	2.29	2.67	14.22	2.23	16.45	4.44	2.28	1.95
ACF1-3	2.15	2.67	19.3	2.10	21.4	4.21	2.11	1.99
ACF1-5	2.29	2.67	13.72	2.20	15.92	4.79	2.43	1.97
CR1b	2.19	2.47	11.2	14.7	25.9	4.49	2.28	1.96
CR1c	2.19	2.47	11.0	14.7	25.7	4.11	2.04	2.01
CR1-2	2.13	2.47	13.7	14.3	28.0	4.43	2.25	1.97
CR3-1	2.18	2.45	11.09	15.94	27.0	3.98	2.01	1.98
CR3b	2.11	2.43	13.0	16.8	29.8	3.81	1.92	1.98

Table 1.3*: Summary of the physical properties of the Bolognano samples. This table is related to the properties of HHC-bearing samples on which I conducted velocity measurements at increasing temperature. I reported bulk and grain density, total porosity measured by using helium pycnometer, the back-calculated initial porosity for HHC-bearing samples starting from knowing of the HHC content in each sample and the acoustic velocities recorded at ambient temperature and pressure.*

Properties of HHC-Bearing Samples

Sample	**Bulk Density [g/cm³]**	**Grain Density [g/cm³]**	**Total porosity [%]**	**HHC Content [%]**	**Total Corrected Porosity [%]**	**Vp0 dw [km/s]**	**Vs0 dw [km/s]**	**Vp/Vs**	**E_{d0}** [GPa]	**ν_{d0}**
CR3a	2.09	2.48	16.4	14.3	30.6	3.94	2.18	1.81	25.4	0.28
CR3b	2.06	2.48	16.4	14.5	30.9	3.56	1.97	1.81	20.5	0.28
ACF5c"	2.28	2.48	8.1	13.9	22.1	4.46	2.30	1.94	31.7	0.32
ACF5a	2.26	2.48	8.7	13.7	22.3	4.44	2.27	1.95	30.9	0.32
ACF1f'	2.34	2.63	12.2	5.0	17.2	4.48	2.32	1.93	33.1	0.32
ACF1e'	2.26	2.63	15.3	5.1	20.4	4.26	2.24	1.91	29.6	0.31
ACF1c"	2.33	2.67	12.7	2.5	15.2	4.53	2.30	1.97	32.6	0.33
ACF1b'	2.31	2.67	14.0	2.5	16.6	4.56	2.36	1.93	33.9	0.32

Table 1.4*: Summary of the physical properties of HHC-bearing samples (Bolognano Fm), on which I conducted velocity measurements at increasing confining pressure. I reported bulk and grain density, total porosity measured by using helium pycnometer, the back-calculated initial porosity for HHC-bearing samples starting from knowing of the HHC content in each sample and the acoustic velocities recorded at ambient temperature and pressure.*

1.4.3 Temperature effect on velocity measurements at ambient pressure

Wave velocities are primarily affected by porosity (Anselmetti and Eberli, 1993; Eberli et al., 2003; Makvo et al., 2009; Trippetta and Geremia, 2019; Trippetta et al., 2020), so I firstly characterized this relation.

Axial P-wave (Vp) and S-wave (Vs) velocities, measured at ambient temperature and pressure, are listed in Tables 1.2-1.3. Figures 1.10a and 1.10b show the relationship of Vp and Vs with total porosity for both clean samples (white squares) and HHC-bearing samples (gray squares). The uncertainty of the recorded velocities is within the size of the markers reported in Figure 1.10. For clean samples, a linear inverse correlation is defined between acoustic velocities and porosity, and the best correlations of P- and S-wave velocities are given by:

$$V_p = -0.0817\phi + 5.6406 \quad (1.7)$$

and,

$$V_s = -0.0453\phi + 2.9764 \quad (1.8)$$

The investigated HHC-bearing samples are out of this trend, generally showing higher velocities with lower values of porosity, in agreement with previously published data (Yuan et al., 2018; Trippetta and Geremia, 2019; Trippetta et al., 2020). As highlighted in the above section (“Sample characterization”), the porosity measurements of HHC-bearing samples are influenced by the presence of the infilling hydrocarbon and therefore, in Figure 1.10, I corrected the porosity ofHHC-bearing samples with the original porosity. In this way, I can analyze the HHC influence only on velocity measurements.

Recorded velocities of HHC-bearing samples show a variation of Vp from 3.81 to 4.80 km/s and of Vs between 1.93 and 2.44 km/s at ambient temperature (Figures 1.10a and 1.10b). This suggests that porosity, rock texture and HHC within samples affect the wave velocities. Specifically, Vp and Vs decrease with increasing total porosity, whereas the presence of HHC generally defines an increasing in both velocities. In Figures 1.10c and 1.10d, I reported the velocity measurements on HHC-bearing samples as a function of total porosity at increasing temperatures from 25° to 70° and 90 °C. At temperature of 70° C, the measured Vp ranges from 3.69 to 4.70 km/s and Vs spans between 1.90 and 2.41 km/s. Increasing temperature up to 90 °C, Vp is in the range of 3.60 – 4.66 km/s, whereas Vs varies from 1.86 to 2.41 km/s. As a general trend, the measured Vp and Vs exhibit a reduction with increasing temperature from 25° to 90 °C, showing an average reduction of 6.2% and 4% for Vp and Vs, respectively.

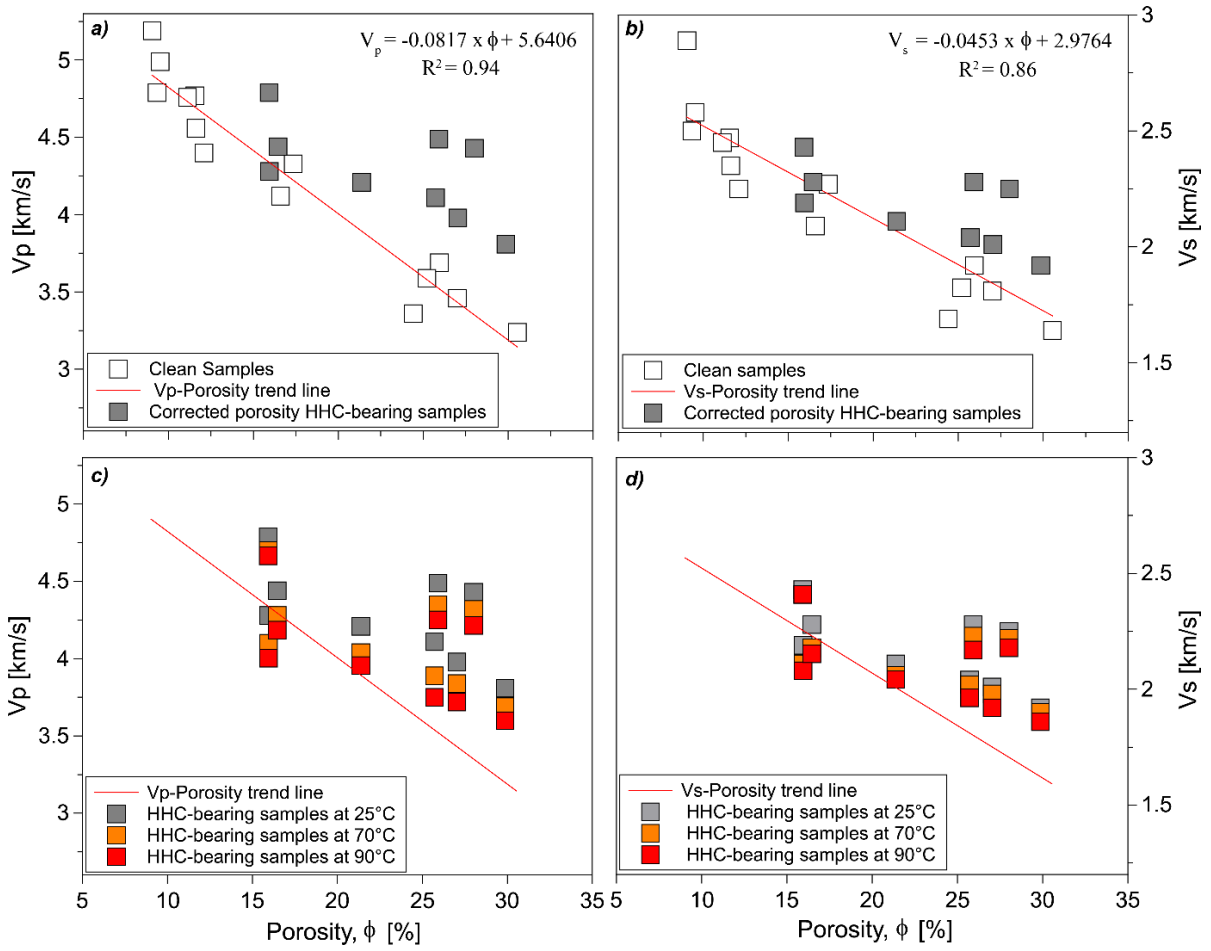

***Figure 1.10**: Variation of (a) P-wave velocity and (b) S-wave velocity for clean samples (white squares) and HHC-bearing samples (gray squares) are plotted as a function of total porosity at ambient temperature. Also, I showed the variation of (c) Vp and (d) Vs with porosity at different temperature: 25 °C, 70 °C and 90 °C. The red line represents the linear relationship obtained between velocity and porosity for clean samples. The uncertainty of the recorded velocities is within the size of the markers.*

Additionally, Vp/Vs ratio has been calculated for both clean and HHC-bearing samples and plotted in Figure 1.11 as a function of total porosity from ambient temperature to 90 °C. The general trend of clean samples at ambient temperature (Figure 1.11a) shows a slightly increment of Vp/Vs with increasing porosity. On the other hand, at ambient temperature Vp/Vs of HHC-bearing samples are plotted with their corrected porosity and it is in an average value of around 1.98 (Figure 1.11a). With increasing temperature from 25 °C to 90 °C (Figure 1.11b), the average Vp/Vs of the HHC-bearing samples decreases of about 2.1%, reflecting the sensitivity of Vp/Vs in temperature changing. The analysis of Vp/Vs variation is noteworthy because this ratio represents a very good lithology indicator (Domenico, 1984) and it has a key role for the identification of hydrocarbon anomalies in seismic sections (McCormack et al., 1984). The high

HHC-bearing samples display a significant reduction of about 3% for Vp/Vs, whereas for low HHC-bearing samples I have calculated a reduction of about 1.6%. Therefore, the Vp/Vs, calculated from the compressional and shear velocities within the temperature range of 25 °C-90 °C, can produce a clear seismic signal, that may be very useful tool to detect the hydrocarbon-rich zone throughout AVO analyses of seismic sections.

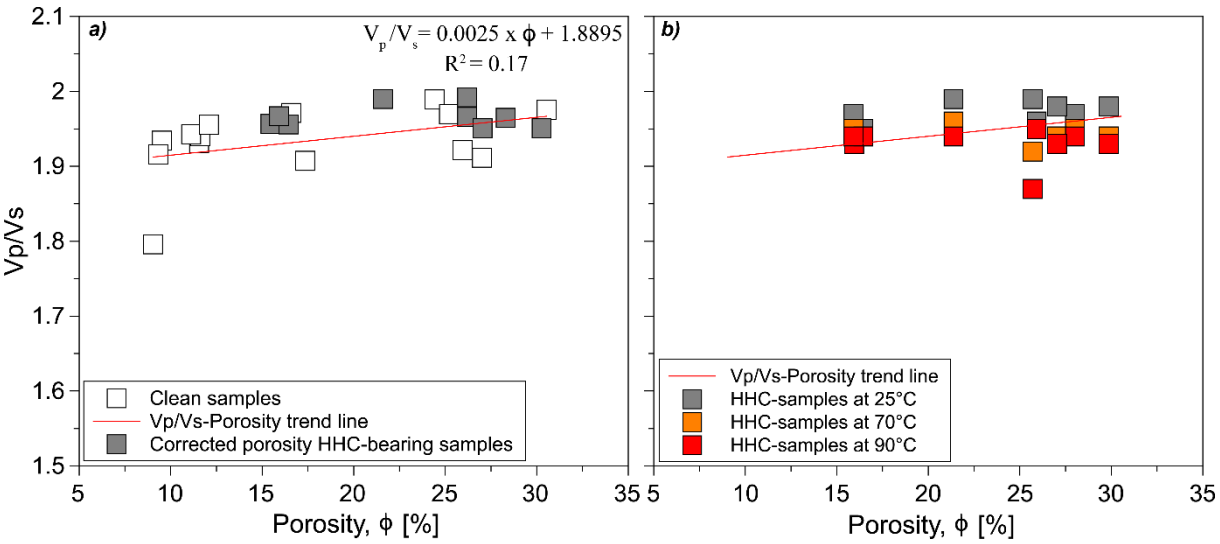

***Figure 1.11**: Calculated Vp/Vs ratio is plotted against total porosity for (a) clean samples (white squares) and HHC-bearing samples (gray squares). Moreover, I reported (b) the calculated Vp/Vs ratio as a function of different temperatures (25 °C, 70 °C and 90 °C) for the investigated HHC-bearing samples. The red line represents the linear relationship obtained between the calculated Vp/Vs ratio and porosity for clean samples.*

1.4.4 The effect of bitumen content on velocity measurements at increasing temperature

The investigated HHC-bearing samples (Table 1.3) can be divided in two groups based on the HHC content: four samples (ACF) with a low HHC content (around 2.20 %) and five samples (CR) with high HHC content (around 15%).

In Figure 1.12, I reported the variation of Vp and Vs as a function of temperature for all investigated samples, discriminating high HHC-bearing samples (in dark gray) and low HHC-bearing samples (in light gray). Basically, all samples show an inverse relationship between wave velocities and temperature: wave velocities decrease with increasing temperature in agreement with analogue measurements on bitumen carbonates (Rabbani et al., 2017; Yuan et al., 2017, 2018). Moreover, Vp and Vs variations outline different trends with increasing temperature, depending on the amount of the HHC content. Low HHC-bearing samples indicate a linear reduction of velocity with increasing temperature. In contrast, high HHC-bearing samples depict a double velocity-temperature trend: when the temperature is less of about 50 °-60 °C a very slight variation of velocities is observed; whereas, if the temperature is higher than 50 °C, the velocities decrease with a higher gradient.

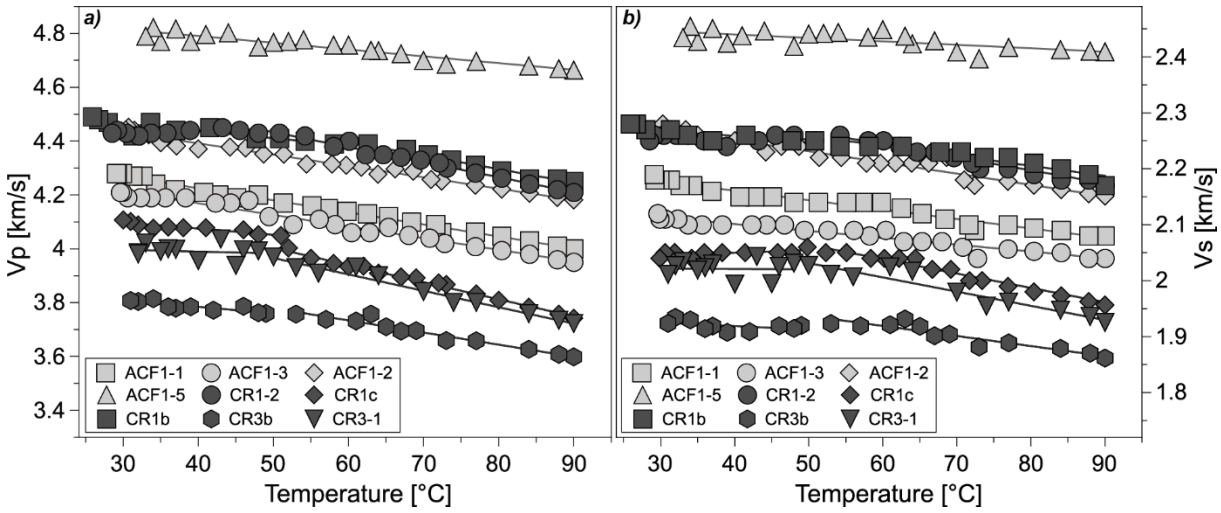

***Figure 1.12**: Evolution of (a) P- and (b) S- wave velocities measured within the entire range of temperature for all investigated carbonate samples: low HHC-bearing samples (in light gray) and high HHC-bearing samples (in dark gray). The lines represent the best fit of the P- and S-wave velocities with the temperature.*

To clearly characterize how temperature and HHC content can influence the velocity of carbonate rocks, I calculated the percentage of Vp and Vs change over the entire temperature range (from 90 °C to 25 °C). Therefore, for a better representation, I decided to use the average values of Vp, Vs and temperature, obtained by averaging every two temperatures and velocities for all samples. The velocity change (ΔV_{change}) was calculated by using the following equation:

$$\Delta V_{change} = \frac{V_{Tf} - V_{Ti}}{V_{Tf}} 100 \quad (1.9)$$

where V_{Ti} are the measured velocities at increasing temperature and V_{Tf} represents the measured velocity at the lowest temperature (around 30 °C). By using equation 1.5, the velocity change spans between 0, when V_{Tf}= V_{Ti}, and >0, when $V_{Ti} < V_{Tf}$. The results of Vp and Vs changes are plotted in Figure 1.9 as a function of the calculated average temperatures. Figure 1.13 shows that for low HHC-bearing samples, Vp and Vs decrease linearly with temperature showing average changes for all four samples of 5.2% and around 3.8%, respectively. On the other hand, high HHC-bearing samples (Figures. 1.13c and 1.13d) outline different velocity changes over the entire temperature range. In the temperature range 50°-90 °C, a larger gradient of velocity variations is observed and, in this interval, the average Vp change of all high HHC-bearing samples is of 6.09% and Vs is of almost 4%. Whereas when the temperature is < 50° C, the average velocity changes for all samples are smaller, being 1% and 0.35% for Vp and Vs, respectively. Going into the details, it results that below 50°C the Vp change is 1.55% (1.28 % Vs) for low HHC-bearing samples and 1.00 % (0.38% Vs) for high HHC-bearing samples. This gentler decreasing slope for high HHC-bearing samples, can be explained by the following phenomena: in each pore a smaller amount of hydrocarbon melts earlier respect to a larger amount because heat capacity of the same material is proportional to its mass (e.g., Halliday et al., 2013). Being the hydrocarbon homogeneously distributed and the type of porosity the same for all samples, hydrocarbon in low HHC-bearing samples may quickly melt due to the lower mass in each pore and thus, a reduction in velocity can be observed earlier respect to higher HHC-bearing bitumen samples. This is confirmed by the observation that at higher temperature the total change of velocities is larger for the high HHC-bearing samples.

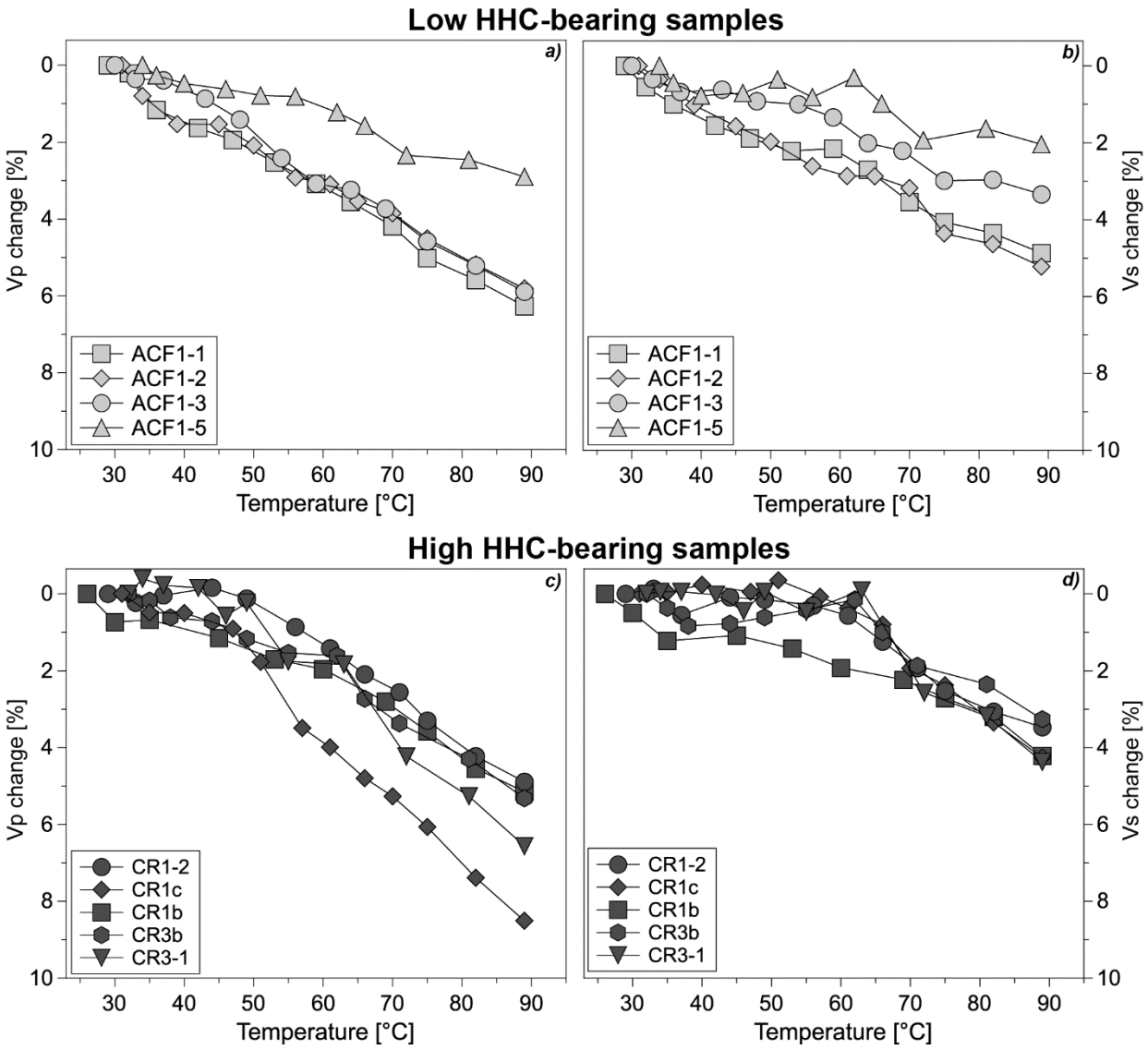

***Figure 1.13**: Velocity changes of P-wave (a and c) and S-wave (b and d) are plotted as a function of average temperature. I reported data maintaining difference between low (~2.2% in light gray) and high (~15% in dark gray) HHC-bearing samples.*

1.4.5 Velocity measurements at elevated pressure

P-wave velocity measurements were conducted during pressurization up to 100 MPa and depressurization back to ambient pressure for both clean and HHC-bearing samples in dry condition (Figure. 1.14). At 100 MPa of confining pressure the recorded Vp values for clean samples (Figure. 1.14a) range from 3.6 km/s to 5.2 km/s whilst for HHC-bearing samples velocity range at 100 MPa is narrower (4.5-4.8 km/s, Figure. 1.14b). The relative increase of velocity by increasing confining pressure for each sample is generally very low and this is particularly evident for HHC-bearing samples (Figure. 1.14b). Moreover, the difference of Vp values obtained during depressurization and pressurization cycles (hysteresis), seems to be slightly larger for clean samples.

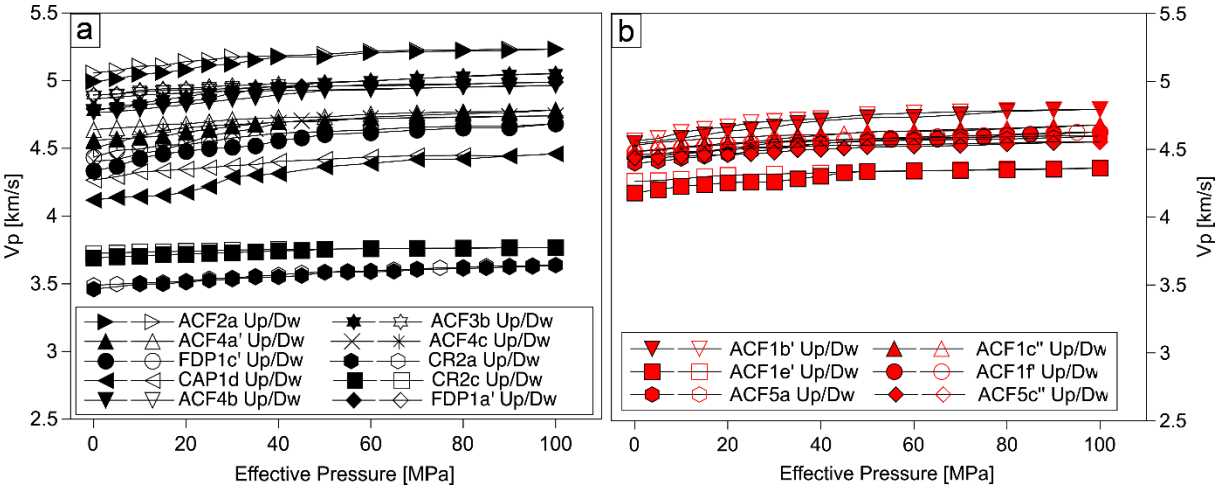

Figure 1.14*: Evolution of axial P wave velocity at increasing effective pressure for representative samples of clean (A) and HHC-bearing (B) limestone. For all samples, the P wave velocity were measured during both pressurization (solid symbol, Up) and depressurization (open symbol, Dw) cycles.*

To quantify these observations, velocity hysteresis (H) at ambient pressure, has been calculated by using the equation:

$$H = \frac{V_{p\,(down)} - V_{p\,(up)}}{V_{p(up)}} \qquad (1.10)$$

where $V_{p(up)}$ and $V_{p\,(down)}$ are the Vp measured at ambient pressure, at the beginning and at the end of the test under pressure, respectively.

Results (Figure 1.15) show that hysteresis is scarcely related to porosity, however, HHC-bearing samples generally show a decreased hysteresis respect to the trend derived from clean samples (red line in Figure 1.15). Therefore, the presence of the hydrocarbons limits the effect

of the confining pressure increasing the elasticity of heavy oil-bearing samples with respect to clean samples.

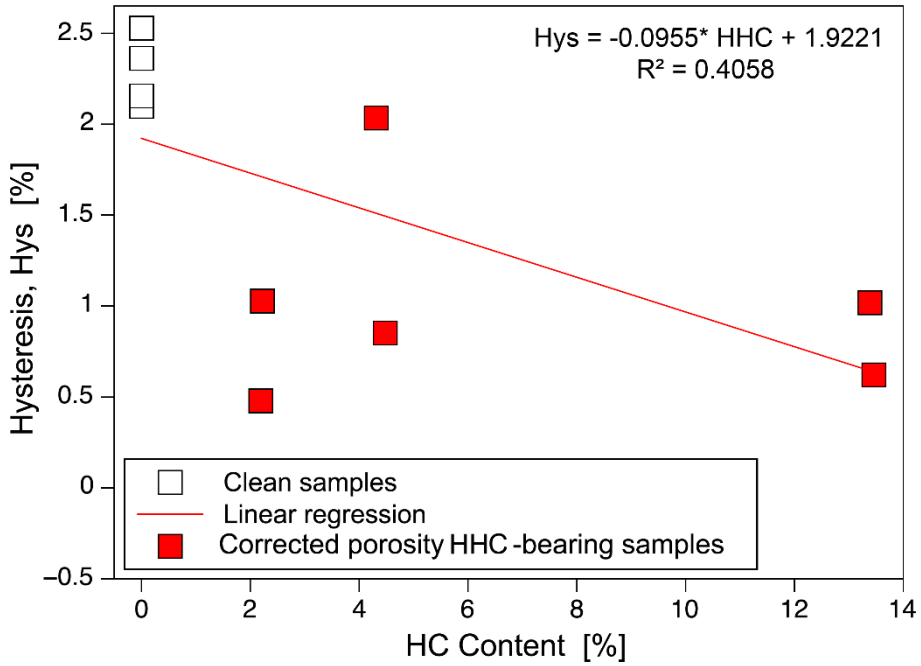

***Figure 1.15**: Variation of Hysteresis, measured at pressure ambient after pressurization cycle that reached 100 MPa (Figure 1.14), as a function of total corrected porosity for clean (white squares) and HHC bearing samples (red squares).*

Vp/Vs ratios, calculated from the measured velocities, are plotted in Figure 1.16 as a function of confining pressure. The Vp/Vs ratio remains essentially constant with increasing confining pressure (Figure 1.16) for both clean and HHC-bearing samples indicating that Vp and Vs follow a very similar pattern with increasing pressure. The range of Vp/Vs ratios for both clean (Figure 1.16a) and HHC-bearing (Figure 1.16b) is similar being between 1.9 and 2. This highlights that the bitumen does not act as a fluid since the presence of fluids should increase the Vp/Vs ratio as observed for several lithologies in laboratory (Heap et al., 2014; Smeraglia et al., 2014; Trippetta et al., 2010) and at crustal scale (Chiarabba et al., 2009; Peacock et al., 2011).

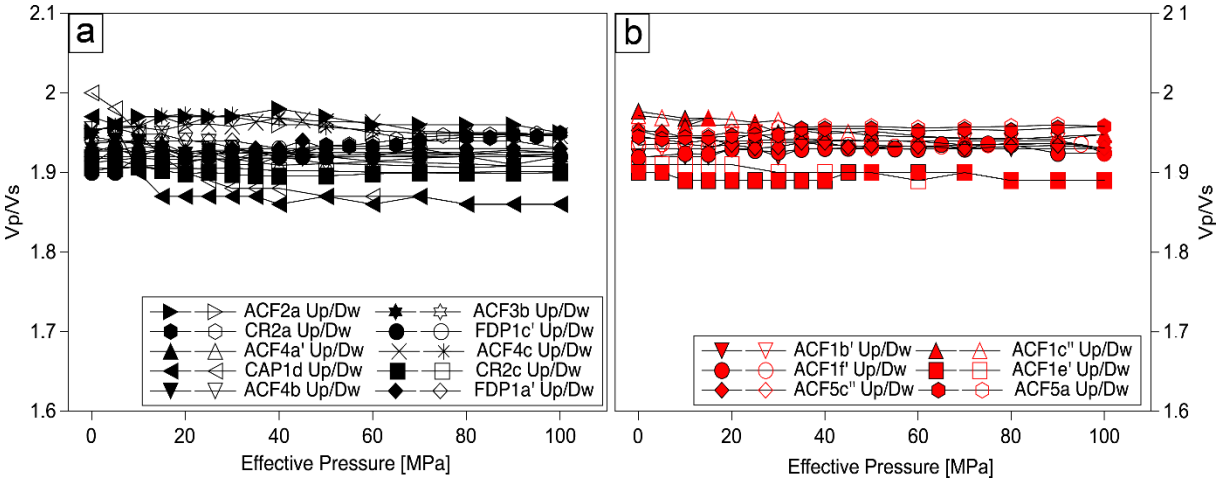

***Figure 1.16**: Calculated Vp/Vs ratio as a function of confining pressure for (a) clean and (b) HHC-bearing samples.*

1.4.6 Dynamic Elastic moduli

The dynamic elastic moduli (E_d and ν_d) were calculated from measurements of Vp and Vs using the equations:

$$E_d = \rho \frac{V_s^2(3V_p^2 - 4V_s^2)}{V_p^2 - V_s^2} \quad (1.11)$$

$$\nu_d = \frac{1}{2}\frac{V_p^2 - 2V_s^2}{V_p^2 - V_s^2} \quad (1.12)$$

where ρ is the bulk rock density and Vp and Vs are the compressional and shear elastic wave velocities, respectively. Results are summarized in Table 1.4.

Confining pressure has not a significant effect on Vp and Vs (Figure 1.14), whilst total porosity exerts a strong control on the tested samples. Thus, I here report dynamic elastic moduli calculated from measurements taken at ambient pressure in relation with the measured porosity. For clean samples E_d values are in the range 16.5 to 43.7 GPa. The higher values correspond to the clean samples with lower porosity (~10%), while the lower values correspond to the samples with high effective porosity (~30%). As observed for Vp data, an increase in porosity corresponds to a decrease in E_d in agreement with literature data (Heap et al., 2019). For HHC-bearing samples, porosity and E_d do not follow the trend of the clean samples (red line in Figure 1.17). Moreover, for the same original porosity, the presence of HHC generally increases E_d (Figure 1.17 red squares). This observed increase in Ed makes samples more difficult to deform suggesting that the hydrocarbons presence stiffens the rocks.

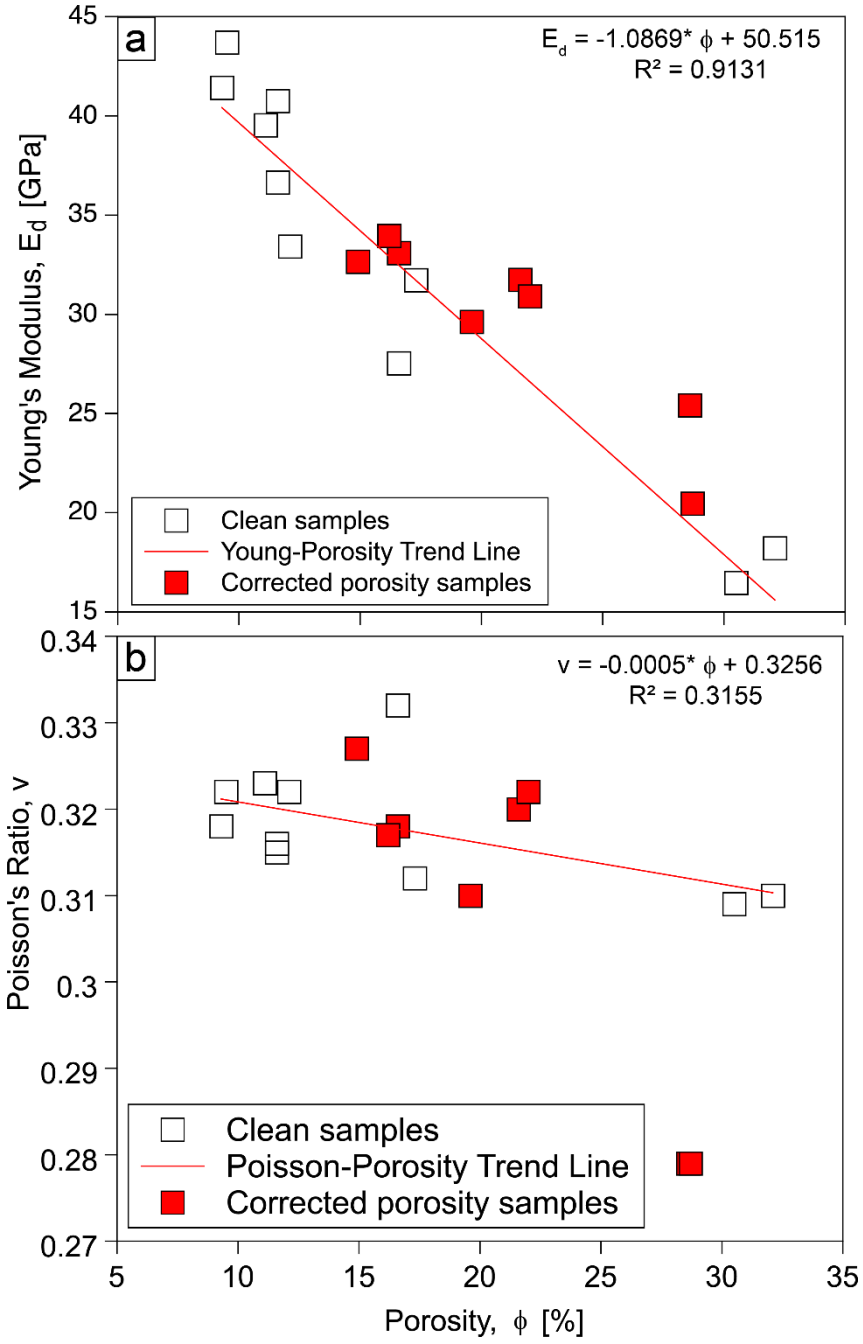

***Figure 1.17**: (a) Variation of Young's modulus (E_d) and of Poisson's ratio (ν), measured from ambient pressure, as a function of effective porosity for clean (white squares) and HHC-bearing (red squares) limestone samples. The inverse linear relations of Ed and ν with porosity have been calculated for clean samples.*

Poisson's ratio is in the range 0.31-0.33 for clean samples (Figure 1.18 and Tab. 1.4), whilst for HHC-bearing samples is wider spanning from 0.28 to 0.33. Porosity shows very weak relation with Poisson's ratio (Figure 1.18), in particular with respect to what observed for the

Young's modulus. However, HHC-bearing samples show Poisson's ratios values (red squares in Figure 1.18) generally lower respect to the trend derived from clean samples (red line in Figure 1.18), in particular the high porosity HHC-bearing samples show the lowest Poisson's ratio of the whole dataset.

1.4.7 Compressive strength and elastic moduli

For this kind of tests, I selected 6 samples (3 clean and 3 HHC-bearing samples) characterized by similar original porosity (~28%) in order to correctly assess only the influence of HHCs. The full set of cyclic loading-unloading uniaxial experiments is shown in Figure 1.18. Cyclic loading-unloading experiments, characterized by a progressive increase in maximum stress, show the progressive shift in strain of the starting loading point respect to the previous loading cycle (permanent strain in Figure 1.18). This shift is indicative of an increasing amount of permanent, irrecoverable strain with increasing loading cycles. In particular, it results that the permanent strain is constantly larger for clean sample (black lines Figure 1.18) with respect to HHC-bearing samples (red squares in Figure 1.18), indicating a stiffer behaviour for HHC-bearing samples.

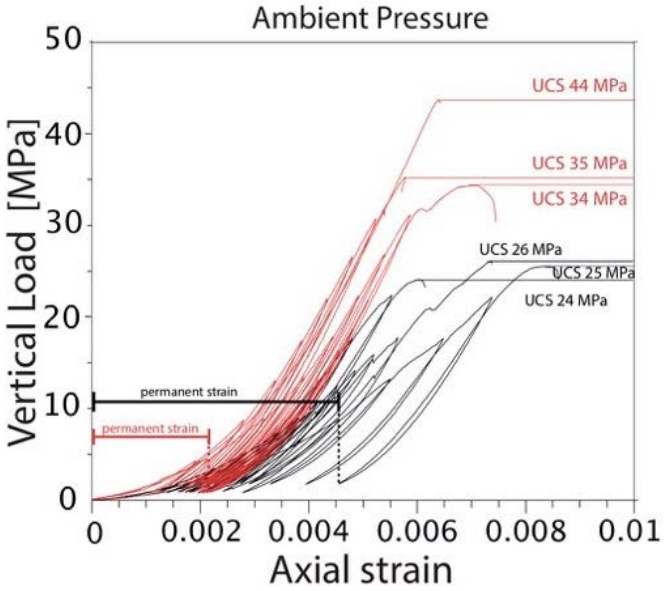

***Figure 1.18**: Full suite of axial stress-curves from cyclic axial stressing experiments on both clean (black lines) and HHC bearing samples (red lines). The clean samples failed at Compressive Strength (CS) of 24, 25 and 26 MPa whilst HHC-bearing samples failed at 34, 35 and 44 MPa.*

All tested clean samples show a compressive strength of about 25 MPa that represent low values for carbonate rocks (Cilona et al., 2012; Rajabzadeh et al., 2012) and they are related to the high porosity of the investigated samples (Baud et al., 2017) and to their bioclastic nature (Croizé et al., 2010). HHC-bearing samples are, on the other hand, all characterized by a higher compressive strength that increase up to 44 MPa with an average value of 38 MPa.

The evolution of elastic moduli with increasing stress is different depending on the type of analyzed lithology (Grindrod et al., 2010; Heap et al., 2010; Heap and Faulkner, 2008; Trippetta et al., 2013). As observed from Trippetta et al. (2013) for carbonate rocks, during the cyclic loading I systematically observed significant changes in the static elastic moduli that are interpreted as involving a three-stages process. This evolution is attributed to the dominance of compaction in Stage I, dilatant crack growth and coalescence in Stage III, and a balance between these two competing processes in Stage II. I thus calculated the static Young's modulus (Es) by dividing the applied stress over the axial strain for each cycle for the range where gradients of unloading and subsequent re-loading curves were less than 10% different. I observed the same three-stage behaviour observed by Trippetta et al. (2013) so I averaged the values derived from Stage II that represent the "elastic part" of the test. The so calculated Young's moduli are 5.7 GPa and 9.9 GPa for clean and HHC-bearing samples, respectively. Thus, in agreement with previous observations, HHC presence appears to strengthen the rocks, increasing both the strength and the stiffness (Es) of the samples.

1.5 Field Work

To compare these laboratory results with larger scale data, I analyzed 11 structural scanlines (Table 1.5) in the northern flank of the Majella Mountain (rectangles in Figure 1.3b). To avoid any possible difference in the mechanical behaviour of rocks between laboratory and field samples I only selected outcrops belonging not only to the same formation (Bolognano Fm) but also to the same lithofacies (Lepidocyclina calcarenite 2) following the most recent literature (Brandano et al., 2016). Moreover, I choose locations not affected by faulting to obtain a homogeneous dataset not influenced by the presence of damaged zones in the nearby. I then focused on both clean (Figure 1.19a) and HHC-bearing (Figure 1.19b, c) outcrops where I measured the type of fracture (joints, veins, tectonic stylolites, small faults), aperture, dip direction, inclination and spacing. Where possible, scanlines have been analyzed in orthogonal directions (Figure 1.3b) to increase the representability of this dataset avoiding the "Terzaghi" bias (Mauldon and Mauldon, 1997; Terzaghi, 1965). The analyses show that fractures for both HHC-bearing and clean outcrops are mainly joints-type with aperture not more than 2 mm with few stylolites and very few small faults. Reopened fractures within HHC-bearing outcrops are often filled by hydrocarbons. Results on orientation show two main fractures trends: NW-SE and NNE-SSW for clean outcrops (Figure 1.19a inset) and the same two families have been observed for HHC-bearing samples (Figure 1.19b inset). Figure 1.19d highlights that the fracture orientation is comparable for clean and HHC-bearing outcrops, whilst the main difference between the two types of outcrops is the absolute number of measured fractures. For HHC-bearing outcrops the number of measured fractures (55, Figure 1.19a, b inset) is ~0.25 times the fractures observed on clean outcrops (207, Figure 1.19a inset), being the total analyzed length of the two types of outcrop very similar (20 and 22 m for clean and HHC-bearing outcrops respectively, see Table 1.5). This is directly related to fracture frequency showing that HHC-bearing outcrops are four times less fractured respect to clean outcrops (Table 1.5).

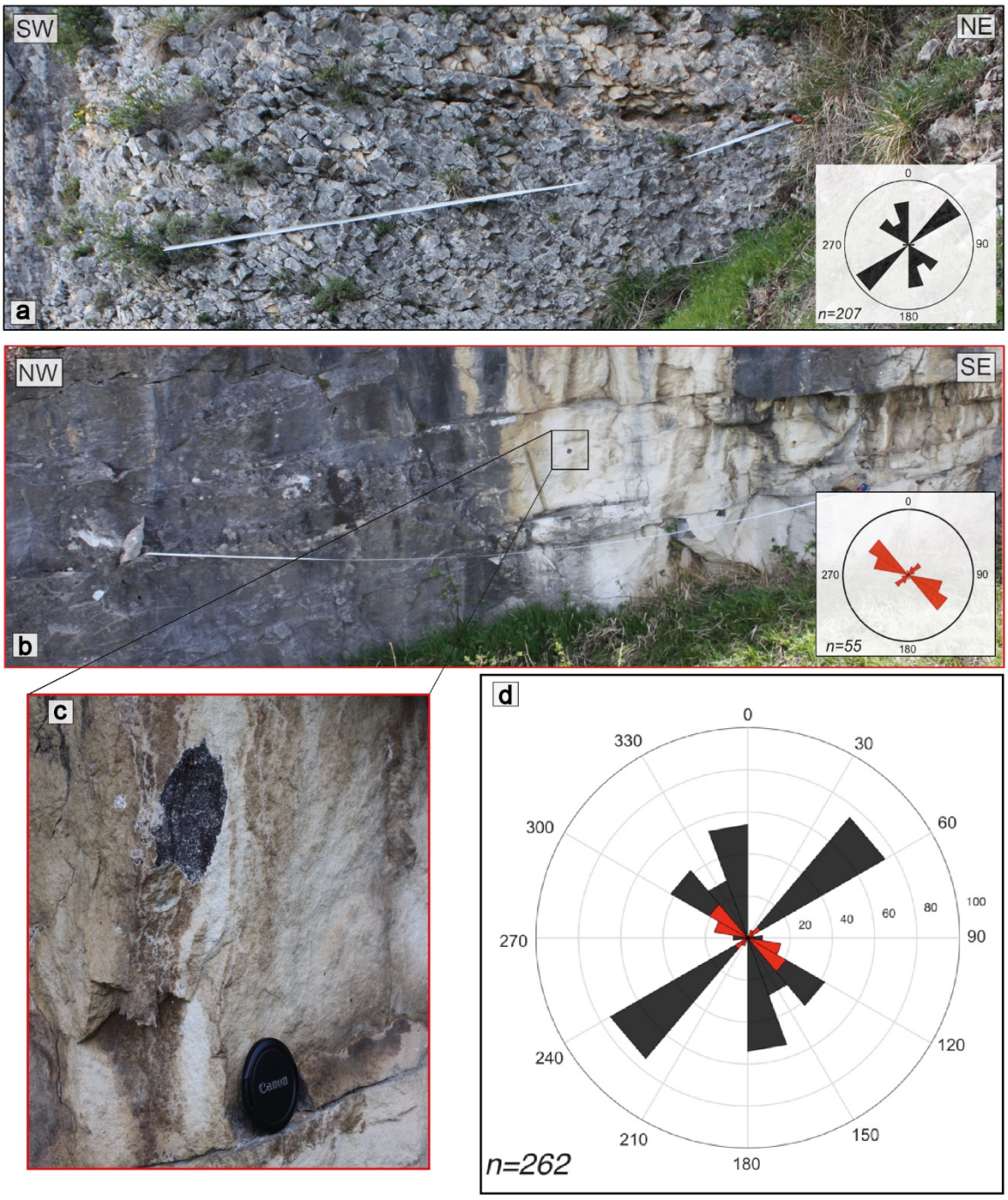

***Figure 1.19**: (a) Outcrop picture of clean fractured Lepidocyclina showing two main fracture orientations striking mainly NW-SW and NW-SW. The bottom-right inset shows the total number of measured fractures (207) for all the 6 outcrops of clean Lepidocyclina, (b) Outcrop picture of HHC-bearing Lepidocyclina showing two main fracture orientations striking mainly NNE-SSW and NW-SE. The bottom-right inset shows the total number of measured fractures (55) for all the 5 outcrops of HHC-bearing Lepidocyclina. (c) Detail of the HHC-bearing portion showing the high grade of saturation of the outcrop. (d) Rose diagram comparing number and orientation of fractures for clean (black) and HHC-bearing (red) outcrops. The orientations agree whilst the number is much lower for HHC-bearing outcrops.*

Scanline	Length [m]	N° of fractures	N° of fractures/m	Bedding dipdir/incl	Type
1	0.90	29	32.3	330/16	Clean
2	3.60	36	10.0	310/17	Clean
3	4.00	33	8.3	350/13	Clean
4	2.70	54	20.0	299/06	Clean
10	4.40	28	6.4	315/15	Clean
11	4.40	27	6.1	327/16	Clean
Total	**20**	**207**	**10.4**	**322/14**	**Clean**
5	5.00	7	1.4	335/06	HHC-bearing
6	4.75	18	3.8	326/06	HHC-bearing
7	5.00	14	2.8	297/06	HHC-bearing
8	5.00	10	2.0	289/12	HHC-bearing
9	2.43	6	2.5	302/14	HHC-bearing
Total	**22**	**55**	**2.5**	**310/09**	**HHC-bearing**

***Table 1.5**: Summary of the data acquired on both clean and HHC-bearing outcrops in terms of number of measured fractures. Bedding attitude in terms of dip directions and inclinations are also reported. Note that both clean and HHC-bearing outcrops pertain to the same lithofacies (Lepidocyclina calcarenite 2).*

1.6 Discussion

1.6.1 Implications of the acoustic response of HHC-bearing samples

In this study I recorded the acoustic velocities to analyze the response of HHC-bearing carbonate samples to temperature change at different HHC content since properties of high-viscosity fluid, like bitumen, are strongly influenced by the temperature. Monitoring these variations is fundamental in reservoir characterization as well as in production monitoring (e.g., Tatham and Stoffa, 1976; Lines at al., 2005b) since acoustic properties drive the seismic response of reservoir rock volumes.

Thus, to better evaluate the temperature effect on samples with different HHC contents, I conducted acoustic velocity measurements on carbonate-bearing samples, which belong to the Bolognano Fm of the Majella mountain. Laboratory data, presented in this study, outline that the presence of heavy hydrocarbon influences the petrophysical properties of hosted carbonate rocks. Velocity data highlight a general reduction in the acoustic properties of carbonate samples with increasing temperature, from ambient temperature to 90 °C. This downward tendency is sensible for HHC-bearing samples, indicating a strong influence of temperature on changing the properties of viscous fluid, as evidenced in similar conditions by Yuan et al. (2017, 2018) and Rabbani et al. (2016) for bitumen carbonate samples and Baztle et al. (2006) for heavy oil samples. These authors postulated that the decreasing of P- and S-wave velocities with increasing temperature is likely due to a strongly temperature dependent of the bitumen properties, such as viscosity, bulk, and shear modulus. In addition, velocity results show that another important factor influencing the acoustic response of hydrocarbon-bearing samples is the amount of hydrocarbons. In fact, I noticed a distinct trend between low and high HHC-bearing samples: both Vp and Vs of low HHC-bearing samples depict a linear reduction throughout the investigated temperature range; whereas high HHC-bearing samples show a double trend with a higher slope in velocity reduction when the temperature is above 50°- 60 °C. Therefore, bearing in mind that HHC properties are deeply temperature-dependent, this different trend for the samples with higher HHC content is indicative of a change in the physical state of hydrocarbon from a solid state when the temperature is below 50 °C to liquid state if the temperature is increased above 50°-60 °C.

Data from wells around in the study area (ViDEPI PROJECT, 2012) show an average thermal gradient of around 43 °C/km. Thus, a temperature interval of 50°-60 °C in the investigated area corresponds to about 1-1.7 km depth. The effect of pressure has been proved to be negligible in the range of 0-4 km for the same Bolognano Fm (Figure 1.14), so ambient pressure of these velocity measurements can be considered as reliable for the investigated formation. Furthermore, the transition point of the temperature (in the interval of 50°-60 °C) is consistent with previous works on pure heavy oil samples (Han et al., 2006) and bitumen saturated carbonate samples (Yuan et al., 2017, 2018; Rabbani and Schmitt, 2019) under similar experimental conditions. It is worth noting that in real scenario, in-situ rocks are usually saturated, containing both bitumen and brine. However, at such relatively low pressure and temperature the influence of brine on acoustic velocity should not influence the seismic P-wave velocity at crustal scale as well shown in literature (Nur et al., 1984; Chopra et al., 2010; Mavko et al., 2009). On the other hand, temperature is a primary factor influencing acoustic velocity when rocks are saturated with oil due to strongly temperature dependence of their physical properties (Nur et al., 1984). Moreover, these data suggest a more pronounced reduction of the P- than S-wave velocities with increasing temperature and it well noticed evaluating the variation of acoustic response in terms of velocity changes (Figure. 1.13). To explain such behaviour, I start form the observation that at room temperature HHC, hosted in the investigated carbonate samples, is in a solid state and it has a negligible shear modulus of 11.6 GPa for low HHC-bearing samples and 9.6 GPa for high HHC-bearing samples. Conversely, at higher temperature HHC progressively melts down and so its shear modulus drops drastically, as evidenced by Batzle et al. (2006) for heavy oil samples with an API = -5°.
The equation of P- and S-wave velocities are given by:

$$V_p = \sqrt{\frac{K + \frac{4}{3}\mu}{\rho}} \tag{1.13}$$

and,

$$V_s = \sqrt{\frac{\mu}{\rho}} \tag{1.14}$$

where K is the bulk modulus, μ is the shear modulus and ρ is the density. It is well known that the bulk density of HHC-bearing carbonate sample is correlated to temperature and the density decreases with increasing temperature, as observed by some experiments on HHC samples

(e.g., Eastwood et al., 1993; Mochinaga et al., 2006). In equations 1.13 and 1.14, the density results to be inversely proportional to the velocity and so a reduction of the density should lead to a rise of velocity, but from laboratory results I observed a reduction in velocity in agreement with literature data of heavy oil saturated samples (e.g., Rabbani et al., 2016, 2019; Yuan et al., 2017, 2018). This reduction of both P- and S-wave velocities is attributed to a larger change in the bulk and shear moduli through the investigated temperature range respect to the drop of density. Thus, the variation of Vs is only affected by the shear modulus that drops drastically with increasing temperature since HHC behaves like a fluid. On the other hand, the variation of Vp is not only influenced by shear modulus, but also by the bulk modulus. Therefore, I highlight that the bulk and shear moduli of bitumen play a greater role in the velocity variations under different temperature. Specifically, I suggest that the more marked decrease of Vp respect to Vs is related to the fact that Vp is affected by a double decrease of both K and μ (equation 1.13), while Vs variation is only related to a decrease of the shear modulus, μ, (equation 1.14), that approaches to zero at high temperatures when bitumen behaves as a light oil.

1.6.2 Theoretical model to predict Vp as a function of temperature and hydrocarbon saturation

In this section, I use the collected dataset as a base to propose a theoretical model for estimating the P-wave velocity as a function of different variables, such as temperature, hydrocarbon content and porosity. This model has been developed to give to the geophysics community a powerful tool that directly links the variation in seismic properties to the presence of heavy hydrocarbons. This P-wave velocity model was developed considering three different initial porosities: 16%, 26%, 30%, so that I can present an estimation of P-wave velocities within the entire porosity range of the investigated samples. The initial porosities were calculated by summing the measured pycnometer total porosity with HHC content (in volume) and consequently, they refer to a total porosity of the HHC-free samples (see section “Sample characterization” and Table 1.2). I evaluated the P-wave velocity at different simulated HHC contents: 0%, 2.1%, 5%, 8%, 12%, 15%, allowing us to represent the entire range of the HHC contents calculated for the investigated samples.

For samples ACF1-1, ACF1-2, CR1c the influence of hydrocarbon on Vp is out of the trend respect to the entire dataset, leading to an underestimation of the predicted P-wave velocities respect to the actual content of hydrocarbon (Figure 1.20a). I decided to remove these three data points from my modelling dataset.

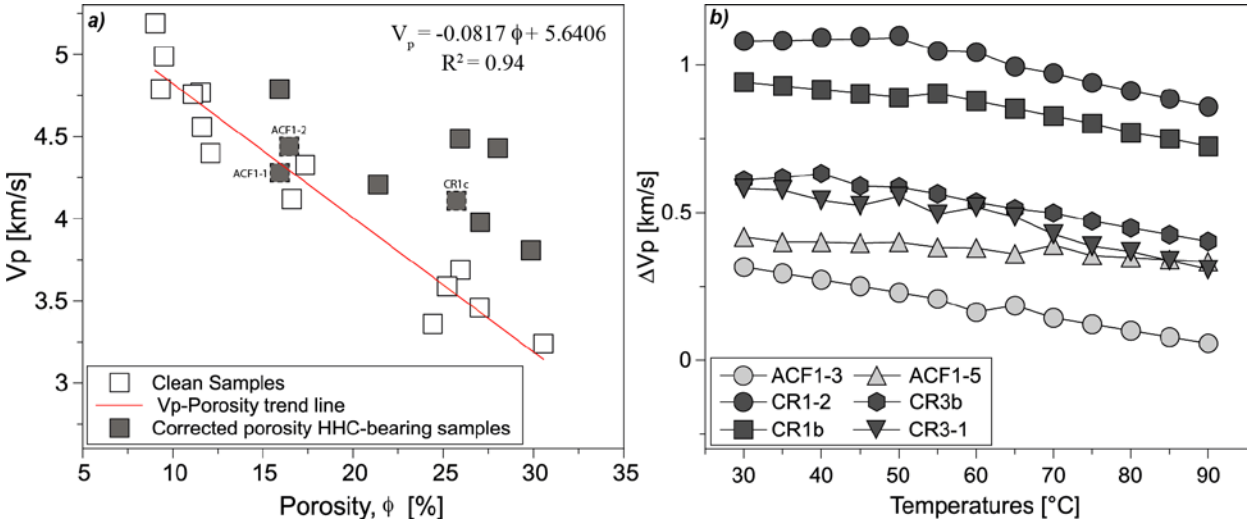

***Figure 1.20**: Laboratory calculated trends used to develop the theoretical model. a) Velocity-porosity relationship used in the model and three samples were removed from my modelling dataset (symbols with dashed lines). b) Trends of P-wave velocity variation (ΔVp) at increasing temperature, used to estimate the variation of P-wave velocity in the theoretical model.*

A four-step workflow has been applied to develop a method for the estimation of P-wave velocities:

(1) For each sample, I considered the P-wave velocities recorded at different temperatures (Figure 1.12a). Starting from these data, I considered in the model 13 temperature values at steps of 5 °C (range of 30°-90 °C), thus representing the entire investigated temperature range. Thereby, each point of the model is related to the same temperature, so that a proper velocity data comparison could be made. Furthermore, for all samples I considered the corresponding recorded P-wave velocity at each temperature. When the velocity data were lacking for a specific temperature, I calculated the velocity (V_{pm}) using the velocity-temperature relationship, obtained for the corresponding sample (Figure 1.12a).

(2) For all HHC-bearing samples I calculated the theoretical P-wave velocity (V_{pt}), in absence of HHC. To do this, I applied the correction of the porosity for HHC-bearing

sample (see section “Sample characterization” and Table 1.3) and then I referred to the Vp-Porosity relationship of clean samples of equation 1.7 and Figure 1.10a. Consequently, knowing that V_{pm} is a P-wave velocity actually recorded in laboratory for the real samples, I determined the HHC influence on acoustic velocity response (ΔVp) using the following equation:

$$\Delta V_p = V_{pm} - V_{pt} \quad (1.15)$$

By using equation 1.15, I have been thus able to determine the relationship between ΔVp and the entire temperature range (30°-90 °C) for each investigated sample as reported in Figure 1.20b.

(3) Since each sample was characterized by a known HHC content (see section "Bitumen characterization” and Table 1.3), I then determined the relationship between ΔVp (calculated at step 2) and HHC content for all investigated samples at each temperature value.

(4) As a last step, I calculated the P-wave velocity using the Vp-Porosity relationship (equation 1.7) simulating 0% of HHC content for the three initial porosities of 16%, 26%, 30%. Subsequently, I used the ΔVp- HHC trends, computed at each temperature (step 3) to calculate the HHC effect on velocity (ΔVp), by assuming an increasing HHC content (2.1%, 5%, 10%, 12%, 15%). The obtained ΔVp was added to the P-wave velocity calculated for a single sample with 0% HHC content.

The obtained models at different HHC content are reported in Figure 1.21 for three defined initial porosities (Figures 1.21a-1.21c). The predicted Vp decreases with increasing porosity for both simulated HHC content and HHC-free conditions, in agreement with the defined velocity-porosity relationship. Therefore, Vp at HHC-free conditions ranges from 4.43 to 3.19 km/s (16-30% porosity) and the sample with high porosity corresponds to a lower velocity. Vp is constant since the porosity of carbonates results to be temperature independent within the investigated range in agreement with literature data (e.g., Mehrgini et al., 2016; Trippetta and Geremia, 2019).

Regarding hydrocarbon influence on acoustic velocities, for all the investigated temperature and porosity ranges, the models display an increment of the predicted Vp proportionally to the simulated HHC content. This is related to the fact that bitumen physical properties, such as bulk modulus and viscosity, are temperature dependent and, consequently, influence the acoustic

response of hosted carbonate frame (Batzle et al., 2006; Rabbani et al., 2016; Rabbani and Schmitt, 2018; Yuan et al., 2018). The P-wave velocities predicted from the theoretical model at ambient pressure and under different temperatures from 30 °C to 90 °C, can be correlated positively to those measured by Yuan et al. (2015b) for two bitumen carbonate samples. These samples show porosity values from 7.38% and 10.23%, which are inversely related to the bitumen content: low porosity corresponds to high bitumen content and vice versa. Although, these bitumen carbonates display lower values of porosity respect to those of the modeled samples, a similar inverse correlation between porosity and velocity is clearly observed. In agreement with my results, the downward tendency of velocities with increasing temperature is displayed for two bitumen carbonate samples and, also a more marked reduction is recorded for samples with higher bitumen content within the entire investigated temperature (20 °C-120 °C).

For what regards the temperature influence, at low HHC content all models show a reduction of the predicted Vp by increasing temperature. In particular, with increasing simulated HHC content, a significant transition from a linear to a more marked double trend behaviour can be observed for the predicted Vp variation with increasing temperature at high HHC contents for all the investigated porosities.

It is well known that seismic properties of a porous rock with different fluid types can be usually predicted by applying Gassmann fluid substitution (Gassmann, 1951). One assumption of the Gassmann model is that the shear modulus is independent on the fluid type. Because the shear modulus of heavy hydrocarbon evolves with increasing temperature from a finite value at low temperature to near zero value at high temperature, the predicted velocities by the Gassmann model match the velocities fairly well at higher temperatures, but at lower temperatures the velocities are drastically underestimated for bitumen-bearing samples, as shown by Kato et al. (2008) for bitumen sands.

To discriminate between absolute and relative HHC content, I calculated the hydrocarbon saturation (S_{HHC}) with the following equation:

$$S_{HHC} = \frac{HHC\ content}{\phi_{initial}}\ 100 \tag{1.15}$$

This parameter represents the fraction of the pore space occupied by hydrocarbon respect to the total volume of sample. Starting from the sample with lower initial porosity (16%- Figure 1.21a), the so calculated hydrocarbon saturation spans from 0% to 94%, for sample with

intermediate initial porosity (26%- Figure 1.21b) S_{HHC} is in the range 0-58% and at higher initial porosity (30%- Figure 1.21c) it varies between 0% to 50%.

Regarding hydrocarbon saturation, the variations of P-wave velocity as a function of temperature show a non-systematic relationship. For example, if I consider the simulated HHC content of 15%, the corresponding hydrocarbon saturations, calculated at 16%, 26% and 30% of porosity, are: 94%, 58% and 50%, respectively. Therefore, in the interval of temperature 50 °C- 90 °C, the velocity changes (calculated with equation 1.9), show variations of 4.3%, 4.9% and 5.3%, respectively. These data highlight that sample with same absolute HHC content, that corresponds to different hydrocarbon saturations, depict a velocity change that increases inversely respect to the hydrocarbon saturation. In particular, the velocity change is 5.3% at 50% of saturation and 4.3% at 94% of saturation. Consequently, the velocity change seems to be more linked to the absolute volume of HHC respect to the sample saturation.

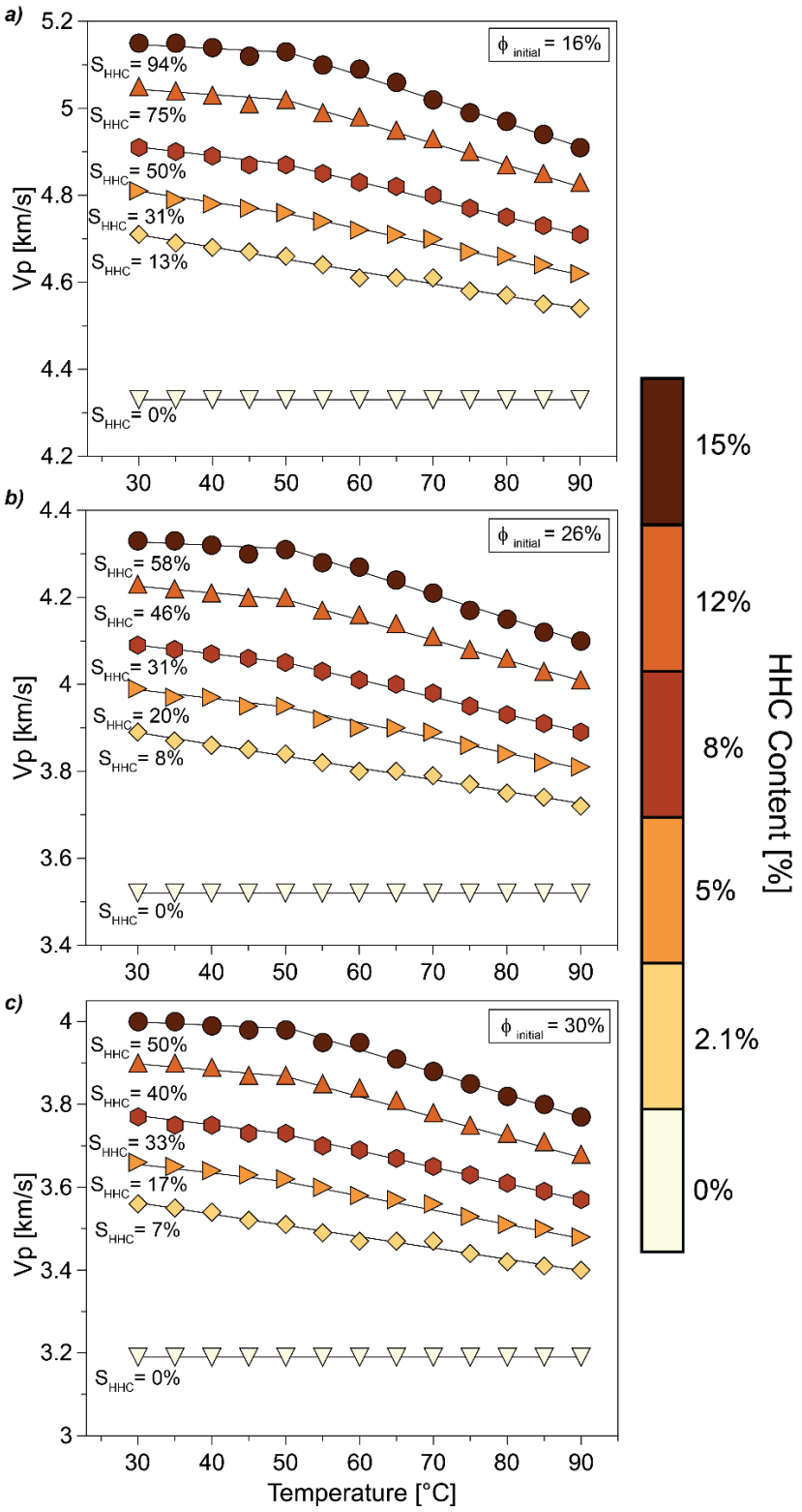

***Figure 1.21**: Evolution of predicted P-wave velocity as a function of temperature at three distinct levels of initial porosity for investigated samples of the Bolognano Formation: (a) Low porosity 16%; (b) Intermediate porosity 26% and (c) High porosity 30%. For each level of porosity, I plotted the estimated Vp simulating different HHC content within the sample (see color bar). I also reported the level of hydrocarbon saturation for each investigated HHC content.*

1.6.3 Integration of laboratory and field data at regional scale

It is well known that the mechanical behaviour of the host rock is function of the depositional facies, diagenetic processes, and fracture distribution, that affect the petrophysical properties of carbonate-bearing reservoirs such as the Bolognano Fm of the Majella mountain. Laboratory and field data presented in this work demonstrate that also the presence of infilling material such as hydrocarbons in form of heavy oils severely affects the petrophysical properties of host rocks, being all the studied rocks collected from the same depositional facies.

In particular, for the same porosity, HHC-bearing samples show higher Vp and Vs, lower hysteresis, lower permanent strain, higher Young's modulus (both static and dynamic), lower Poisson's ratio and higher compressive strength, thus, the presence of bitumen strengthens and stiffens the Bolognano Fm. It is worth noting that low viscosity fluids such as water or light oil weaken the host rock by decreasing its elastic properties (Baud et al., 2009; David et al., 2015; Fabricius et al., 2010; Heap et al., 2011; Risnes et al., 2005; Stanchits et al., 2011), whilst for very high-viscosity fluid such as bitumen I observed an opposite behaviour at room temperature in the laboratory, in agreement with literature data (Trippetta and Geremia, 2019; Yuan et al., 2018, 2016). This opposite behaviour is likely to be related to the fact that the HHC that fills the studied samples, has a rigid and viscous structure and a shear modulus at temperature lower than about 50° C (Han et al., 2008; Yuan et al., 2017) in contrast to a Newtonian fluid (Trippetta and Geremia, 2019).

In the field, all the investigated outcrops, both clean and HHC-bearing, pertain to the same structural domain (NW flank of the Majella Mountain) and thus they are likely to have experienced the same tectonic history. This is confirmed by the observation that fractures characterizing HHC-bearing and clean outcrops have very similar orientations suggesting that they formed under the same stress field. Moreover, the measured orientations are also in agreement with fractures previously measured on the Bolognano Fm and on older formations (Lavenu et al., 2014). HHC-bearing outcrops are much less fractured respect to adjacent clean outcrops indicating a different (stiffer) mechanical response respect to same applied stresses, in agreement with laboratory data. The higher Young's modulus of the HHC-bearing portions leads to a lower fracture density because of the larger stress-reduction shadow in full agreement with theoretical models (Gross et al., 1995; Hobbs, 1967) and field data on limestones (Lézin et al., 2009; McGinnis et al., 2017). Bearing in mind that the whole area has been exposed to the same stress field and that low viscosity fluids should weaken the host rock (David et al., 2015; Risnes et al., 2005), I can infer that, when the last stage of fracturing in the Majella Massif

occurred, some portions of the host rock were already saturated in bitumen that prevented rock fracturing. The high primary porosity of the studied formation is almost totally effective driving to high permeability (Baud et al., 2017; Ehrenberg et al., 2006) that allowed the saturation of the unfractured reservoir. I thus speculate that HHC migration predates the last stage of deformation of the Bolognano Fm, implying that the primary porosity of the reservoir (Bolognano Fm) is the main factor driving the secondary migration of the HHCs.

1.7 Conclusions

The petrophysical characterization conducted on carbonate samples with different HHC contents, belonging to the Bolognano Fm (Majella, in Central Italy), allowed to measure and compare the variations of petrophysical properties between HHC-bearing and HHC-free samples.

Laboratory results highlight that the presence of HHC within the carbonate samples of the Bolognano Fm affects both porosity and seismic velocities. Specifically, a linear inverse relationship between porosity and wave velocities is shown for clean samples at ambient conditions of temperature and pressure. While HHC-bearing samples are out of the Velocity-Porosity trend and the presence of HHC increases P- and S-wave velocities. With increasing temperature (from 25° to 90 °C) the average P- and S-wave velocities decreases of about 6.2% and about 4%, respectively. Moreover, by comparing the variations of P- and S-wave velocities at different temperature, P-wave velocity of the HHC-bearing samples appeared to be more sensitive to temperature. On the other hand, the amount of HHC within samples has a significant influence on the P- and S-wave velocity variations over the entire investigated temperature range. In fact, for low HHC-bearing samples I observed a linear reduction of velocities with increasing temperature, whereas the velocity variations in high HHC-bearing samples are represented by distinct trends at around 50°-60 °C, suggesting a change of the physical properties of hydrocarbon. Based on these laboratory observations, I developed a new model for the estimation of the P-wave velocity as a function of temperature (from 30° to 90° C) and testing this Vp model at different conditions of porosity, HHC content and/or HHC saturation. The model suggests that the velocity change seems to be more linked to the absolute volume of HHC respect to the sample saturation. Therefore, the results of this work on HHC-bearing carbonate rocks provide a direct link between Vp variations and hydrocarbon content at different temperatures, allowing in interpreting seismic properties variations as a direct evidence of heavy oil presence. These results improve the seismic survey for hydrocarbon detection, reservoir characterization and for production assessment and monitoring.

Moreover, I founded that P-wave velocity hysteresis measured at ambient pressure after 100 MPa of applied confining pressure, also suggest an almost ideal-elastic behaviour for heavy oil-bearing samples and more inelastic behaviours for clean samples. These data are confirmed by loading-unloading tests performed on the same lithology that show an average increase of both

strength and Young's modulus for HHC-bearing samples respect to clean samples. Thus, the presence of HHC strengthens and stiffens the reservoir.

The different measured mechanical properties from HHC-bearing to clean samples in laboratory are in good agreement with outcrop observations showing a less fractured HHC-bearing portions respect to clean outcrops. Fractures characterizing HHC-bearing and clean outcrops differ in frequency but have very similar orientation suggesting that they formed under the same stress field. This implies that when the fracturing occurred HHCs were already in place limiting the formation of fractures.

Chapter 2

The role of shale content and pore-water saturation on frictional properties of simulated carbonate faults

Abstract

In this Chapter I present the experimental dataset derived by frictional tests, designed to investigate the frictional properties of carbonate-bearing faults. Faults are complex structure, and they experience a broad range of slip behaviour, from aseismic creep to a seismic slip and this can be correlated with a mechanical heterogeneity, such as the presence of clay minerals. In fact, the presence of clay minerals in mature carbonate fault zones has been invoked to explain the slip behaviour of weak faults. Notwithstanding the key role of heterogeneities in slip behaviour of faults, the relation between frictional strength, fault stability, mineralogical composition, and fabric of fault gouge, composed of strong and weak minerals, is poorly constrained. I used a biaxial apparatus to systematically shear different mixtures of shale (68% clay, 23% quartz and 4% plagioclase) and calcite, as powdered gouge, at room temperature, under constant normal stresses of 30, 50, 100 MPa and under room-dry and pore fluid-saturated conditions, i.e., CaCO3-equilibrated water. I performed 30 friction experiments during which velocity-stepping and slide-hold-slide tests were employed to assess frictional stability and to measure frictional healing, respectively. Laboratory frictional data indicate that the mineralogical composition of fault gouges significantly affects frictional strength, stability, and healing as well as the presence of $CaCO_3$-equilibrated water. Under room-dry condition, the increasing illite content determines a reduction in frictional strength, from μ=0.71 to μ=0.43, a lowering healing rates and a transition from velocity-weakening to velocity-strengthening behaviour. Under wet condition, with increasing illite content I observe a more significant reduction in frictional strength (μ=0.65-0.37), a near-zero healing and a velocity strengthening behaviour. Microstructural investigations evidence a transition from localized deformation promoted by grain size reduction, in calcite-rich samples, to a more distributed deformation with frictional sliding along clay-enriched shear planes in samples with shale content greater than 50%. For faults cutting across sedimentary sequences composed of carbonates and clay-rich sediments, these results suggest that clay concentration and its ability to form foliated and interconnected networks promotes important heterogeneities in fault strength and slip behaviour.

2.1 Frictional behaviour of carbonate-bearing faults

The frictional behaviour of fault rocks is controlled by the interaction of several factors, such as mineral composition, hydraulic properties, state of stress and distribution of strain in the surrounding fault rock and gouge layer (e.g., Sibson 1977; Faulkner et al., 2010; Fagereng and Sibson, 2010; Collettini et al., 2019). In this study I examine the influence of mineralogical composition, pore fluid presence and microstructural texture on frictional properties of carbonate-bearing faults.

Early laboratory experiments conducted on a great variety of rocks showed that friction is almost independent of rock type and it is in the range of μ = 0.6-0.85 (Byerlee, 1978). However, it is widely documented that along mature fault zones fluid-rock interaction can promote fluid-assisted dissolution and precipitation processes characterized by the replacement of strong granular mineral phases with weak platy phyllosilicates (Wintsch et al., 1995; Renard et al., 1997; Vrolijk and van der Pluijm, 1999; Faulkner et al., 2003; Collettini and Holdsworth, 2004; Jefferies et al., 2006; Solum and van der Pluijm, 2009; Fagereng and Sibson, 2010; Gratier et al., 2013; Collettini et al., 2019). Examples of fluid-assisted reaction softening from carbonates are documented along strike-slip (Kaduri et al., 2017), normal (Collettini et al., 2009; Hayman, 2006; Bullock et al., 2014; Smeraglia et al., 2017) and thrust faults (e.g., Tesei et al., 2013; Viti et al., 2014). On these faults, fracturing, fluid-rock interactions and dissolution of the carbonates facilitate the development of smectite-illite networks within fault gouges, with increasing illite concentration with depth, i.e., for temperature above 100-150 °C (Pytte and Reynolds, 1989; Saffer and Marone, 2003; Tesei et al., 2015).

A large number of laboratory experiments have documented that with increasing clay content fault gouges exhibit a significant reduction in frictional strength and a more stable sliding behaviour with little or no time-dependent friction re-strengthening (e.g., Marone et al., 1990; Marone, 1998a; Saffer et al., 2001; Saffer and Marone, 2003; Ikari et al., 2009; Niemeijer et al., 2010; Tesei et al., 2012, 2014; Collettini et al., 2019). However, despite the fact that clay-rich fault rocks have long attracted attention of experimentalists (e.g., Morrow et al., 1992; Tembe et al., 2010; Saffer and Marone, 2003; Ikari et al., 2009; Kohli & Zoback, 2013; Orellana et al., 2018; Scuderi and Collettini 2018; Rabinowitz et al., 2018), the role of clay minerals in the evolution of frictional properties of carbonate faults have not been systematically explored. The role of clay content in the frictional properties of carbonate-bearing faults is of particular interest since numerous faults, that cut across sedimentary sequences composed of carbonates and clay rich sediments, are located in seismically active regions such as the Apennines in Italy (Miller et al., 2004; Mirabella et al., 2008; Valoroso et al., 2014, Baccheschi et al., 2020), the

Gulf of Corinth in Greece (Bernard et al. 1997) and the Wenchuan county in China (Burchfiel et al., 2008). Cases of induced seismicity in carbonate lithologies have been documented at the Val d'Agri oil field in southern Italy (Improta et al., 2017), at the Lacq gas field in southwest France (Bardainne et al., 2008), in Oklahoma (e.g., Keranen et al., 2014) and in Canada (Eyre et al., 2019).

To fill this knowledge gap, I carried out frictional experiments on binary mixtures composed of calcite and shale mineral phases over a range of normal stresses, 30-100 MPa, under room-dry and $CaCO_3$-equilibrated water conditions. In these experiments, I conducted velocity-stepping tests (0.1-300 µm/s) and slide-hold-slide tests (30-3000 s of hold) to evaluate how various amounts of clay influence frictional stability and frictional healing, respectively. Finally, I recovered sheared gouge samples for microstructural investigations which I linked with mechanical data.

2.2 Experimental Methods

2.2.1 Sample preparation

Experiments were conducted on simulated gouges prepared by mixing various proportion of calcite mineral and shale rock. The calcite powder was obtained from natural limestone from the Caramanica Formation (Gargano Promontory, near Monte Sant'Angelo village) (Hairabian et al., 2015) and the grain density of this limestone is 2.72 g/cm^3, in good agreement with literature data for pure calcite rocks (Jaeger et al., 2007; Makvo et al., 2009). The shale powder derived from the Rochester Shale, which is an illite-rich shale outcropping in New York (the same rock as in Saffer and Marone, 2003). From X-ray diffraction analysis this illite-rich shale is primarily composed of clay minerals (68%), quartz (23%) and plagioclase (4%). The clay-rich fraction consists of 87% illite and 13% kaolinite/dickite. The starting material of our experiments was obtained by crushing the rocks and passing through a 63 μm sieve.

All friction experiments were performed in double-direct shear configuration using a servo-controlled biaxial testing apparatus, BRAVA (Collettini et al., 2014b) (Figure 2.1a). The horizontal servo-controlled hydraulic piston was used to apply and maintain a constant load normal to the gouge layers, while the vertical servo-controlled hydraulic piston was used to apply shear load at constant displacement rate (Figure 2.1a). Loads were measured using two strain gauged load cells (accuracy ±0.03 kN), positioned at the end of the ram and in contact with the sample assembly. Horizontal and vertical displacements were measured by LVDTs (linear variable differential transformers) with a resolution of ±0.1 μm and were corrected for the elastic stiffness of the loading frame. Double-direct shear configuration consists of two identical layers of simulated gouges sandwiched between three stainless steel forcing blocks (Figure 2.1b): a central forcing block and two stationary side blocks (e.g., Mair and Marone, 1999; Ikari et al., 2011). The surfaces of the steel sliding blocks in contact with gouge layers were machined with grooves 0.8 mm high and spaced 1 mm to avoid slip at the interface between gouges and steel and to ensure shear deformation within the gouges. Simulated gouge layers were prepared by smoothing the powdered materials with a levelling jig in order to obtain a uniform layer with an initial thickness of 5 mm and a nominal area of 5 x 5 cm, which was maintained constant during each experiment. The composition of simulated gouge layers varied between 100% and 0% wt. of calcite, within which Rochester shale (hereafter named Shale) ranges from 0 to 100% wt. (Table 2.1).

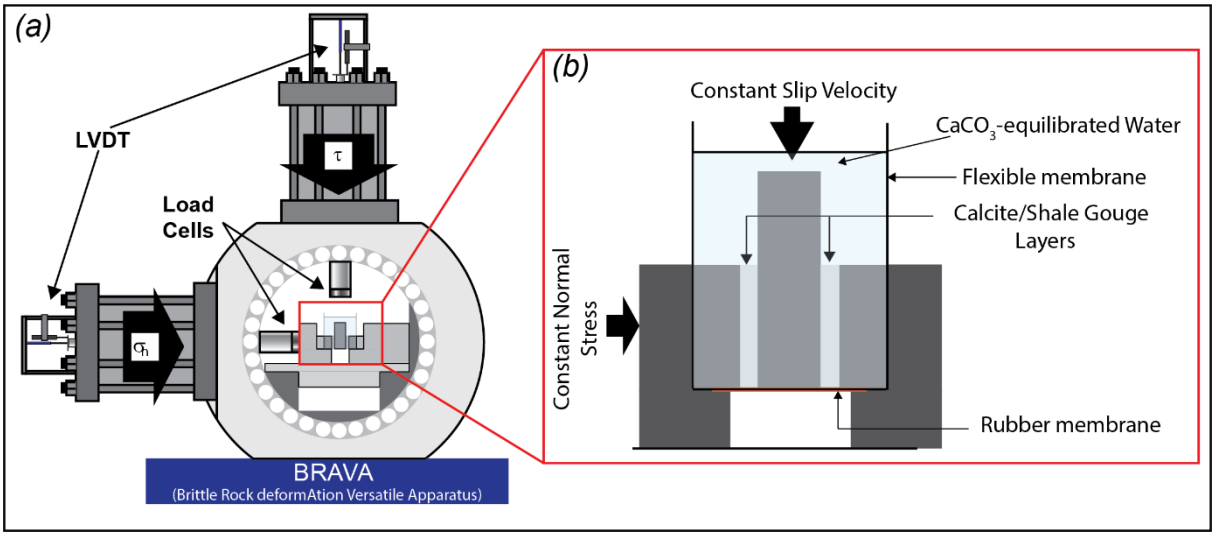

***Figure 2.1**: (a) Schematic diagram of the BRAVA rock deformation apparatus (Collettini et al., 2014b). (b) Details of the double-direct shear configuration, where two identical layers of simulated gouges were sandwiched between three stainless steel forcing blocks. For wet experiments, the $CaCO_3$-equilibrated water was added into a flexible, plastic membrane surrounding the sample (modified after Mercuri et al., 2018).*

Room-dry conditions			***Wet conditions***		
Experiment number	Calcite/Shale [wt.%]	Normal stress, σ_n [MPa]	Experiment number	Calcite/Shale [wt.%]	Normal stress, σ_n [MPa]
b769	100/0	30	b799	100/0	30
b770		50	b806		50
b798		100	b811		100
b773	70/30	30	b800	70/30	30
b782		50	b807		50
b797		100	b812		100
b772	50/50	30	b801	50/50	30
b781		50	b808		50
b796		100	b814		100
b784	30/70	30	b803	30/70	30
b786		50	b809		50
b787		100	b815		100
b771	0/100	30	b802	0/100	30
b779		50	b810		50
b780		100	b816		100

Table 2.1*: List of experiments under room-dry and wet conditions, mineralogical composition of gouges and the applied normal stresses. The shale is primarily composed of clay minerals (68%), quartz (23%) and plagioclase (4%). The clay-rich fraction consists of 87% illite and 13% kaolinite/dickite. The starting material of our experiments was obtained by crushing the rocks and passing through a 63 µm sieve.*

2.2.2 Testing procedure

I conducted 30 friction experiments over the range of normal stress from 30 to 100 MPa, under both room-humidity (room-dry) and $CaCO_3$-equilibrated water (wet) conditions, as reported in Table 2.1. Wet experiments were performed under drained conditions. For reproducibility and comparison purposes, all experiments followed the same experimental protocol (Figure 2.2a). After positioning the sample assembly in the biaxial loading frame, I started by applying normal stress with the horizontal ram, initially controlled in displacement feedback mode until a small load force of 1kN was reached. At this stage, I switched the horizontal piston control in a load feedback mode and normal load was increased with steps of 1kN every 20-10 seconds until the target normal stress was achieved. I left the sample to compact until a steady value of the layer thickness was attained and I maintained normal stress constant throughout the experiment. For experiments under wet conditions, before reaching the target value of normal stress, I allowed sample to saturate for 40 minutes with a water saturated in $CaCO_3$ at 1kN of horizontal force. This was necessary to ensure that the water penetrated within the gouges. Subsequently, after the compaction of the sample, I applied shear stress by advancing the vertical ram at constant displacement rate of 10 μm/s until a steady state shear at constant friction was achieved (Figure 2.2a). After this phase "run-in", velocity steps and slide-hold-slide sequences were performed for each experiment to characterize the velocity and time dependence of friction, respectively. In the velocity step sequences, the sliding velocity was changed from 0.1 to 300 μm/s with a shear displacement of 500 μm during each step (Figure 2.2b). The slide-hold-slide (SHS) sequences were conducted at constant shear velocity of 10 μm/s alternating with hold periods, where the sample was maintained under quasi-stationary contact, of 30, 100, 300, 1000 and 3000 s with 500 μm displacement after each hold (Figure 2.2c). These procedures allow to attain a general steady-state friction for velocity steps and slide hold slide. All digital data were recorded with a simultaneous multichannel analog to digital converter at a sampling rate of 10 kHz and then down sampled to 1-100 Hz, depending on the shearing velocity.

At the end of each experiment, I collected the deformed gouge layers and prepared thin sections oriented parallel to the sense of shear for microstructural analysis using a Scanning Electron Microscope (SEM) in backscatter mode.

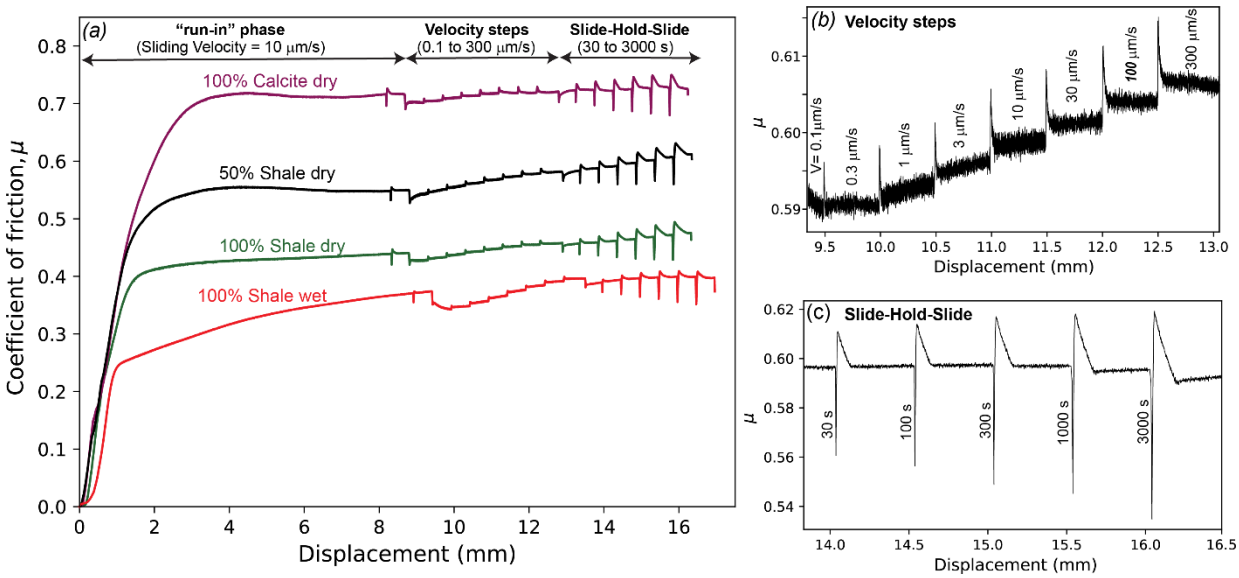

***Figure 2.2**: (a) The evolution of friction coefficient as a function of displacement for four representative experiments, run at normal stress of 100 MPa. During the "run-in phase", at loading rate v=10 μm/s, friction increases until a steady state value is achieved. After the run-in phase, velocity steps are performed to evaluate the frictional velocity dependence, followed by a slide-hold-slide sequences used to measure the re-strengthening of the simulated fault gouge. (b) Details of the velocity steps (from 0.1 to 300 μm/s) and (c) Slide-Hold-Slide (from 30 to 3000 s) sequences.*

2.2.3 Data analysis

In the experiments, I calculated the friction coefficient (μ) from the Coulomb criterion, as the ratio of shear stress (τ) and normal stress (σ_n), assuming that the cohesion in the powdered gouges is negligible.

To analyse the velocity dependence of friction and fault stability, I employed the framework of the rate and state constitutive equations (RSF) (Dieterich, 1978, 1979; Ruina, 1983; Marone, 1998b):

$$\mu = \mu_0 + a\, ln\left(\frac{V}{V_0}\right) + b\, ln(\frac{V_0\, \theta}{D_C}) \quad (2.1)$$

$$\frac{d\theta}{dt} = -\frac{v\theta}{D_c}\ln(\frac{v\theta}{D_c}), \quad (2.2)$$

where μ0 denotes the friction value before the velocity step (at sliding velocity V0), whereas μ represents the friction after the velocity step (at sliding velocity V); θ is the state variable, which may be interpreted as an evolution of contact life time; Dc is the critical slip distance, which refers to the slip necessary to regenerate a new population of contacts after the velocity change; a and b are empirically derived constants, representing the direct effect and the evolution effect, respectively. To account for the evolution of the state variable in this work I adopted the Ruina "slip law" (Equation 2.2). Therefore, I model the velocity stepping data coupling the constitutive law and the evolution equation (equations 2.1 and 2.2) with equation 2.3, which describes the elastic interaction of the sample with the finite stiffness of the testing machine:

$$\frac{d\mu}{dt} = k(V_{lp} - V) \quad (2.3)$$

where k is the stiffness of the testing apparatus and the sample blocks, normalized by the normal stress, Vlp is the load point velocity and V is the slip velocity. Therefore, the constitutive parameters (a, b and Dc) were obtained as the best fit of our velocity step data by solving equations (2.1), (2.2) and (2.3) and using an iterative, least-squares method (e.g. Reinen and Weeks, 1993; Blanpied et al., 1998; Saffer and Marone, 2003).

To assess frictional stability, I defined the friction rate parameter (a-b):

$$a - b = \frac{\Delta\mu_{ss}}{\ln\left(\frac{V}{V_0}\right)} \quad (2.4)$$

where $\Delta\mu_{ss}$ indicates the change in the steady state friction coefficient following the change in sliding velocity.

Positive values of (a-b) indicate velocity strengthening behaviour (i.e., friction coefficient increases with increasing sliding velocity) resulting in stable sliding and aseismic slip, whereas negative values of (a-b) reflect velocity weakening behaviour which is a condition required to develop slip instability (e.g., Ruina, 1983; Marone, 1998a). After velocity steps, to characterize the recovery of frictional strength necessary to generate a new instability, SHS sequences were performed. I refer to the frictional re-strength with the term of "frictional healing" ($\Delta\mu$), defined as the difference between the peak friction, μ_p, and the steady state friction, μ_{ss} (Figure 2.3b). The steady state friction is the friction before the hold, whereas the peak friction is defined as the maximum value of friction reached after a hold period, when the sliding velocity of the simulated fault gouge is resumed at the same pre-hold rate (10 μm/s). The rate of the fault strength recovery (healing rates), β, is given by:

$$\beta = \frac{\Delta_\mu}{\log(t_h)} \tag{2.5}$$

where t_h is hold time in seconds. Higher healing rates indicate material strengthening during hold periods, whereas lower healing rates indicate time-dependent weakening (e.g., Marone, 1998b; Carpenter et al., 2011).

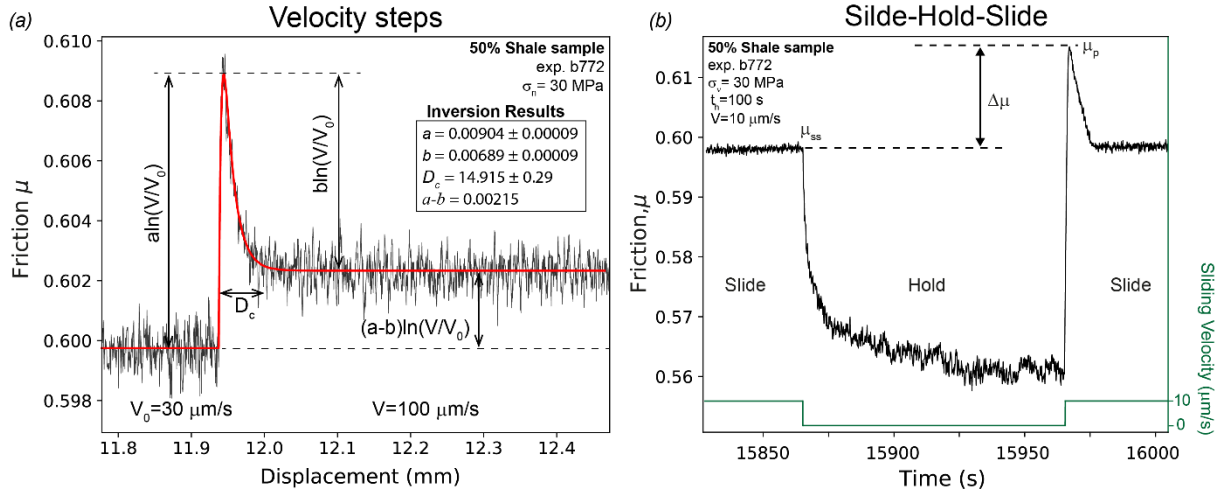

***Figure 2.3**: (a) Details of a representative velocity step, from 30 to 100 μm/s, with raw data (black line) and the best-fit of the modelled evolution of friction as a function of displacement; (b) Details of a representative slide-hold-slide sequence for a 300 s hold. Δμ is the difference between the peak friction (μ_p), reached after the hold and the steady state friction (μ_{ss}) in the pre-hold phase.*

2.3 Results

2.3.1 Frictional Strength

During our friction experiments, I recorded continuously shear strength (τ) of the simulated gouge and its evolution with sliding displacement. To compare our experimental frictional data among all investigated mixtures, I picked the steady state friction values at the end of the "run-in" phase for all gouges. Overall, the steady state sliding friction was reached after displacements of ~ 6-8 mm for room-dry experiments and ~ 7-9 mm for water-saturated experiments (Figure SB.1 in Appendix B).

In Figure 2.4, I show the steady state shear strength as a function of normal stress for room-dry (Figure 2.4a) and wet (Figure 2.4b) experimental conditions. For all gouges, the shear stress is characterized by a linear relation with the normal stress that is consistent with the Coulomb failure envelope. The average coefficient of friction, calculated as the slope of the Coulomb failure envelope of each calcite-shale mixture, shows the influence of both shale content and water in fault strength. With increasing shale content, the coefficient of friction decreases from 0.71, for pure calcite, to 0.43, for shale under room-dry condition and from 0.65 to 0.37 under wet condition. Furthermore, at constant shale content the presence of fluids causes an average decrease of frictional strength of about 16%.

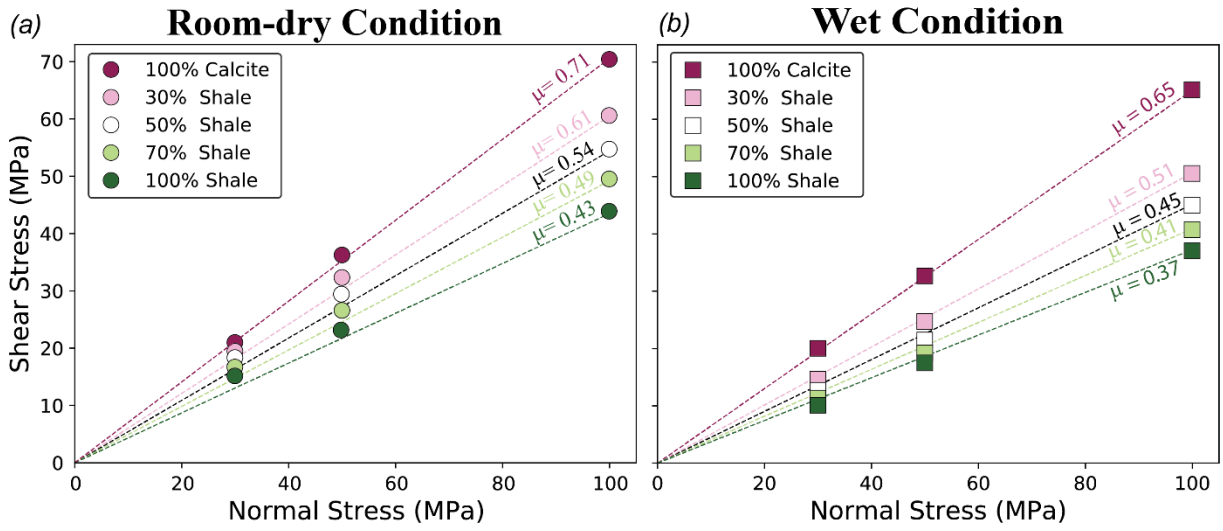

***Figure 2.4**: Shear stress as a function of normal stress for all mixtures investigated under both (a) room-dry condition (symbolized by circles) and (b) wet condition (symbolized by squares). Dashed lines show the Coulomb failure envelope for each fault gouge type.*

2.3.2 Rate and State friction parameters

The relationship between the friction rate parameter *(a-b)*, shale content and shear velocity is illustrated in Figure 2.5 for room-dry (top panels) and wet (bottom panels) experimental conditions at normal stress of 30, 50, 100 MPa. Experiments performed under room-dry condition (top panels in Figure 2.5) show a strong dependence of the rate parameter (*a-b*) as a function of shale content. At low shale content, up to 50%, and normal stress of 30 MPa (Figure 2.5a), I observed velocity-weakening behaviour *(a-b<0)* at low shearing velocity that gradually evolves to velocity-strengthening as shear velocity increases. Above shale content of 50%I document a persistent velocity-strengthening behaviour. Increasing normal stress to 50 MPa suppresses the velocity-weakening behaviour observed at low shale content andI observe an overall velocity strengthening response to increasing shear velocity (Figure 2.5b). At higher normal stress of 100 MPa (Figure 2.5c), with increasing shearing velocity all gouges exhibit a double trend of *(a-b)*: up to 30 μm/sI observe an increase of *(a-b)* from 0.0015 to 0.0032, then values of *(a-b)* start to slightly decrease up to 0.0011 at 300 μm/s of sliding velocities.

Under wet conditions (bottom panels in Figure 2.5), all mixtures exhibit velocity-strengthening behaviour (a-b>0) over the entire range of both shear velocity and normal stress (Figures 2.5d-5f). For shale-rich mixtures the friction rate parameter (a-b) is within a restricted range, 0.0038<a-b<0.0063, showing a negligible variation within the range of applied normal stresses. Pure calcite gouges show a velocity-strengthening behaviour within the entire range of sliding velocities and applied normal stress. The friction rate parameter (a-b) increases up to 3 μm/s in sliding velocity and then decreases with sliding velocity.

.

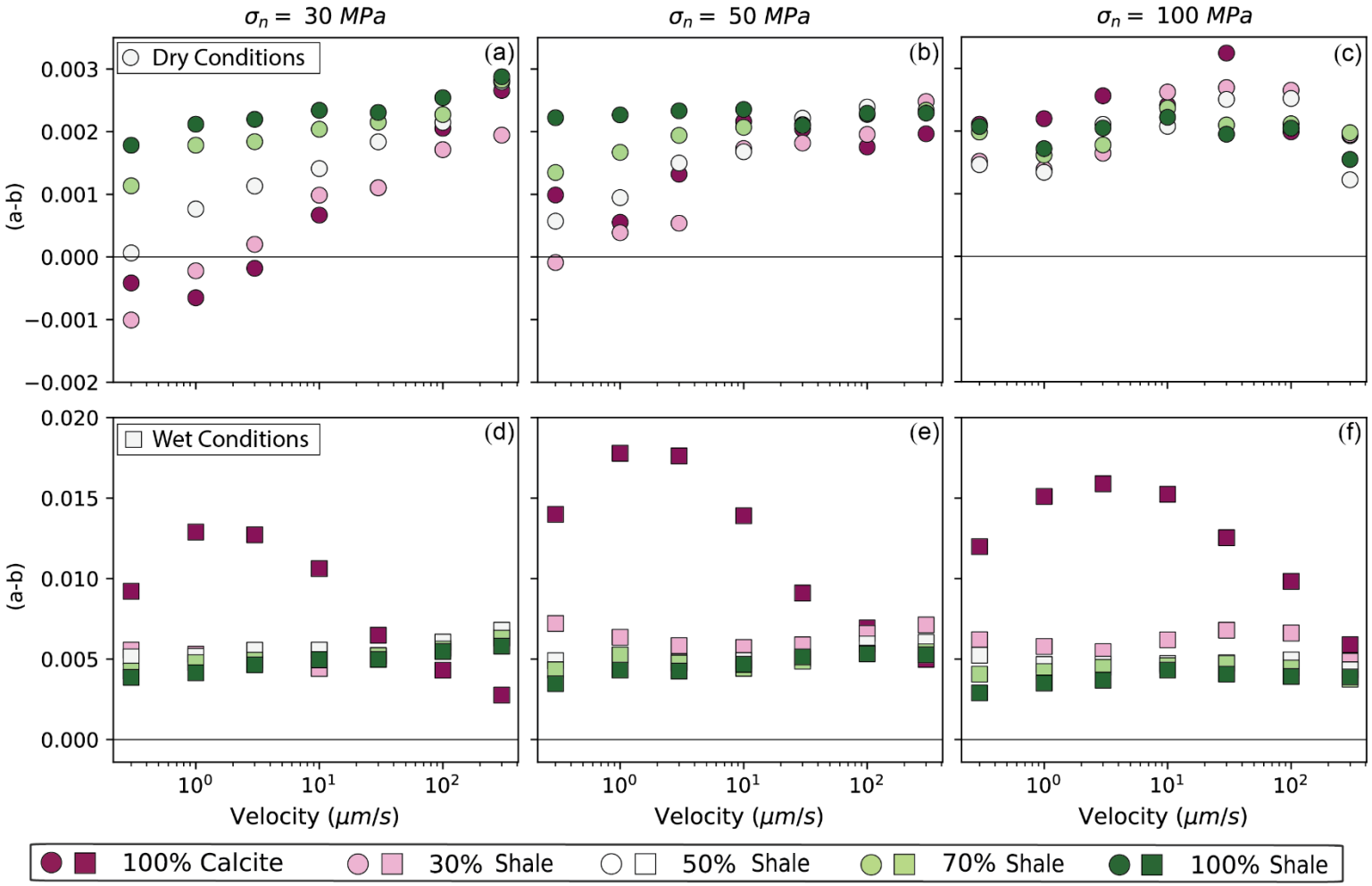

***Figure 2.5**: Frictional constitutive parameters (a-b), shown as a function of sliding velocity for room-dry (symbolized by circles) and wet conditions (symbolized by squares) at different applied normal stresses of 30 MPa (a and d), 50 MPa (b and e) and 100 MPa (c and f). Different colours represent different shale content. The line at zero value of (a-b) represents the transition from velocity-weakening to velocity-strengthening behaviour.*

2.3.3 Frictional healing

After velocity stepping tests, I performed Slide-Hold-Slide (SHS) sequences. Frictional healing data ($\Delta\mu$) are presented in Figure 2.6 as a function of the logarithm of hold time (t_h) and shale content for room-dry and wet experimental conditions at each investigated normal stress. Overall, I observe that frictional healing depends both on hold time and mineralogical composition of mixtures: $\Delta\mu$ increases linearly with the hold time and reduces with increasing of shale content. Moreover, the frictional healing measured in room-dry experiments are lower in magnitude than in the wet experiments at the same conditions of hold time and mineralogical composition.

The rates of frictional healing, β (equation 2.5), are also reported in Figure 2.6. For room-dry experiments (top panels in Figure 2.6) I observe that the healing rates are in the range of 0.0062-0.0023, slightly increasing with normal stress and slightly decreasing with the addition of shale content. For samples with < 50% shale β is in the range of 0.0055-0.0045, whereas when the samples containing > 50 % shale, β is in general slightly lower, spanning between 0.0062 and 0.0023, with the lowest value of β corresponding to shale sample.

In wet experiments (bottom panels in Figure 2.6), healing rates are in the range of $-0.0045 < \beta < 0.0195$ and show higher variations respect to the room-dry tested samples, suggesting a strong influence of pore fluid on fault re-strengthening. Under wet condition, the healing rates of the pure calcite gouge decrease from 0.0195 to 0.0099 at normal stress from 30 to 100 MPa (Figure 2.7). With the addition of shale content (> 50%), the rates of frictional healing show a progressive reduction, reaching values of $0.0045 < \beta < 0.0007$ for pure shale gouges between normal stresses of 30 and 100 MPa (Figure 2.7).

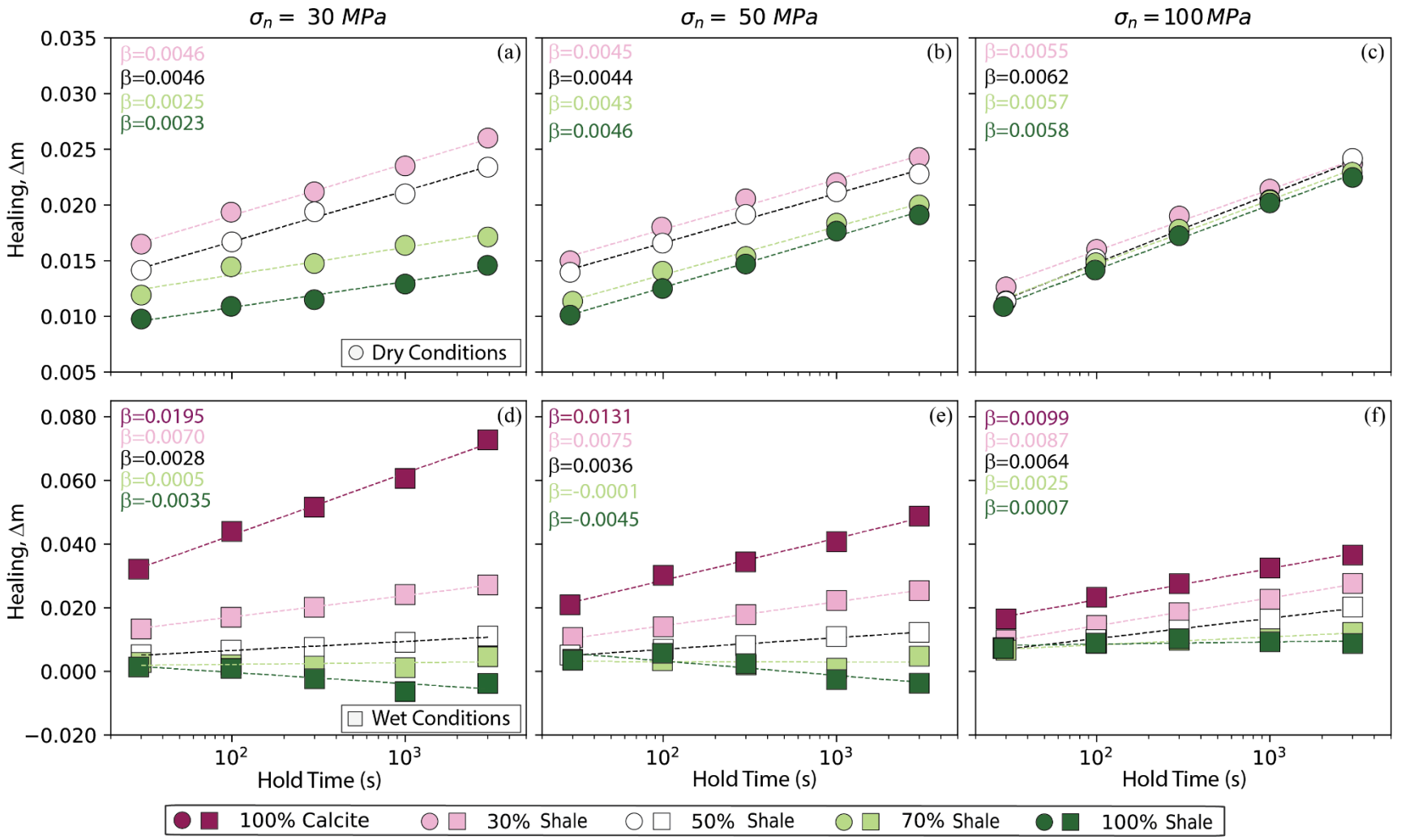

***Figure 2.6**: Frictional healing as a function of the logarithm holding time for room-dry (symbolized by circles) and wet conditions (symbolized by squares) at different applied normal stresses of 30 MPa (a and d), 50 MPa (b and e) and 100 MPa (c and f). Different colours represent different shale content.*

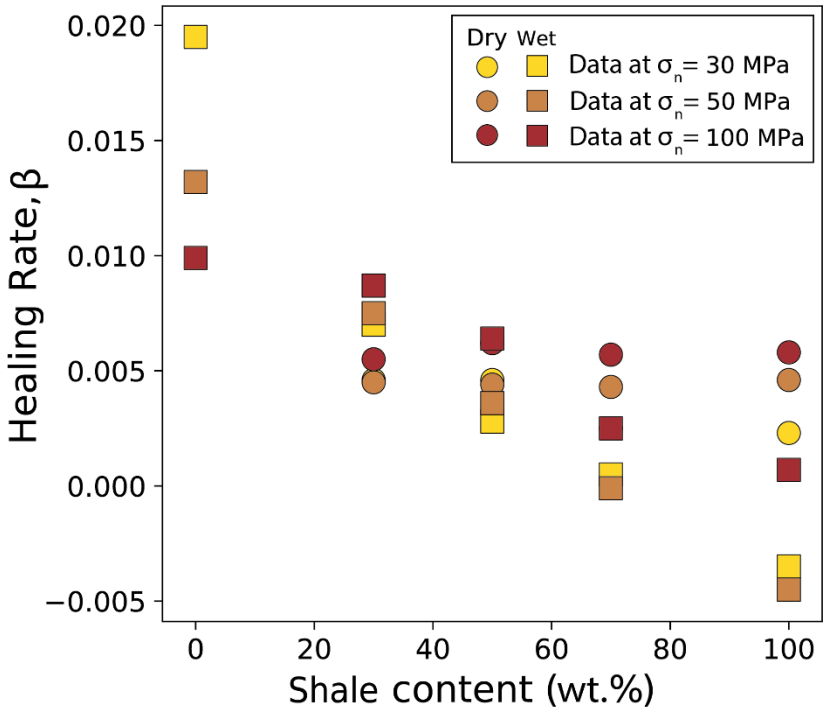

***Figure 2.7**: Frictional healing rates (β) as a function of illite content for room-dry (symbolized by circles) and wet (symbolized by squares) experiments at normal stresses of 30, 50 and 100 MPa.*

2.4 Microstructural observations

Microstructural observations were carried out on sheared gouges collected at the end of the experiments performed at 100 MPa. These selected experiments were chosen to investigate the microstructures stress values that are indicative of seismogenic depths within carbonate rocks (e.g., Mirabella et al., 2008). I present microstructures for both dry and wet conditions of three mixtures: 100% calcite gouge, 50/50 mixture of calcite and shale and 100% wt. shale gouge. Laboratory experience on experimental faults composed of mixtures of weak and strong mineral phases (e.g., Tembe et al., 2010; Moore and Lockner, 2011; Giorgetti et al., 2015) suggests that the three selected end-members can capture the main differences in fault structure and deformation mechanisms that influence the mechanical data. In the following microstructural analysis, I refer to the entire width of the deformed gouge as experimental fault developed during the experiment. Within experimental fault the localization of the deformation occurs along different sliding surfaces, known as Riedel (R_1), Y and boundary (B) shear planes (Logan et al., 1992).

2.4.1 Microstructures of the dry deformed gouges

In the 100% dry calcite gouge, I observe numerous Riedel (R_1) shear planes oriented with en-echelon geometry and linked occasionally with sub-horizontal fractures (Figure 2.8a). The orientation of R_1 planes is not constant and, in some places, they are interrupted by sub-horizontal Y shear planes or they merge into the B-shear planes. Along R_1 and Y shear planes the deformation tends to be more localized with intense grain size reduction in the order of submicron scale (Figure 2.8b). Away from the shear planes the original grain-size is mostly preserved and some angular calcite grains appear intensely fractured with structures indicating rotation, translation, and frictional sliding at grain contacts (Figure 2.8c).

The 100% dry shale gouge shows a texture dominated by a minor amount of R_1 shear planes with respect to the calcite gouge (Figure 2.8d). Some clay minerals are aligned parallel to shear direction and others describe a P foliation (Figure 2.8e). In some portions of the gouge, clay lamellae are occasionally deformed by kinking and folding. More competent material (i.e., quartz) are inter-dispersed within the shale-rich foliation and some of them show intergranular fractures and/or truncations (Figure 2.8e).

In the dry gouge of mixed composition, the microstructure presents features that are intermediate between the two end-members (100% calcite and 100% shale) described above. R_1 and proto-B shear planes are present (Figure SB.2a in Appendix B) and granular mineral

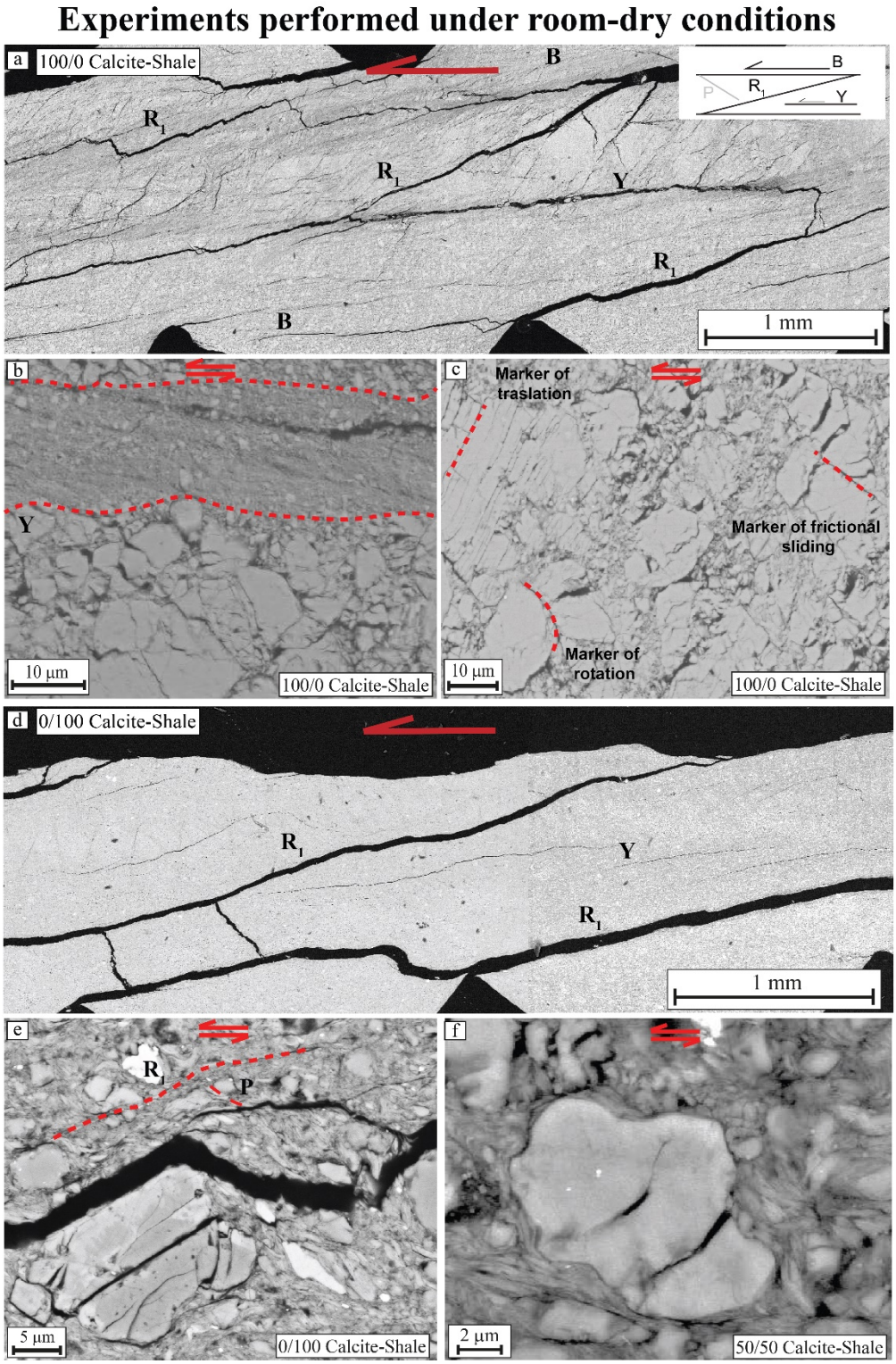

***Figure 2.8**: SEM images of the sheared gouge samples tested at 100 MPa normal stress and under room-dry conditions for the end-members where we recognized a YPR geometry. (a) Simulated gouge composed of 100% calcite. (b) Zoom of Y shear plane characterized by grain size reduction. (c) Detail of intergranular fractures of calcite grains indicating rotation, translation, and frictional sliding at grain contacts. (d) Simulated gouge composed of 100% shale. (e) R1 shear plane with some fractured minerals and the iso-orientated clay minerals along R1 and P-orientations. (f) Detail of 50/50 calcite-shale mixture where clay minerals form the interconnected and anastomosing network around more competent calcite grains, which present some intergranular fractures.*

phases, such as calcite and quartz clasts, are occasionally fractured and surrounded by foliated clay lamellae, which form an interconnected foliation wrapping around clasts (Figure 8f).

2.4.2 Microstructures of the wet deformed gouges

In the 100% wet calcite gouge, I observe a network of R_1 shear planes that extended across the entire experimental fault (Figure 2.9a). As observed in dry calcite gouge, R_1 shear planes are linked with discrete Y-planes describing a staircase geometry. In this fault gouge, B shear planes are more continuous and fully developed along both sides of the shear plane. Both B and R_1 shear planes are 100-200 μm and 20-40 μm thick, respectively, and are characterized by intense grain size reduction (Figure 2.9b). Within and around the B and R_1 shear planes, calcite grains with dimensions up to around 50 μm are characterized by pervasive intergranular fractures often occurring along the pre-existing twinning planes (Figure 2.9c).

In the 100% wet shale gouge, deformation is homogeneously distributed within the entire experimental fault, where R_1 planes are mainly rotated into the Y orientation. Some remnant R_1 planes are formed at low angle to the shear direction (Figure 2.9d). Within the experimental fault, the bulk microstructure consists of fine matrix with a few competent grains (i.e., quartz) with dimensions in the order of 10-23 μm and without intergranular fractures (Figure 2.9e). In some portions of gouge, clay minerals are deformed by kinking and folding, while elsewhere they are oriented parallel to the shear direction or define a P foliation (Figure 2.9e).

The microstructure of the 50% shale samples shows intermediate features between the two end-members. Across the fault gouge, R_1 planes are developed and are rotated in sub-horizontal Y-direction or merge into the B plane, about 150 μm thick (Figure SB.2b in the Appendix B). Within the shear planes, the fine matrix consists of grains <1μm in size, with irregular boundaries. Granular mineral phases (i.e., calcite and quartz) are present within the fine matrix, showing intergranular fractures. As observed in the dry gouge of mixed composition, clay lamellae form an interconnected network enclosing granular mineral phase (Figure 2.9f).

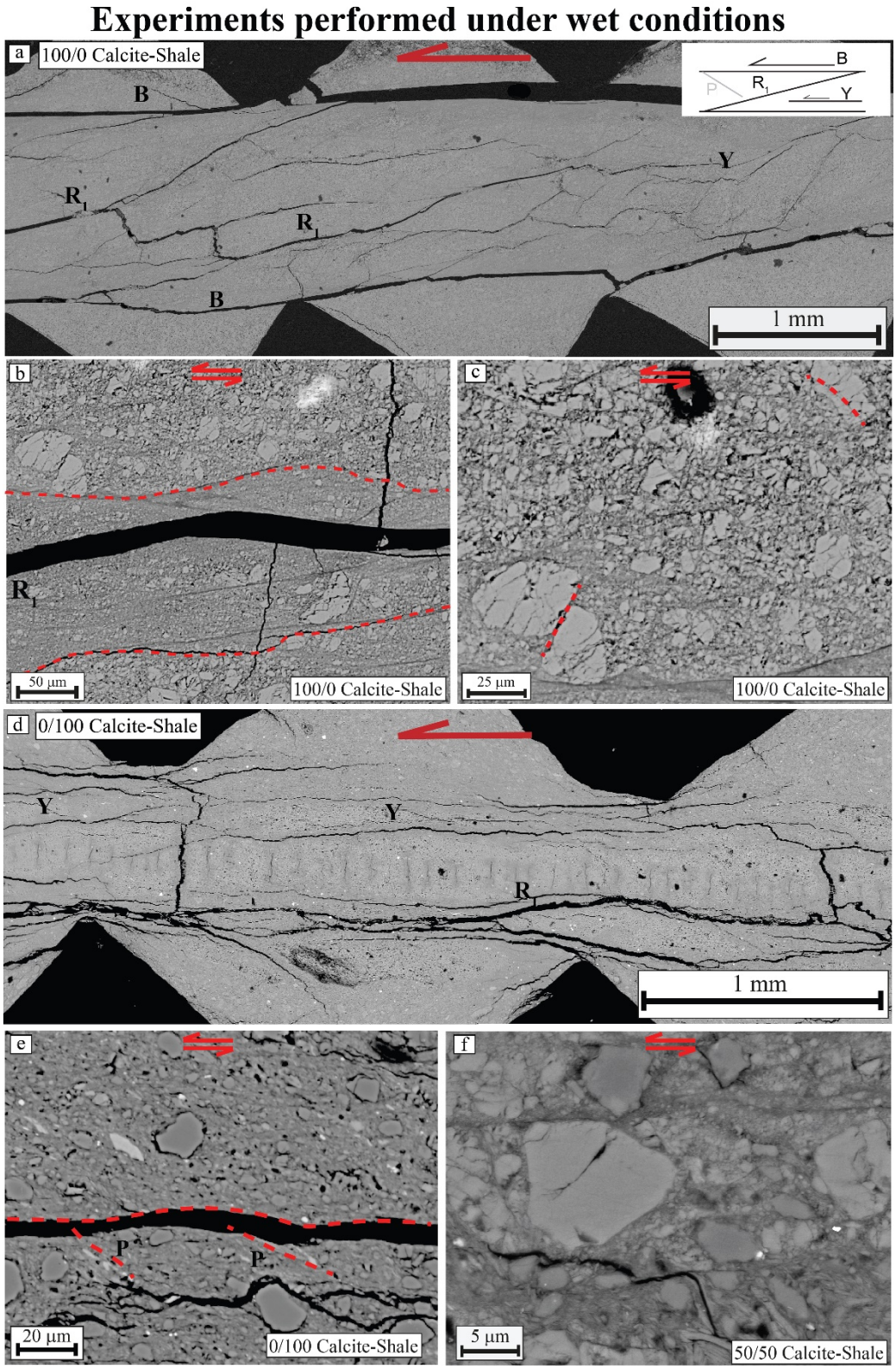

***Figure 2.9**: SEM images of the sheared gouge samples tested at 100 MPa normal stress and under $CaCO_3$-saturated conditions for the end-members where we recognized a YPR geometry. (a) Simulated gouge composed of 100% calcite. (b) Zoom of grain size reduction within R1 shear plane. (c) Detail of R1 shear band and P foliation. (d) Simulated gouge composed of 100% shale. (e) Zoom of P foliation along which clay lamellae are aligned. (f) Detail of 50/50 calcite-shale mixture where clay minerals are around more competent grains (e.g., quartz and calcite), characterized by intergranular fractures.*

2.5 Discussion

2.5.1 Integration of mechanical and microstructural data

Laboratory data show that starting from a calcite gouge the increasing shale content causes a reduction in frictional strength (Figures 2.4 and 2.10). This frictional weakening is accompanied by significant differences in the experimental fault microstructures. The 100% calcite gouges consist of a load-bearing framework of calcite grains where deformation occurs by grain size-reduction and localization along BYR_1 shear planes (Figures 2.8a and 2.9a). On the other hand, in shale-rich gouges clay minerals tend to form interconnected layers where Y and rotated R_1 shear planes are linked with a P foliation, formed by aligned clay lamellae (Figures 2.8e-f and 2.9e-f). These microstructural observations, together with the documented reduction of friction with increasing shale content and the linear relationship between normal and shear stress (Figure 2.4), indicate that fault weakening is mainly due by frictional sliding along the clay lamellae. However, experiments using a stack of single phyllosilicate crystal sheets showed a coefficient of friction significantly below, i.e., << 0.1 (Okamoto et al., 2019), the data documented in this study (Figure 2.4). This suggests that frictional sliding along the phyllosilicate lamellae occurs in concert with other mechanisms, such as intergranular slip, folding, grain cleavage, rotation, and breakage (Behnsen & Faulkner, 2012; Moore & Lockner, 2004). Wavy structure of phyllosilicates, kinking with closely associated layer faults and flexures, interlayer delamination and phyllosilicate rotations are well documented at the nanoscale on natural phyllosilicate-rich shear planes (Viti and Collettini, 2009; Viti et al., 2014).

In Figure 2.10, I report our frictional data under room-dry and wet conditions within the entire range of the applied normal stress and, for comparison, I also include frictional data published by other studies analysing the role of weak phyllosilicates in frictional strength (Crawford et al., 2008; Tembe et al., 2010; Moore and Lockner, 2011; Giorgetti et al., 2015). Our data, at first approximation, are consistent with previous studies on mixtures composed by strong mineral phases, such as quartz or calcite, and weak platy mineral phases, such as talc and clays. The coefficient of friction for talc mixtures, investigated by Moore and Lockner (2011) and Giorgetti et al. (2015), is lower than our frictional data on shale mixtures. This difference can be attributed to the different strengths of the clay minerals and the presence of quartz within the tested shales. Moreover, calcite-shale mixtures, investigated in this study, present a more pronounced reduction in frictional strength for wet conditions.

This is likely due to: 1) the reduction in frictional strength produced by the adsorbed or interlayer water on sheet mineral structures (Morrow et al., 2000; Moore & Lockner, 2004) and 2) the higher strains achieved during wet experiments with the possibility to better develop the interconnected weak layer of shale lamellae.

Fault stability, evaluated by the analysis of the friction rate parameter *(a-b)*, defines a dominant velocity-strengthening behaviour not influenced by wet and room-dry conditions and applied normal stress. This is the typical velocity-strengthening behaviour documented for shale gouges (Morrow et al., 2000; Suffer and Marone, 2003; Tembe et al., 2010; Tesei et al., 2012, 2014; Scuderi and Collettini, 2018) and more in general for phyllosilicate-rich natural fault gouges (e.g., Ikari et al., 2011; Collettini et al., 2019). Dry calcite-rich mixtures, with the exception of a few velocity-weakening data at low normal stress and low sliding velocity, show a velocity-strengthening behaviour. Under wet conditions for calcite gouges I observe a strong velocity-strengthening behaviour at low sliding velocity, followed by a transition to velocity-weakening friction behaviour at the highest sliding velocity. I interpret this as a transition from a semi-brittle deformation, in part testified by folding and twinning (Figure 2.9c), favouring rate-strengthening at low sliding velocity (Carpenter et al., 2016; Mercuri et al., 2018) to a frictional dominated deformation at higher sliding velocity with localized deformation along B, Y and R_1 shear planes (Figure 2.9a). Temperature and therefore crustal depth also play an important role on the friction rate parameter *(a-b)*. Experiments on illite-quartz mixtures show a transition from velocity strengthening at low temperature to a velocity weakening behaviour for T > 250 °C (Den Hartog and Spiers, 2014). Calcite fault gouges show a similar velocity strengthening to weakening transition at T > 100°C (Verberne et al., 2015).

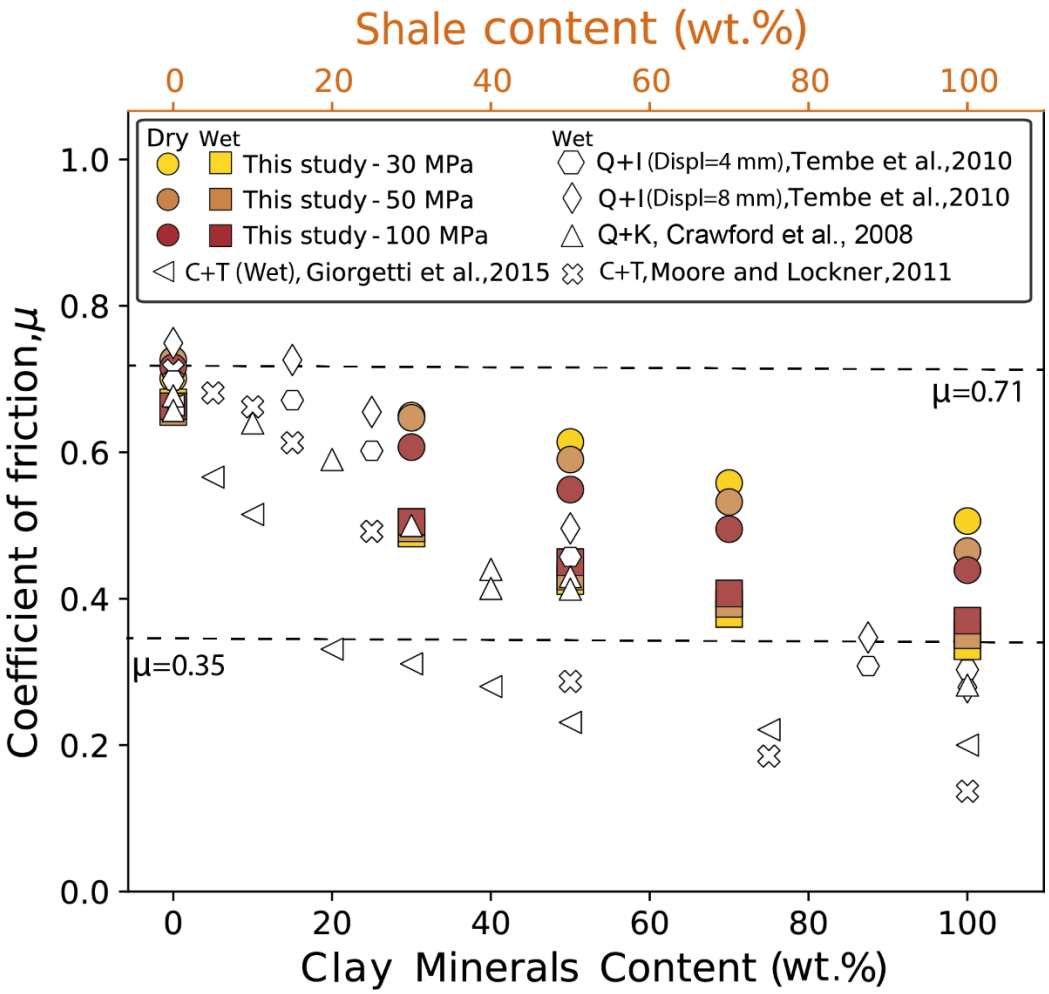

***Figure 2.10**: Evolution of the steady state coefficient of friction as a function of phyllosilicate mineral content. I report experimental results obtained from this work (calcite-shale mixtures) for all the normal stresses investigated (30, 50 and 100 MPa) under wet and room-dry conditions. For comparison, I report data obtained by frictional tests on analogues mixtures, symbolized by empty symbols (Crawford et al., 2008, Tembe et al., 2010; Moore and Lockner, 2011; Giorgetti et al., 2015). Q, C, I, T and K represent quartz, calcite, illite, talc and kaolinite, respectively.*

To study the frictional healing of the simulated fault gouges I adopt the Slide-Hold-Slide analyses. In room-dry experiments the healing decreases with the increase of shale percentage and the healing rates slightly increases with applied normal stress. In wet experiments I observe high healing rates for calcite and a significant reduction in the healing rates with increasing shale contents. For high shale contents the healing rate is close to or below zero in agreement with previous experiments on phyllosilicates (e.g., Beeler, 2007; Neimeijer and Spiers, 2006; Tesei et al., 2013; Giorgetti et al., 2015; Okamoto et al., 2020). I speculate that this lack of healing for shale-rich gouges is due toa reduction with hold time of grain contact strength, which would also lead to low values of frictional strength of the fault gouges (Carpenter et al., 2011). The comparison of dry and wet calcite-rich gouges suggests that the increase in healing in wet calcite gouges is promoted by fluid-assisted diffusion mass transfer (Tesei et al., 2012, 2014; Carpenter et al., 2016). Whereas for wet 100% calcite gouges, I observed an opposite trend, that is the reduction of healing rate with increasing normal stress (Figure 2.7). I propose that this distinct trend is likely due to a wide cumulative contact area within the gouge at higher normal stress that cannot grow significantly during the hold time. The reduction to null healing rates for shale-rich mixture under wet conditions is interpreted to be related to the higher strains achieved during these experiments. Increasing strains promote the development of continuous weak layers where clay lamellae are parallel to the foliation and during hold periods the lamellae quickly reach contact saturations with the resulting null healing (e.g., Saffer and Marone, 2003; Ikari et al., 2009; Tesei et al., 2012).

2.5.2 Implications for the slip behaviour of calcite-illite rich faults

In many active tectonic environments, there are numerous faults that cut across sedimentary sequences composed of carbonates and clay rich sediments: examples include the Apennines belt in Italy (e.g., Barchi et al., 1998), the Shimanto belt in Japan (Kimura et al., 2012), Hikurangi in New Zealand (Rabinowitz et al., 2018; Barnes et al., 2020), Cocos in central America and Nazca in south America (Vannucchi et al., 2017) subduction zones and the Longmenshan Fault Zone in the southwest China (Verberne et al., 2010). These faults are characterized by structural heterogeneities that are influenced by protolith lithologies (e.g., Lacroix et al., 2011; Kimura et al., 2012; Tesei et al., 2013; Smeraglia et al., 2017). In particular, in carbonates, deformation is localized along principal slipping surfaces formed by cataclastic processes (e.g., Smith et al., 2011; Collettini et al., 2014a; Smeraglia et al., 2017), whereas in marly limestones, fluid assisted dissolution and precipitation processes tend to form thick shear planes (e.g., Lacroix et al., 2011; Kimura et al., 2012; Tesei et al., 2013) made of interconnected

illite-smectite networks where slip occurs by frictional sliding along the phyllosilicate lamellae (Viti et al., 2014). Our laboratory and microstructural data can contribute to shading light on possible fault slip behaviours. Therefore, starting from a heterogeneous fault zone structure, consisting of thick portions dominated by clay lithologies and principal slipping zones formed within carbonate rocks (e.g., Tesei et al., 2014), the clay-rich patches are more prone to initiate slip during fault loading as they represent the weak fault portions (Figure 2.10). As these weak regions exhibit velocity-strengthening frictional behaviour (Figure 2.5), the fault should undergo stable sliding and aseismic fault creep. Continued creep, however, may increase shear stress (e.g., Cappa et al., 2019) on carbonate fault portions that are locked due to high frictional strength (Figures 2.4 and 2.10) and significant healing (Figure 2.6). If the shear stress reaches the strength of the carbonate-hosted faults, frictional reactivation occurs on carbonate patches too. There, the slip behaviour could be seismic due to the transition towards velocity-weakening behaviour of carbonates at high normal stress (Figure 2.5) and the more pronounced velocity-weakening behaviour of carbonates at temperature above 100 °C (Verberne et al., 2015). This behaviour has been recently documented during hydraulic fracturing in Canada (Eyre et al., 2019), where the integration of seismic reflection profiles with earthquake localization showed that accelerated creep, induced by hydraulic stimulations of shales, promoted a stress increase on adjacent fault patches hosted in carbonates where earthquakes nucleated.

2.6 Conclusions

I performed 30 frictional sliding experiments on simulated gouges composed of mixtures of shale and calcite under room-dry condition and in the presence of $CaCO_3$-pore fluid within a range of normal stresses (30-100 MPa) and sliding velocities (0.1-300 µm/s).
Starting from a calcite-bearing fault gouge the increasing shale content determines a significant reduction in friction from about 0.71 to 0.37. This frictional weakening is accompanied by an evolution from a load-bearing microstructure in calcite gouges, where deformation occurs by grain size-reduction and localization along BYR_1 shear planes, to interconnected layers of clays where Y and rotated R_1 shear planes are linked with a P foliation formed by aligned clay lamellae.

For gouges with a shale content ≥ 50% in weight, fault stability analysis of demonstrated a dominant velocity-strengthening behaviour that is not influenced by the presence of pressurized pore water and applied normal stress. Calcite-rich gouges show predominant velocity-strengthening behaviour at room-dry conditions, whereas pure calcite samples saturated with CaCO3-equilibrated water show a transition from strong velocity-strengthening to velocity-weakening with increasing sliding velocity. I associate this evolution to a transition from semi-brittle to a frictional dominated deformation with increasing sliding rates. High healing rates are observed for calcite gouges and a significant reduction in healing rates are due to the increasing shale contents, mainly under wet conditions.

Our laboratory and microstructural data suggest an heterogenous frictional behaviour that is controlled by the amount and connectivity of clay layers within the shear planes. In particular, clay concentration and interconnectivity promote fault weakening, hence facilitating fault reactivation. Upon reactivation the marked rate-strengthening behaviour of clay-rich shear planes point to a slip behaviour characterized by aseismic creep.

Chapter 3

3D structural model and hydrocarbon migration of the Burano-Bolognano petroleum system

Abstract

Typical final tasks in Petroleum System Modelling studies are building a 3D geological model from field and subsurface data and developing an evolution of the petroleum system in time and space. So that, after the investigation of the influence of the bitumen as infilling fluid on the petrophysical properties of carbonate reservoir rocks and the evaluation of slip behaviour of carbonate bearing faults in presence of fluid, in this chapter, I present a 3D structural modelling and 2D basin modelling exercises. These regional-scale models are aimed to the understanding of the geological evolution of the petroleum system and the related fluids movements through the geological time.

I focus here on the Burano-Bolognano petroleum system in the Abruzzo Region, and it extends from the norther sector of the Majella mountain to the Cigno/Vallecupa oil fields. Even if these oil fields were intensively explored during the past century, some uncertainties in geographical distribution of the source rock and its maturity, timing migration and hydrocarbon-rock interactions, which have contributed to the actual known hydrocarbon distributions, are still opened questions. To support this understanding, a 3D structural model has been constructed for the main reservoir interval filled by hydrocarbon, using the Petrel software, in the whole investigated area. Geometry of the surfaces, derived from well correlations, depicts a coherent and continuous stratigraphic framework from the Majella mountain to the Cigno/Vallecupa oil fields. Then, I have performed simulation models of hydrocarbon generation and migration in time and space along two-dimensional geological sections, extracted by Petrel project, using the PetroMod software. Preliminary simulation results show that the Burano source rock is enough mature to generate oil and the best accurate representation of actual hydrocarbon occurrences is reached when the source rock is placed at north of the Majella mountain. Moreover, migration pathways evidence that in this petroleum system oil migration is firstly vertical, from the source rock into reservoir rock and then the system is laterally drained with a gradual oil biodegradation.

3.1 Basin and Petroleum System Modelling approach

Over the past decade, growing attention has been paid in the construction of accurate reservoir models by integrating the available geological, geophysical and petrophysical data to enhance the knowledge and production strategies of a petroleum system. To that purpose, in reservoir characterization study, it is a common practice to develop dynamic models that can describe the hydrocarbon flow behaviour within the reservoir.

Magoon and Dow (1994) defined a petroleum system as a geologic system that encompasses the hydrocarbon source rocks and all related oil and gas accumulations, also including all of the geologic elements and processes (i.e., deposition, erosion, hydrocarbon generation, and migration) that are essential for a hydrocarbon accumulation to exist. Therefore, basin modelling is a dynamic modelling that simulates these processes through geological time starting with the sedimentation of the oldest layers until to reach the present-day basin configuration and in the meantime the hydrocarbon generation from the source rock and accumulation in reservoir rocks (Hantschel and Kauerauf, 2009).

In this work, I have applied the basin and petroleum system modelling study to the petroleum system that extends from the norther sector of the Majella mountain to the Cigno/Vallecupa oil fields (Figure 3.1). The whole area has received great attention by oil companies in the past for its structural, stratigraphic, and geodynamic evolution, which has led to being an important target for hydrocarbon exploration during the past century. These discovered reservoirs are nowadays abandoned and for this reason the relative data is partially public (ViDEPI Project, 2012).

The northern sector of the Majella area was investigated by almost 160 wells drilled by ALBA company in the Lettomanoppello- Fonte di Papa-Fonticelle (LFF) and Sterparo-Cerratina (StC) areas at topographic elevation of 400-650 m and 700-1000 m, respectively (Lipparini et al., 2018). These wells reached a maximum depth of 200 m drilling the Oligo-Miocene carbonate deposits, as described in detail in the paragraph 1.2 of Chapter 1. These carbonate deposits, from all different facies of the Bolognano to Santo Spirito Fm, were reproduced in 3D modelling exercise with the exception of the thin marly interval, named “Cherty hemipelagic marly limestone”, well recognized in the Majella mountain, but not in the Cigno and Vallecupa oil fields, either because it is not distinguishable by composite well logs or because it is absent.

The Cigno/Vallecupa oil fields have also been intensively explored with almost 60 wells. These wells have reached an average depth of 700 m below surface, except for two deeper wells, Vallecupa 45 and Cigno 2 (location in Figure 3.1). These wells achieved the total depth of 2422 m and 2969 m, respectively, and they intersected the most key reservoir intervals up to older formations of the late Triassic and Jurassic age. Most of the other wells reached the principal reservoir interval at the bottom, named "Civita limestone", also known in literature as "Lepidocyclina Calcarenites" and some other wells drilled the Santo Spirito Fm (Figure 1.3B). In both study areas (Majella and Cigno/Vallecupa) the main reservoir interval is represented by the Bolognano Fm and in particular by the Lepidocyclina calcarenites. In the Majella outcrops are characterized by abundant heavy hydrocarbon within both primary and secondary porosity (Agosta et al., 2009; Scrocca et al., 2013; Lipparini et al., 2018). This heavy hydrocarbon shows a large density (1.14 g/cm^3), as investigated in Chapter 1. On the other hand, in the Cigno/Vallecupa oil fields several wells encountered the same reservoir interval at about 500-700 m of burial depth and the discovered oil is characterized by low density (average value of 0.850 g/cm^3). These hydrocarbon occurrences have been generally associated to a wider petroleum system that extends from the onshore Abruzzo and Molise regions to the offshore areas in central Adriatic Sea. Several authors pointed out that these hydrocarbon occurrences are generated from the late Triassic source rocks (Mattavelli & Novelli, 1990; Cazzini et al., 2015), but the actual geographical distribution of the sources is scarcely constrained, and several (sometimes conflicting) hypotheses have been proposed over time (e.g., Scrocca et al., 2013).

With the purpose to help constraining the location of the kitchen areas (i.e., area of the source rock that has reached appropriate conditions of pressure and temperature to generate hydrocarbons), the migration pathways and the properties of the generated hydrocarbons, I have applied the basin and petroleum system modelling approach starting from the known hydrocarbon occurrences in the whole study area.

In order to support this objective, a 3D structural model has been constructed using the Petrel software for the main reservoir interval filled by hydrocarbon in the whole investigated area. Geometry of the surfaces were constrained by the dense well dataset available for the northern sector of the Majella mountain and for the Cigno/Vallecupa oil fields (ALBA campaign and ViDEPI Project). Then, I have conducted an analysis on simulation of hydrocarbon generation and migration in time and space along two-dimensional geological sections.

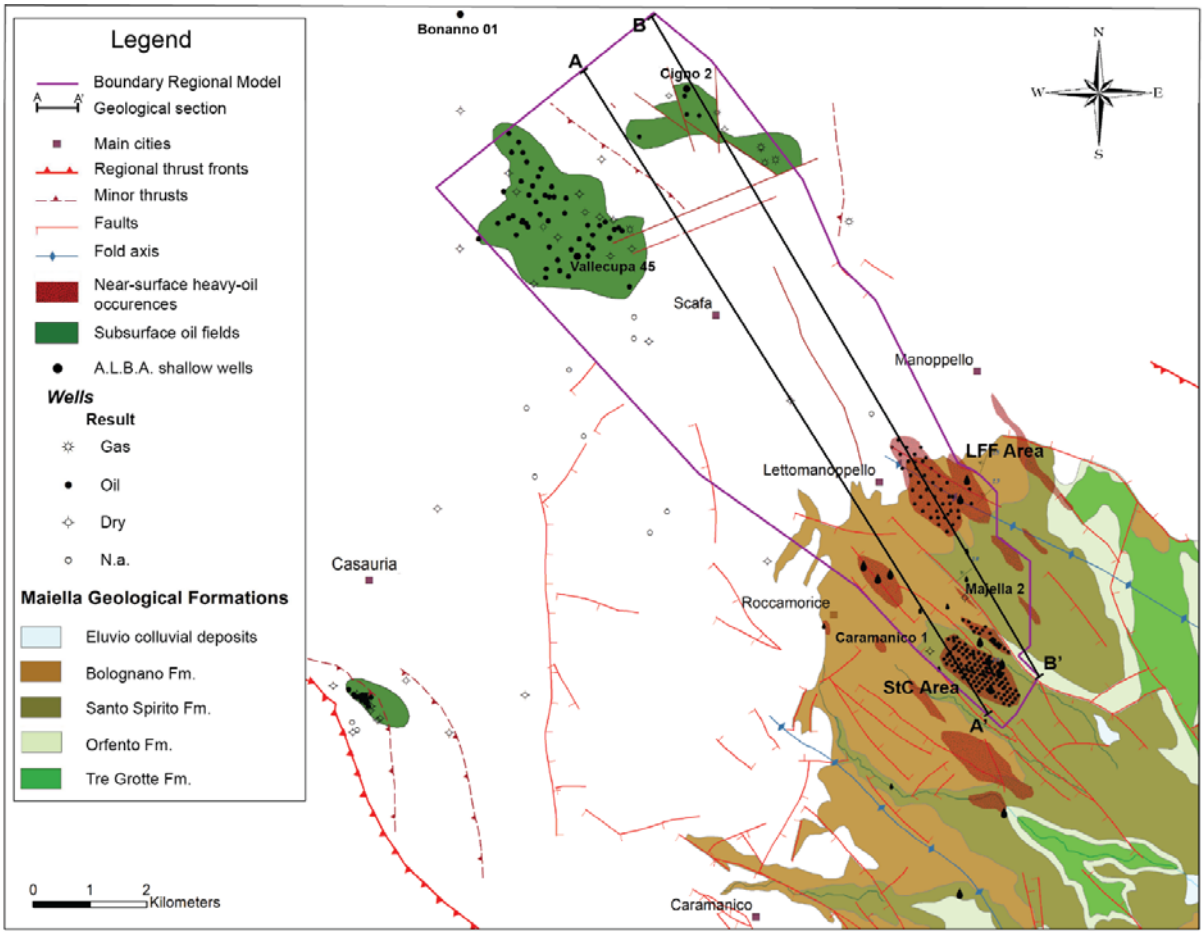

***Figure 3.1**: Base map of the study area at the front of the Apenninic chain (Abruzzo Region, Central Italy). The analyzed oil fields in this study are reported: the north-western flank of the Majella Mountain (LFF and StC Areas) and the Cigno/Vallecupa oil fields. Structural elements are shown, including major Apenninic-related thrusts and faults, in red. In dark violet the boundary of the 3D regional model is shown. 2D regional sections with NNW-SSE direction (A-A' and B-B') are drawn. Finally, exploration wells are shown following standard layout (modified after Lipparini et al., 2018).*

3.2 Input data and Methods

To evaluate the dynamic evolution of the petroleum system, I started from the reconstruction of the three-dimensional model of the Abruzzo onshore reservoir, from the northern sector of the Majella mountain to the Cigno and Vallecupa oil fields (Figure 3.1).
This work is subdivided in three tasks:

1. Stratigraphic input data selection and well correlations
2. Static model building
3. Fluid flow simulations

In the model construction phase, surface and subsurface of the investigated petroleum system were integrated with well data. The modelling was performed using the Petrel platform, mark of Schlumberger, which provided a flexible powerful tool to re-create a consistent 3D geological picture of the study area at different observation scales. This 3D volume reconstruction represents the static model, which is a base for the subsequent dynamic model. Accordingly, the geological surfaces, derived by the static model, have been used as input data within the PetroMod software, mark of Schlumberger, to provide a hydrocarbon fluid flow simulation.

3.2.1 Input Data

As a first step in building of the regional static model, I collected, re-classified and re-organised a large number of available data of wells (about 60 wells), which refer to the oil and gas exploration activities carried out across the 19th and early 20th century. All documentations were downloaded from ViDEPI dataset mainly related to the the Cigno and Vallecupa area (ViDEPI Project, 2012). For each well an accurate stratigraphic analysis has been conducted, defining well top depths of the key geological intervals that have been correlated with each other in the whole area. For the northern sector of the Majella mountain, I found at the Eni SpA Historical Archive an historical dense dataset of a drilling campaign executed over key bitumen and asphalt-rich area (Lipparini et al., 2018). The recovered reports, letters, and attachments of the geological and drilling campaign, conducted by a company called Azienda Lavorazione Bitumi Asfalti (ALBA) in years 1942-1943, had been the input data for the reconstruction of key intervals of the oil-bearing reservoirs and for the hydrocarbon distribution. This drilling campaign has produced about 180 shallow wells with depths from 80 to 200 m and regularly spaced over 100x100 and 200x200 m grids. Each well reported an accurate stratigraphy of the top and base reservoir interval, an average hydrocarbon percent saturation (by weight) and a

total-pay value. The results of the modelling exercise of the northern sector of the Majella mountain have been presented in Lipparini et al. (2018).

Therefore, key input data for the construction of the principal surfaces of the investigated petroleum system were:

- Key well tops which were interpreted and correlated with each other.
- Geological information over the investigated successions and lateral correlation, extracted from reports of the ancient exploration activities.

On the base of these information, I defined a reference stratigraphic succession to develop well-constrained stratigraphic levels, types, and characteristics, in terms of e.g., lithology, hydrocarbon accumulation, porosity. These datasets were loaded into the Petrel project as a key input in building the regional 3D model of the study area.

3.2.2 Static model

The building of the static model started with the reconstruction of the structural top of the hydrocarbon reservoir and with the interpretation of the fault network that dislocates the reservoir within the study area. For the Cigno oil field the reservoir top was developed by digitalizing the contour map of the Orte fm (the Bolognano member, see paragraph 1.2 for a detailed description), derived from the ViDEPI online dataset. To extend this surface to the adjacent Vallecupa oil field, I have correlated the top of this surface with the reservoir top depths, defined by stratigraphic analysis of all Vallecupa wells. In the northern sector of the Majella area the reservoir surface was created based on densely well dataset of ALBA campaign. The fault network, that affected the shallow stratigraphic succession, was directly mapped from the structure contour map for the Cigno/Vallecupa oil fields, from the available geological map (Foglio “Chieti 361”) and published papers (modified after Vezzani and Ghisettti, 1998 and Agosta et al., 2009) for the remaining study area. Then, these faults were reproduced within the 3D structural model.

The main steps to build a structural model are: 1) fault framework modelling, 2) pillar gridding and 3) making horizons (Figure 3.2a-c).

1) Firstly, faults, mapped in the study area, were imported in the structural framework module to build a reliable subsurface model. In this module I was able to define the cross-cutting relation between the mapped faults (Figure 3.2a).
2) Then, the defined faults were converted from the structural framework module to a key pillar-based fault model that was necessary to generate a grid. Following the pillar

gridding approach, I created three structural grids with high resolution (25x25 meters wide cells), each attached to the top, the mid and the base points of the fault key pillars (Figure 3.2b). The created structural grid is based on the fault model and thus, each new stratigraphic horizon, inserted in the model, follows the structural grid.

3) The subsequent step was to make horizons that are the principal stratigraphic surfaces, and this process defines the vertical stratigraphic intervals of model. The horizons are created inserting as input data the surfaces, previously created from the well tops, and each horizon defined by the top and bottom of a zone (Figure 3.2c). In this case, I have built five horizons that defined four zones (Figure 3.4).

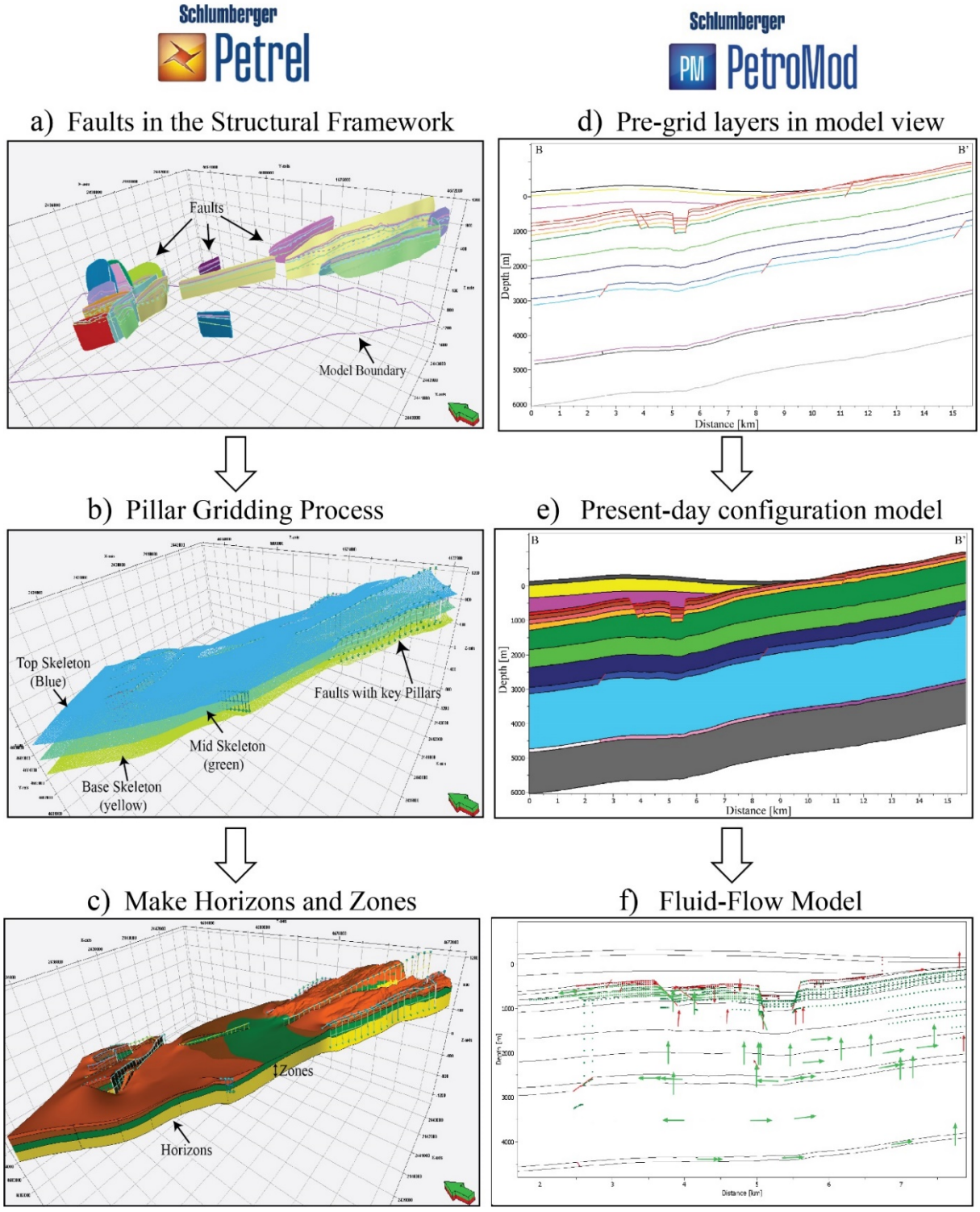

***Figure 3.2**: Schematic representation of the static and dynamic modelling workflows. For the construction of the static model using Petrel software (Schlumberger), the main steps are: a) Definition of faults and their relationships in structural framework modelling. b) Construction of a grid based on the defined faults in the Pillar gridding process. c) Inserting of stratigraphic horizons to increase the vertical resolution of the regional model. Simulation models were performed using PetroMod software (Schlumberger) along 2D section: d) Definition of geometry and stratigraphy in the pre-grid view. e) Gridding of the present-day basin configuration model. f) Simulation of generation-migration-accumulation of hydrocarbons within the study petroleum system.*

3.2.3 Dynamic model

I performed a hydrocarbon flow simulation using the software PetroMod 2D, following the methodological approach reported by Hantschel & Kauerauf (2009), and Allen & Allen (2013). For simulation models I defined 2D geological sections across the regional model developed using Petrel. Along these geological sections, 2D petroleum system model was built from geometry of the key stratigraphic intervals in the study area using 2D PetroBuilder in PetroMod software.

In Figure 3.2d-f I reported the basic model building workflow, which includes:

- Loading of digitalized horizons and faults (Pre-grid horizons and faults);
- Gridding process;
- Age and facies definition assignment;
- Fault properties assignment;
- Assign boundary conditions such as, paleo water depth (PWD), sediment water interface temperature (SWIT) and heat flow (HF);
- Setting the simulator options and parameters, such as the resolution of each time steps, migration method, petroleum kinetics, and the output data.

Firstly, the interpreted stratigraphy along the geological sections from Petrel software were directly imported in PetroMod software as the geometric input for 2D basin modelling. I defined the boundary of the model, and I checked the intersection between the pre-grid horizons and faults, verifying also that pre-grid horizons reached the boundary of the model using PetroMod software manually. Moreover, in 2D models I added deeper horizons that those in the Petrel model to reconstruct all elements of petroleum system, from seal to source rocks. To do this, I selected the deepest wells (Caramanico 1 and Cigno 2) drilled near the geological sections in the study area and I imported the well top depths of the main stratigraphic intervals of the area (see Table 3.1).

Subsequently, the fault model was created, and the gridding process is started, ensuring that each node of a horizon or fault lies on a grid point (PetroBuilder2D User Guide, version 2020). After the complete digitization, fault model creation and gridding of the faults and horizons process, the section was ready for model development.

In the next step, age and facies properties were assigned to each layer of the model (Table 3.1). In PetroMod each facies is characterized by the defined petrophysical properties, and thus with the definition of facies I assigned the petrophysical properties for layers, which is essential for a realistic fluid-flow simulation.

Moreover, the definition of the source rock properties, such as: thickness, lithology, Total Organic Content (TOC) and Hydrogen Index (HI) values, is necessary for the generation of hydrocarbons during the simulation.

Horizon Name	Age [Ma]	Layer Name	Lithology PetroMod	PSE
Recent Deposits	0	Recent Deposits	Conglomerate (typical)	Overburden
Pliocene Deposits	2.5	Pliocene	Siltstone	Overburden
Gessoso-solfifera Fm.	5.33	Gessoso-solfifera	Anhydrite	Seal
Lithotamnium Lmst	6.9	Lithotamnium Lmst	Limestone (Chalk, 40% calcite)	Reservoir
Hemipelagic Marls	11.6	Hemipelagic Marls	Marls	Seal
Lepidocyclina calcarenites	17.6	Lepidocyclina calcarenites	Limestone (ooid, grainstone)	Reservoir
Santo Spirito Fm.	31.2	Santo Spirito Fm.	Limestone (shaly)	Reservoir
Orfento Fm.+ Scaglia	66	Upper Cretaceous	Limestone (shaly)	Overburden
Marna a fucoidi	100.5	Lower Cretaceous	Limestone (shaly)	Overburden
Maolica + Aptici	120	Lower Cretaceous-Upper Jurassic	Limestone (micrite)	Overburden
Rosso Ammonitico	174	Middle/Lower Jurassic	Limestone (micrite)	Overburden
Corniola + Massiccio	182.7	Lower Jurassic	Limestone (micrite)	Overburden
Burano Fm.	201.3	Upper Triassic	Dolomite (Organic rich)	Source

Table 3.1*: Input parameters necessary for building of 2D PetroMod simulation model are reported: the principal interval obtained from the Petrel model and the deeper wells, their ages, name of the layer within the PetroMod model and the corresponding petroleum system element (PSE).*

Before running the simulation, the last step was the setting of boundary conditions, which define the basic energetic conditions for temperature and burial history of the source rock and, consequently, for the maturation of organic matter through time (PetroBuilder2D User Guide, version 2020). Three main boundary conditions were designated (Figure SC.2 in Appendix C): paleo water depth (PWD), sediment water interface temperature (SWIT) and heat flow (HF).

The PWD of the basin model were assigned for each stratigraphic layer based on published information (e.g., Crescenti et al., 1969; Vecsei et al., 1998; Mutti and Bernoulli, 2003; Rusciadelli, 2005; ViDEPI, 2012; Carminati et al., 2013).

Since the temperature at surface water interface and the paleo water depth are strongly correlated, the SWIT trend was calculated starting from the PWD data using the semiautomatic tool in PetroMod. This tool extracts a standard temperature at sea level over geological time

setting the geographic location and the latitude, that are North Mediterranean and 42°, respectively, for this study case (Figure SC.3 in Appendix C).

The last parameter to be defined for a basin modelling work is the HF, which represents the thermal energy flux at the base of the model, measured in mW/m^2. This parameter was set to 45 mW/m^2 as the present-day heat flow based on matching the paleo-thermal reconstruction proposed by Ronchi et al. (2010) with the present-day thermal data of wells drilled in the study area (ViDEPI Project, 2012; GeoThopica Project, in progress) and also considering the present-day heat flow map proposed by Della Vedova, (2001).

After the definition of all properties, the model was opened in 2D simulator window to run simulations. Hydrocarbon migration was modelled using the combined Darcy flow and invasion percolation algorithm, that results to be faster and with the same resolution than the other migration methods. This is because Darcy flow model is used in low permeability cells and invasion percolation in high permeability cells.

3.2.4 Characterization of the petroleum system elements

In the previous paragraph, it was outlined the importance of facies assignment at stratigraphic intervals that consists in defining the appropriate petrophysical properties, such as porosity and permeability that influence the migration of fluid. Therefore, I used the default properties of the PetroMod catalogue for the chosen lithologies except for the most important reservoir interval, Lepidocyclina Calcarenites. This interval was well characterized by laboratory measurements of porosity and velocity at ambient and increasing confining pressure (Chapter 1), so that I decided to assign user-defined porosity property as a function of depth with the following methodology.

In the Chapter 1, I shown the linear relation between porosity-velocity established for the clean samples (Equation 1.7, Paragraph 1.4.3 Chapter 1) and therefore from this equation, the porosity is equal to:

$$\phi = \frac{5.6406 - V_p}{0.0817} \quad (3.1)$$

To calculate the porosity values at different depths, I used the relationship between Vp and confining pressure derived from laboratory measurements of the clean samples. Therefore, I calculated the average values of Vp at defined confining pressure (i.e., 0, 25, 50, 70 and 100 MPa) and assuming a constant gradient pressure of 25 MPa/km, so that the selected pressures

correspond to the depths of 0, 1000, 2000, 2800 and 4000 m, respectively. Subsequently, replacing the Vp value at each confining pressure (or depth), I calculated the porosity at different depths. With these porosity values, I defined the exponential relationship between porosity and depth, in agreement with the Athy's law (Athy, 1930), as reported in Figure 3.3.

By the following relationship:

$$z = -19082\ ln(\phi) + 52928 \quad (3.2)$$

where depth is in meters and porosity in percent, it is possible to calculate porosity at different depths by using:

$$\phi = 15.96\ e^{-\,5.25\,10^{-5}\,z} \quad (3.3)$$

Therefore, in PetroMod Lithology editor, I assigned porosity property of the Lepidocyclina reservoir interval calculated for the interested depths of the models with the equation 3.3.

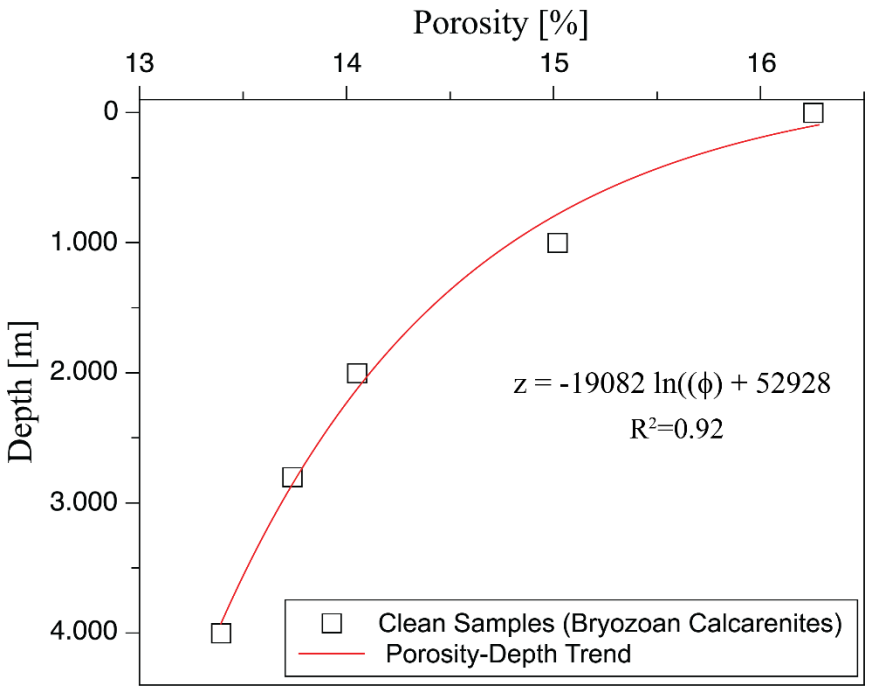

Figure 3.3: *Porosity- Depth relationship for the clean samples belonging to the Lepidocyclina Calcarenite derived by the laboratory measurements of porosity and Vp at increasing confining pressure.*

According to Cazzini et al. (2015), the Triassic evaporites have been supposed to be the source rock for the hydrocarbon accumulation in the study area. The source rock depositional

model, here adopted, has been firstly presented by Zappaterra (1990, 1994). The author has supported the idea that the Late Triassic evaporitic rocks were deposed within anoxic intra-platform lagoons and troughs, characterized by a shallow depth of water (i.e., 10-50 m) and then they were prograded and sealed by platform carbonates. Therefore, I chose to add small faults at the border of the source rock to reproduce a similar depositional environment and also compartmentalize the source interval.

With the purpose to better understand the fluid-rock interactions and the known hydrocarbon accumulations in the Majella and in the Cigno/Vallecupa oil fields, I tested different possible locations where the source rock interval has reached the best conditions to generate hydrocarbons. In particular, I simulated an active source rock: under Majella Mountain (named SR_Majella), under Cigno/Vallecupa oil fields (named SR_Cigno) and further north (named SR_NorthCigno).

The principal geomechanical characteristics of the Triassic source rock have been based on literature works (Mattavelli & Novelli, 1990; Zappaterra 1994; Katz, 2000; Cazzini et al., 2015). The Burano source rock is characterized by:

- Thickness of 100 m at the top of the Burano Fm.
- Total Organic Carbon (TOC = 4%),
- hydrogen index (HI=500 mg HC/g TOC)
- type of kerogen (type II)

Moreover, for the source rock I assumed a kinetic model from the PetroMod software catalog (Pepper & Corvi, 1995 T-II S(A)), on the base of the source rock paleo-environment, organic matter and generated oil.

3.3 Results

3.3.1 Regional model

By integrating the results of the stratigraphic analysis, conducted along composite log of both Majella and Cigno/Vallecupa wells and correlated all available well top depths, I reconstructed accurate 3D stratigraphic surfaces at regional scale. The developed regional model resulted to have total axial length of about 15 km and width about 6 km, located between the northern sector of the Majella mountain and further north of the Cigno/Vallecupa oil fields. In Figure 3.4, I reported a detailed representation of the developed model extracted by the 3D model. The 2D sections cross the key discovered oil fields in the whole study area (see base map on the bottom right). From a stratigraphic standpoint, the main reservoir interval is recognized to be homogeneous in thickness and laterally continuous from the Majella mountain and to the Cigno/Vallecupa oil fields, as well as for the underlying layer of Santo Spirito Fm. The shallower stratigraphic levels (Lithotamnium lmst and Hemipelagic marls) are not continuous because of erosive events linked to the late involvement of the Majella sector into the Apennines chain deformation front (Ghisetti and Vezzani, 2002).

With the purpose to perform an analysis of the fluid-flow behaviour within the investigated petroleum system, I extracted the two 2D sections, directly from Petrel regional project:

1) An NNW-SSE striking section from the Sterparo-Cerratina area (north sector of the Majella Mountain) to the Cigno and Vallecupa oil fields and it is closed to Caramanico 1 well.
2) An NNW-SSE striking section, parallel and east of the section 1, extending, like previous one, from the northern sector of the Majella Mountain, across the Lettomanoppello-Fonte di Papa- Fonticelli area, to the Cigno and Vallecupa oil fields, near the Cigno 2 well.

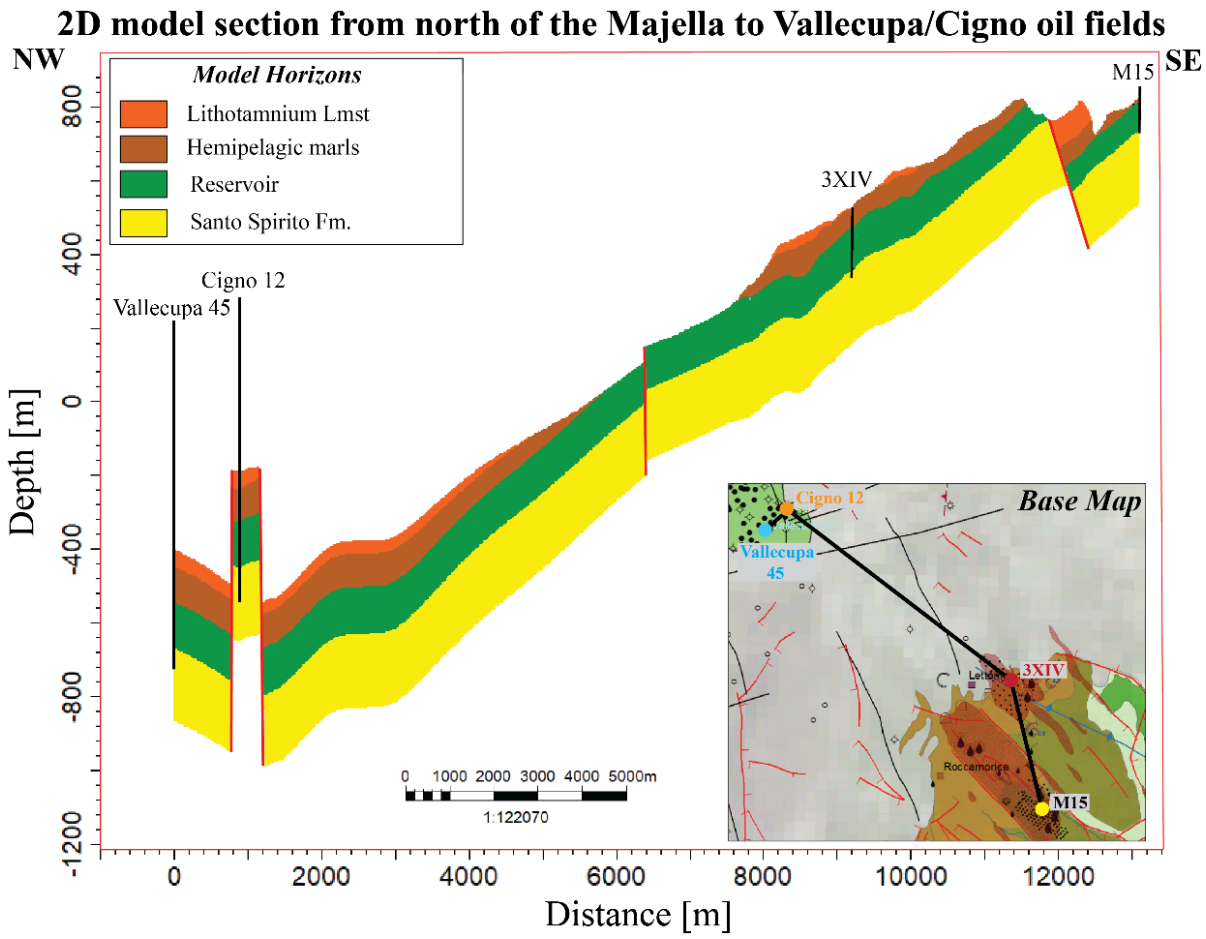

***Figure 3.4**: A detailed representation of 2D section that across the regional model from the northern sector of the Majella Mountain to the Cigno/Vallecupa oil fields (see base map at the bottom right for section location). The section derived by the building of the stratigraphic zones in Petrel project by means of the correlations between key wells in the Cigno /Vallecupa area (Vallecupa 45, Cigno 12) and in the Majella area (3XIV, M15).*

The orientation of both sections is chosen for two reasons. The first one is that most of faults are mainly northwest-southeast trending normal faults (Vezzani and Ghisetti, 1998; Agosta et al., 2009), and they most likely guided the migration of hydrocarbon from the Cigno/Vallecupa oil fields to Majella area. The second reason is related to the location of the deeper wells drilled in the study area (Caraminico 1 and Cigno 2) through which I calibrated the stratigraphic framework below the data of the model.

These sections have been imported in PetroMod and the present-day configuration is reported in Figure 3.4, showing all key elements of the investigated petroleum system, from source to seal rocks.

The stratigraphic intervals, from top Lithotamnium to top Upper Cretaceous, were derived from the 3D structural model and they result to be well constrained by the wells correlation dataset. Whereas the stratigraphic framework below the Santo Spirito Fm the most key intervals, from the Cretaceous to the Late Triassic, were reconstructed based on the deeper wells drilled closed to the geological sections, as Caramanico 1 and Cigno 2 wells.

Since these two sections intersect the same main domains, the same stratigraphic intervals and they have the same directions, I discuss the observations made along sections together from north-west to south-east direction.

Figure 3.5 highlights that the horst and graben structure of the Cigno and Vallecupa oil fields are overlaid by the Plio-Pleistocene deposits and the Messinian evaporites formations that represent the seal for the below hydrocarbon accumulations. Moving toward to south, the thickness of these deposits decreases and a gradual transition from basin marly facies to carbonate ramp facies is observed. In fact, after about 7 km towards the south respect the Cigno/Vallecupa oil fields, the same buried formations crop out in the northern sector of the Majella mountain. Here, at around 1000 m above the sea level, the first stratigraphic interval found at surface by ALBA drilling campaign was the Lithotamnium limestone, that represents the upper member of the Bolognano Fm (Brandano et al., 2016).

From a geological point view, these sections allow to observe the transition from the Apulia carbonate margin (at SSE) to the basin domain (at NNW) with a relatively undeformed and continuous stratigraphic framework from the northern sector of the Majella mountain to the Cigno/Vallecupa oil fields, as also suggest by several previous works over the geometrical and stratigraphical relationships conducted in the study area (Crescenti et al., 1969; Vecsei et al., 1998; Rusciadelli, 2005; Lipparini et al., 2018; Trippetta et al., 2020).

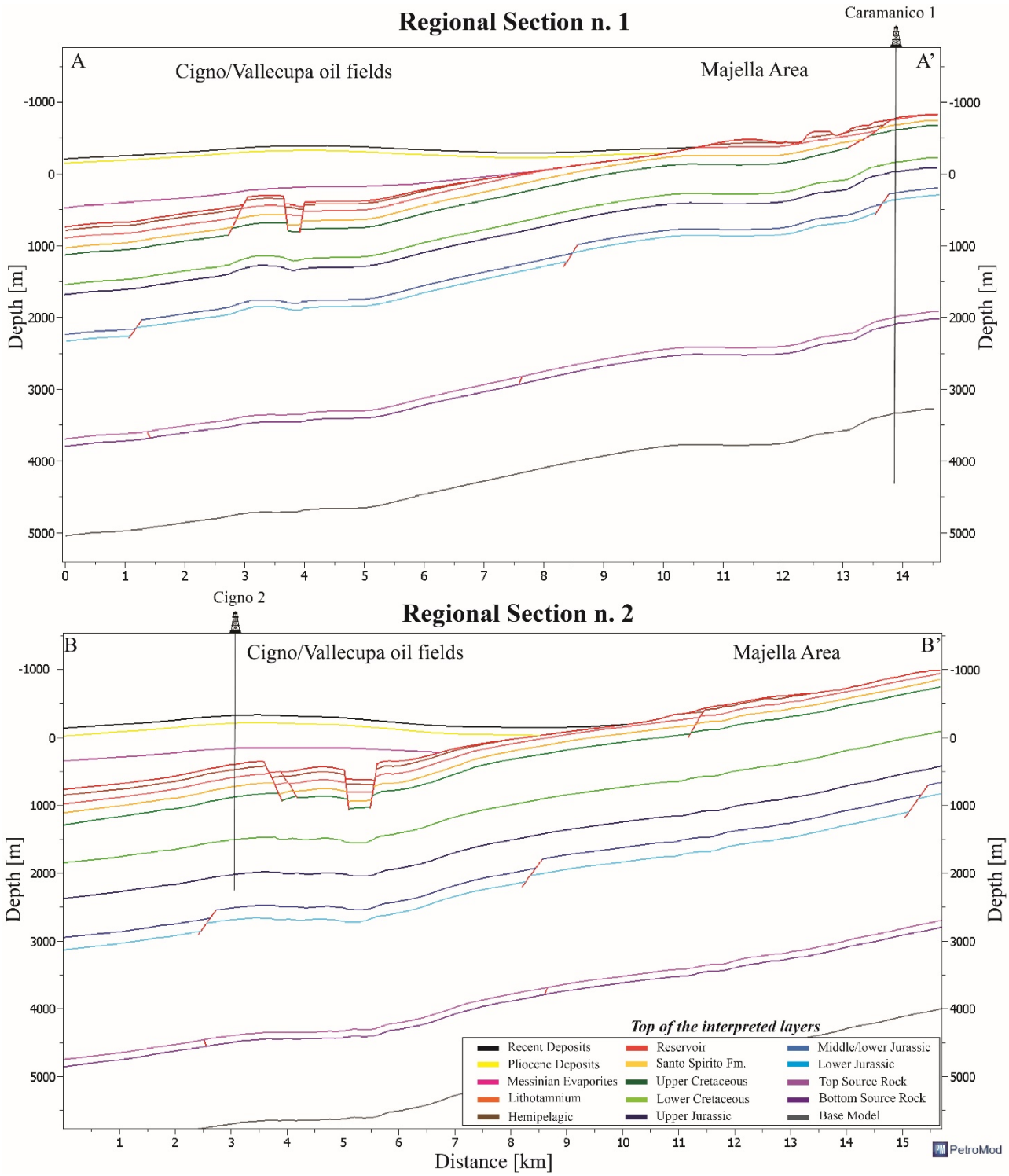

***Figure 3.5**: Pre-grid model view of the digitized horizons and faults across the two 2D sections (see base map in figure 3.1 for section location). Horizons and faults were derived from the regional model and from literature review. Moreover, the tops of horizons were calibrated with the deeper wells drilled near the regional sections (Caramanico 1 for regional section n.1 and Cigno 2 for regional section n.2).*

3.3.2 Simulation modelling results

The simulated models of the investigated petroleum system are displayed in 2D viewer module of the PetroMod software.

Since it is well known that generation, migration, and accumulation processes within a petroleum system occur after that the source rock is mature enough to produce oil, I started presenting the preliminary results about the source rock maturity and then about the hydrocarbon migration pathways and accumulations.

The simulation models in all three different locations of the active source rock show that the Triassic source rock has reached the maturity to generate hydrocarbons and it is still in maturated stage at present-day basin configuration (Figure 3.6a-b). The maturity of source rock is defined with the vitrinite reflectance and temperature evolution, as output data of the model. The temperature history shows that the Burano source rock has achieved in all three locations a maximum temperature comprising between 98.5° and 114 °C in the regional section n.1 and n.2, respectively. The vitrinite reflectance (Ro) values, modelled with the Sweeney and Burnham (1990) easy% Ro model, is reported in Figure 3.6a-b for both regional sections. Assuming the onset of oil window maturity at 0.55% (Allen & Allen, 2013), the simulation models show that in both regional sections and in all the tested locations, the Burano source rock can reach maturity. It is worth noting that the maturity of the source rock is not the same for the different tested locations. When the possible source rock is placed below the Majella mountain, lower values of Ro are observed (in the interval of 0.75-0.70%), while the Ro values increase up to almost 0.90% if the active source rock is located further north, near the Cigno/Vallecupa oil fields, especially for the regional section n. 2. This Ro evolution in space is also consistent with the maximum temperature data, illustrated above.

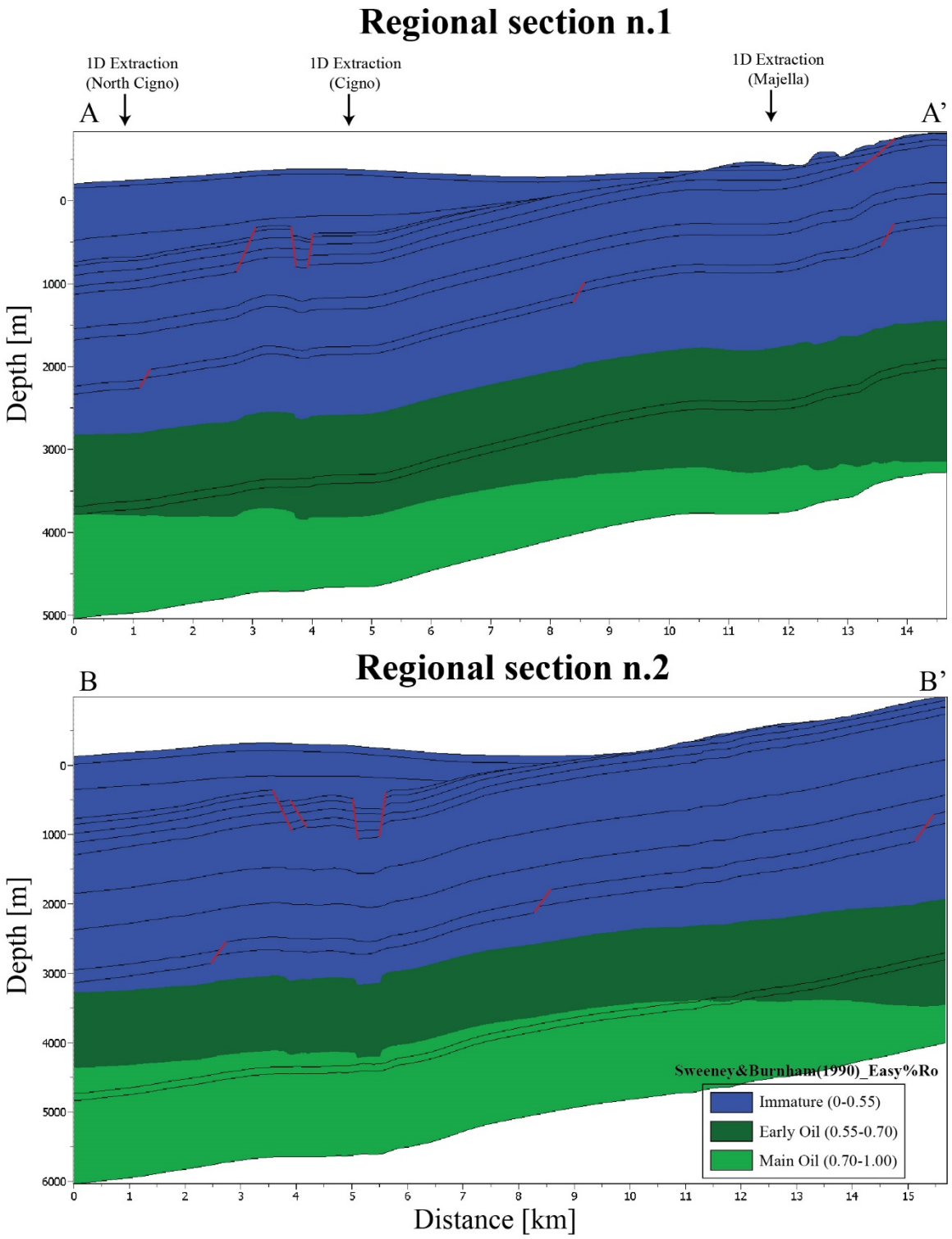

***Figure 3.6**: Present-day basin configuration modelled with the Sweeney and Burnham (1990) easy% Ro model (a) for the regional section n. 1 and (b) for the regional section n. 2. At the top of the regional section 1, I also reported points at which in each section I have extracted the TR properties for the three different active source rocks.*

Another important parameter to be considered in the timing analysis of a petroleum system is the critical moment, that is the time of highest probability of the entrapment and preservation of hydrocarbons in a petroleum system (Schlumberger, Oilfield Glossary). Since the critical moment occurs when the transformation ratio (TR) is greater than around 50%, I also analyzed TR parameter in the source rock interval. TR is related to the production index and it is defined as the ratio of the petroleum (oil and gas) actually formed by the kerogen to the total amount of petroleum that the kerogen is capable of generating (Tissot and Welte, 1984). Values range from 0 to 1.0 and high TR indicate that the source rock has already generated most of its oil and gas, whereas low TR indicate immaturity.

The results about TR analysis are shown in Figure 3.7 for both regional sections and at three different tested positions of the source rock as a burial-depth plot, derived by 1D extraction along a pseudo-well at the middle of each active source (location is reported in Figure 3.6 for each 1D extraction). The plots illustrate the deposition and burial of each layer over time (diagonal lines upper left to bottom right) and in the only source rock interval the TR values are illustrated.

For the regional section 1 (Figures 3.7a-b-c), at the different positions of the possible source rock the average TR values range between 45 and 30% and they are influenced by the position of the source rock. In agreement with the other parameters (temperature and Ro), previously analyzed, when the source rock is located under the Majella mountain lower TR values are recorded (TR around 30%; Figure 3.7 a). An increased TR value of about 33% is observed for the source rock under and further north the Cigno/Vallecupa oil fields (Figures 3.7 b-c). In section 2, the TR values are generally in the interval of 68-55.3% because of higher temperature were reached. The increase of TR can be observed when the active source rock is progressively moved from the SR_Majella, through SR_Cigno to SR_NorthCigno (Figures 3.7 d-e-f).

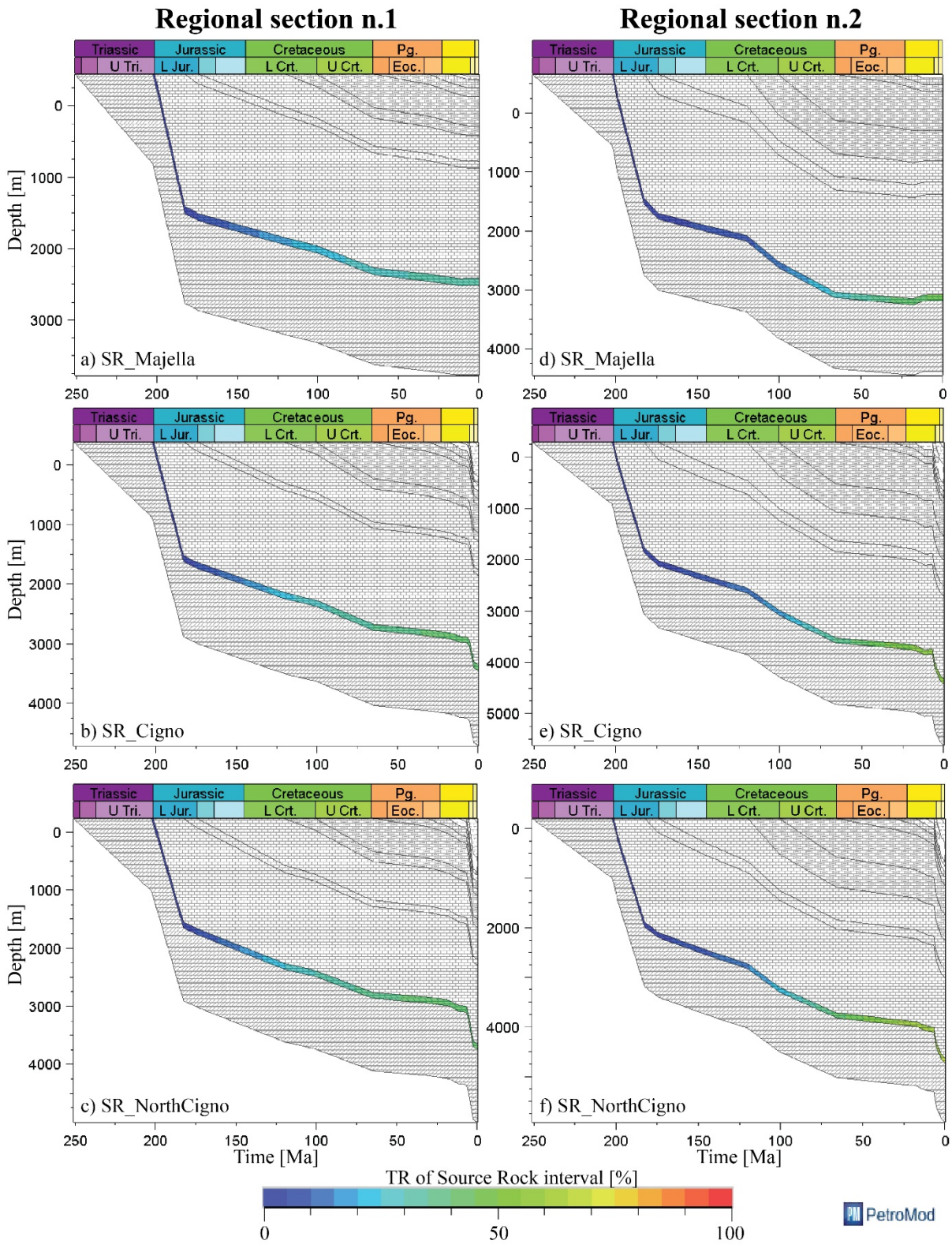

Figure 3.7: *Transformation ratio (TR) as a function of time in the source rock interval at different its investigated locations (under Majella, under Cigno/Vallecupa and futher north of the Cigno/Vallecupa oil field) for the regional section n.1 (a-c) and the regional section n.2 (d-f).*

According to these maturity data, all the models (2 section and the three active source rock locations) show that the Triassic source rock has generated a significant hydrocarbon quantity, accumulated mainly in the known reservoirs of the Cigno/Vallecupa and in the subsurface of the Majella mountain (Figures 3.8-3.9). The oil expulsion started in both sections during the Upper Cretaceous (~99.6 Ma) and the migration from the source rock towards the overlying reservoir rocks is mainly vertical (see green arrows in the lower part of each model). This hydrocarbon migration from the source is mostly controlled by the applied migration method, which considers the pressure gradient-driven (Darcy Flow indicates by arrows in Figures 3.8-3.9) and the buoyancy-driven flow (Percolation Flow indicates by dots in Figures 3.8-3.9).

In the simulation model all faults that dislocate the shallower carbonate sediments of the Bolognano and Santo Spirito Fm., have been considered as possible conduits to fluid flow.
Starting from Early Pliocene, when the Bolognano Fm is overlaid by the regional seal of the Messinian evaporites and marls, hydrocarbon migrations firstly occurred along faults. Then, hydrocarbons laterally migrate through the Miocene reservoir rocks (Bolognano Fm) in agreement with outcrop observations (e.g., Vezzani and Ghisetti, 1998; Agosta et al., 2009).
In both regional sections, some observations concerning the hydrocarbon accumulations can be done:

1) when the source rock is located under the Majella mountain hydrocarbon accumulations are lower and most of the fluid flow is limited towards traps vertically above the source rock. Consequently, at the present-day configuration (Figures 3.8a and 3.9a), hydrocarbons are entrapped in the Cretaceous formations and in the Miocene reservoir rocks of the Majella subsurface. However, hydrocarbon accumulations in the Cigno/Vallecupa oil fields are very limited, being close to zero. Moreover, little accumulations of gas are presented in the shallower layers (Hemipelagic Marls and Lithotamnium Lmst).

2) when the source rock is located under the Cigno/Vallecupa oil fields an important quantity of hydrocarbon is accumulated into the main reservoir interval (Bolognano Fm) in both areas of (Cigno/Vallecupa and Majella mountain). Once the hydrocarbons reached the reservoir by vertical migration, a lateral migration through conduit faults is established. From simulation models, it can be observed that not only an important quantity of hydrocarbon is accumulated, but also a considerable quantity of gas is presented above the main reservoir interval. At the present day-configuration (Figures 3.8b and 3.9b), the Cigno/Vallecupa structures entrapped gas that cannot migrate

upwards because the Messinian evaporites and marls act as a seal. This seal gradually decreases in thickness toward the Majella and thus, in the central part of the section, some gas leakages are observed, caused by the presence of the Plio-Pleistocene deposits characterized by sandstone-clay intercalations, resulting more permeable respect to the Messinian evaporites and marls.

3) when the source rock is located further to the north with respect to the Cigno/Vallecupa oil fields, hydrocarbon and gas accumulations seem to be analogous to the previous model. Here, the hydrocarbons migrate vertically upward from the source rock to the traps below Cigno/Vallecupa structure. Successively, a lateral migration is established towards the Majella area (Figures 3.8c and 3.9c). In both section the hydrocarbon migration is mainly driven by buoyancy. At the present-day configuration, a discrete hydrocarbon and gas accumulations are found in the Majella subsurface and a little wider hydrocarbon and gas accumulations are recorded in the Cigno/Vallecupa oil fields.

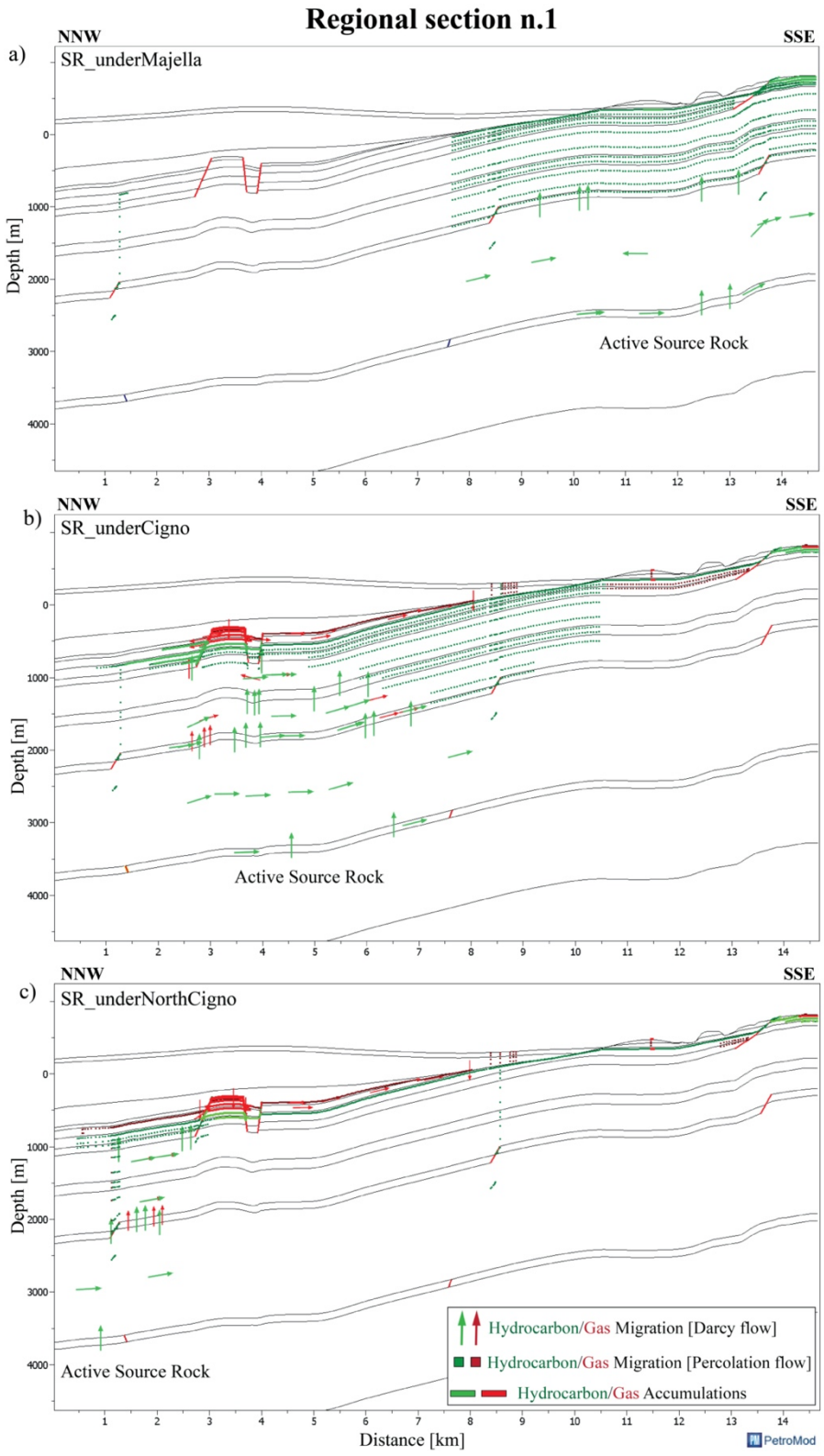

Figure 3.8: *Present-day hydrocarbon accumulations and oil upward (see green arrows) from the source rock into the reservoir and the lateral migration, especially within the source rocks for the regional section n.1. Moreover, hydrocarbons were migrated through percolation and these pathways are reported (green dots). I tested different source rock location: a) under Majella, b) under Cigno/Vallecupa oil fields and c) further north of the Cigno/Vallecupa oil fields.*

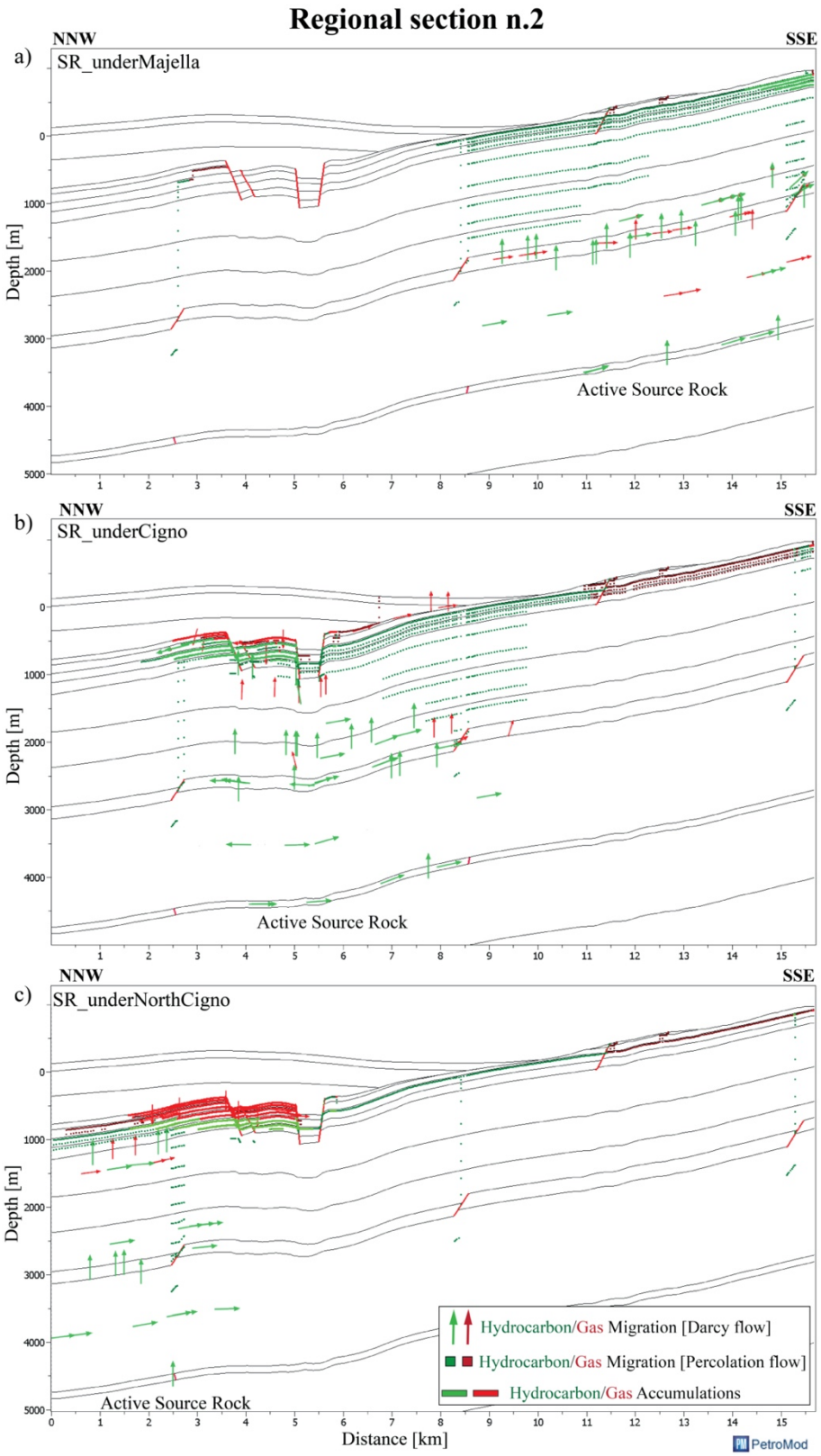

Figure 3.9: *Present-day hydrocarbon accumulations and oil upward (see blue arrows) from the source rock into the reservoir and the lateral migration, especially within the source rocks for the regional section n.2. Moreover, hydrocarbons were migrated through percolation and these pathways are reported (green dots). I tested different source rock location: a) under Majella, b) under Cigno/Vallecupa oil fields and c) further north of the Cigno/Vallecupa oil fields.*

3.4 Data interpretation and Discussion

I discuss here some of key observations that can be drawn from the analysis both of static and dynamic models and I present a hypothetical model of hydrocarbon migration from source to reservoir of the study area.

In the 3D modelling exercise, I was able to reconstruct the stratigraphic framework of the Oligo-Miocene carbonate formations at regional scale, from the northern sector of the Majella mountain to the Cigno/Vallecupa oil fields (Figure 3.4). The coherent and laterally continuous stratigraphy of the main reservoir interval was established in relation to the dense well dataset (ViDEPI Project, 2012; ALBA, 1943), available for the study area and also it is in good agreement with outcrop-based published works (Mutti and Bernoulli, 2003; Brandano et al., 2016). Going at more regional scale, data of exploration wells drilled in the Central Adriatic offshore confirm that the Oligo-Miocene carbonate interval is widespread and laterally continuous, as demonstrated for example, by the oil accumulations within the Bolognano reservoir found at Ombrina Mare and Katia oil fields (Lipparini et al., 2018), all belonging to the same regional petroleum system (Mattavelli and Novelli, 1990; Bertello et al., 2010; Cazzini et al., 2015).

The 2D basin modelling work has highlighted:

1) the Triassic Burano Fm as the best possible source rock, which has generated the known hydrocarbon accumulations discovered in the Cigno/Vallecupa oil fields and in the Majella mountain.
2) the Bolognano Fm, as the best reservoir interval, in agreement with the laboratory porosity data, discussed in the Chapter 1.

Therefore, following the standard criteria for petroleum system name (source rock name-reservoir rock name), I defined the petroleum system, investigated in this research, as the Burano-Bolognano petroleum system.

In Figure 3.10, I reported the most important time steps to show the preliminary results obtained by the modelling. To do this, I selected the section n.2 as the base of the conceptual model at three key interval times. The same interpretations can be extended to the first regional section because in both sections the same hydrocarbon accumulations at present-day configuration is observed.

By analysing the TR (Transformation Ratio) values, the Upper Cretaceous can be considered as time at which the active source rock has started the oil expulsion (Figure 3.10 A). This phase is known as the primary migration during which oils migrate upward within the same source rock. All simulation models have shown that the Burano source rock has reached a discrete maturity along the whole section length, being entirely above the oil window (dashed line in Figure 3.10 A), that is around 3000 m in the first investigated time step. This means that all lithologies above this limit are enough mature to generate oil if favourable conditions, such as the deposition of organic matter, occurred. Considering the model proposed by Zappaterra et al. (1994) several isolated basins within Triassic/Jurassic sediments can reach sufficient TOC to be potential source rocks, so that some other active source rock portions cannot be excluded along the sections. For instance, the Lower Jurassic source rock can be productive due to the intercalations of the dolomite rock that is rich in organic matter, as demonstrated by Grifone 01 well, drilled in the Puglia Region offshore near to the margin of the Apulia carbonate platform (Campana et al., 2017). If Jurassic active source rocks would be present in the studied sections, the oil expulsion would be simply delayed due to the shallower position with respect to the Triassic formations and the consequent delay in reaching the oil-window. Conversely, models seem to exclude any possible Cretaceous source rocks because the Cretaceous sediments always remain above the oil window (Figure 3.6).

The oil migration is influenced by porosity and permeability of the rock and also by the presence of fractures. Consequently, the hypothesized vertical migration is supported by the direction of the minimum principal stress, σ_3, oriented in E-W direction as shown by the present-day stress maps (Montone and Mariucci, 2016).

As shown in Figure 3.10B, the first oil and gas accumulations are recorded under the Cigno/Vallecupa structure when the important seal formations are deposited, such as Hemipelagic marls (Late Burdigaglian to Serravallian) and the Messinian evaporites. During the Early Pliocene, secondary migration brings hydrocarbon within the Miocene reservoir of the Cigno/Vallecupa area along faults that act as conduits to fluid flow. Then, hydrocarbon migration continues laterally, as a tertiary migration, through the Miocene reservoir rocks (Bolognano Fm) reaching the reservoir in the Majella area (Figure 3.10 C), in agreement with outcrop observations (e.g., Vezzani and Ghisetti, 1998; Agosta et al., 2009). In this area, several near-surface and outcropping reservoirs are found locally filled with a heavy-hydrocarbon (bitumen) due to the migration within shallower reservoir (Demaison and Huizinga, 1994; Jones et al., 2008), responsible for a gradual biodegradation of hydrocarbons.

According to the biodegradation hypothesis, models show a decrease of oil density from the Cigno/Vallecupa oil fields (~830 kg/m^3 and API <39°) towards Majella mountain (~900 kg/m^3 and API<24°). This progressive decrease of API gravity toward the south and the consequent increase toward the north seems to be confirmed by the Bonanno 1 well, drilled north to the Cigno/Vallecupa oil fields. This well intersected the same reservoir, Bolognano Fm, and the discovered oil show 36.4° API (American Petroleum Institute gravity) that are larger with respect to the API degrees recorded in the Cigno/Vallecupa oil fields (~25° API) and very much larger with respect to those recorded in the Majella mountain (< 1° API, as observed in Chapter 1).

Finally, fluid-flow model suggests that the most likely position of the active source rock is close to the Cugno/Vallecupa oil fields. This position explains the presence of oil reserves in both reservoirs (Majella and Cigno/Vallecupa oil fields), in agreement with a hypothesized allochthonous origin of the Majella bituminous field (Scrocca et al., 2013; Trippetta et al., 2020). Furthermore, models indicate that a possible source rock exactly below the Majella mountain is not feasible as demonstrated by the Caramanico 1 well (see location in Figure 3.1). This well reached the Triassic Evaporites from ~2850 m down to the total depth of the well where only bitumen traces are founded. However, as previously noted, since the whole Triassic/Jurassic intervals reached the oil window the presence of other Triassic/Jurassic small portions of active source rocks between Cigno/Vallecupa and Majella areas cannot be completely excluded.

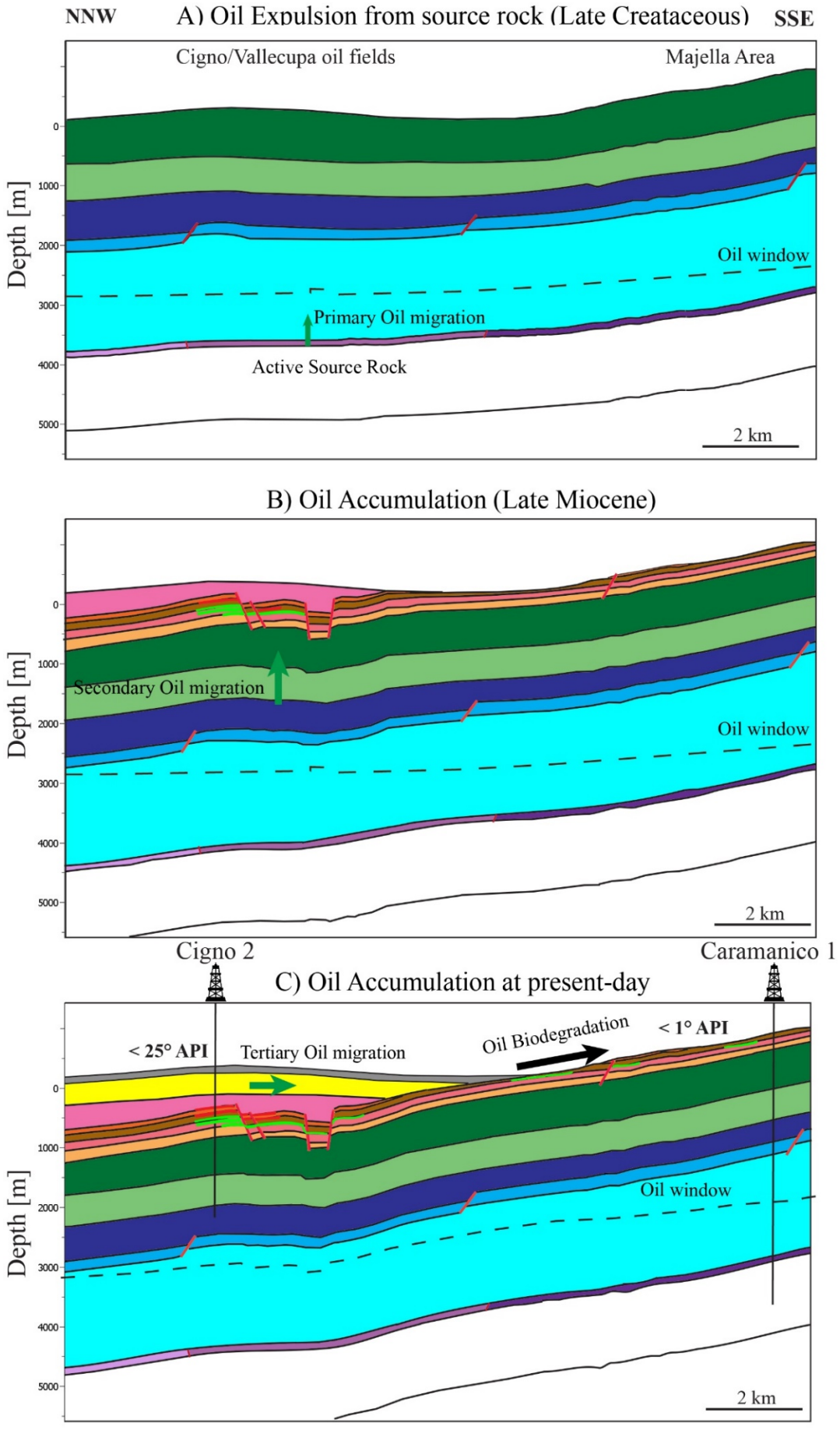
NNW
A) Oil Expulsion from source rock (Late Creataceous)
SSE
Cigno/Vallecupa oil fields
Majella Area
Depth [m]
0
1000
2000
3000
4000
5000
Oil window
Primary Oil migration
Active Source Rock
2 km
B) Oil Accumulation (Late Miocene)
Secondary Oil migration
Oil window
2 km
Cigno 2
Caramanico 1
C) Oil Accumulation at present-day
< 25° API
Tertiary Oil migration
Oil Biodegradation
< 1° API
Oil window
2 km

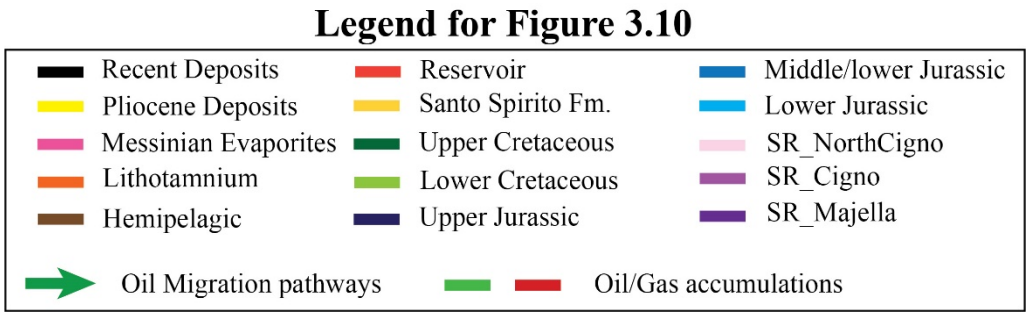

***Figure 3.10**: Conceptual model at distinct time steps of the Burano-Bolognano petroleum system, analyzed in this work for the section 2. Layer and three different locations of the source rocks are reported (see colors in legend). A) The oil expulsion from the active source rock during the Late Cretaceous and Mainly vertical migration upwards into the reservoir rocks. B) First accumulations of heavier oil under Cigno/Vallecupa oil fields, occurred after the deposition of the Messinian evaporites acting as a seal. C) Lateral migration from Cigno/Vallecupa area to Majella with subsequently biodegradation of oils. Here I reported two key wells for the study area. Also, the API degree measured in laboratory (Chapter 1) and reported for the Cigno/Vallecupa oil fields are shown.*

3.5 Conclusion

Although the basin modelling analysis are still in progress, some observations can be drawn over the possible evolution experienced by the Burano-Bolognano petroleum system for which I have proposed a conceptual model.

The dense well dataset available for the northern sector of the Majella mountain and the Cigno/Vallecupa oil fields, has allow to reconstruct an accurate stratigraphic framework that resulted to be laterally continuous and coherent with a ramp geometry. This ramp is extended from the Majella area, where the margin of the Apulia carbonate platform is exposed, to distal basin domain in the Cigno/Vallecupa oil fields, where a deeper burial due to a thicker foredeep succession are characterized the evolution of the petroleum system.

The 2D modelling work, performed on the Burano-Bolognano petroleum system, indicates very clearly that the oil occurrences known along the NW flank of the Majella mountainand in the nearby subsurface oil fields of Cigno and Vallecupa, must been derived by kitchen areas located to the north and more deeply buried below the Cigno/Vallecupa oil fields, although the whole Triassic interval is mature. Modelling also suggest that after the oil expulsion occurred in the Late Cretaceous, mainly efficient mechanism of fluid movement has been a vertical primary migration, and hydrocarbons are entrapped in the Late Miocene when seal formations, such as Hemipelagic Marls and Messinian evaporites, are deposited. Then, hydrocarbons have migrated laterally along the pre-Pliocene fault systems, acting as conduit for fluid flow, and within the Miocene reservoir intervals towards the Majella mountain. Here the migration in the shallower reservoir has caused a gradual biodegradation of original hydrocarbon, as also demonstrated by the decrease of oil density from northwest to southeast sectors.

Conclusions

The work presented in this dissertation aimed to provide petrophysical studies and fluid-flow simulations to reduce the uncertainty that affects carbonate reservoir characterization due to their heterogeneities.

I reported a petrophysical characterization, conducted on carbonate samples with different hydrocarbon contents, belonging to the Bolognano Formation, which represents the reservoir interval of the Burano-Bolognano petroleum system, in Abruzzo Region. Laboratory results, performed at ambient temperature and with increasing confining pressure, highlight that the presence of hydrocarbon within the carbonate samples tends to increase P- and S-wave velocities. Since hydrocarbon properties are temperature dependent, I also investigated the variation of wave velocities with increasing temperature, from 25° to 90 °C. The analysis shows that wave velocities decrease with increasing temperature and also the amount of hydrocarbon within samples has a significant influence. In fact, I observed a linear reduction of velocities with increasing temperature for low hydrocarbon-bearing samples, whereas for high hydrocarbon -bearing sample a distinct trend at around 50°-60 °C, suggesting a change of the physical properties of hydrocarbon. Based on these laboratory observations, I developed a new model for the estimation of the P-wave velocity as a function of temperature (from 30° to 90 °C), suggesting that the velocity change seems to be more linked to the absolute volume of hydrocarbon respect to the sample saturation. Moreover, the presence of viscous fluid determined an almost ideal-elastic behaviour for heavy oil-bearing samples and more inelastic behaviours for clean samples. These data are confirmed by loading-unloading tests performed on the same lithology and from the outcrop observations that show a less fractured hydrocarbon-bearing portions respect to clean outcrops.

Since the investigated reservoir is regarded as an analogue of a faulted and fractured reservoir, I also investigated the influence of fluids on fault slip behaviour performing frictional experiments on mixture of carbonate and clay fault gouges. The coupling effect of the fluid and clay minerals tend to affect frictional strength, stability, and healing of fault gouge, composed of strong and weak minerals, and it is still poorly constrained. Starting from a calcite-bearing fault gouge the increasing shale content determines a significant reduction in friction from about 0.71 to 0.43.

This frictional weakening is accompanied by an evolution from a load-bearing microstructure in calcite gouges, where deformation occurs by grain size-reduction and localization along BYR_1 shear, to interconnected layers of clays where Y and rotated R_1 shear zones are linked with a P foliation formed by aligned clay lamellae. This reduction in friction, determined by the presence of clay, is also marked with the presence of saturated fluid. Under this condition, I observe a more significant reduction in frictional strength (μ=0.65-0.37), a near-zero healing and a velocity strengthening behaviour, likely due to the adsorbed or interlayer water on sheet mineral structures and develop the interconnected weak layer of clay lamellae. This means that for faults cutting across sedimentary sequences composed of carbonates and clay-rich sediments and under saturated conditions, the clay concentration and its interconnectivity promote fault weakening, hence facilitating fault reactivation. Upon reactivation the marked rate-strengthening behaviour of clay-rich shear zones point to a slip behaviour characterized by aseismic creep.

As the last part of my research, I integrated laboratory results to better understand and constrain the key factors, such as fluid properties and their influence on the petrophysical and frictional properties, that can influence the geological evolution of the petroleum system and the related fluids movements over the geological time. A 3D structural model has been constructed for the main reservoir interval filled by hydrocarbon, using the Petrel software, and then I performed simulation models of hydrocarbon generation and migration in time and space along two-dimensional geological sections, extracted by Petrel project, using the PetroMod software.
Geometry of the surfaces, derived from well correlations, depicts a coherent and continuous stratigraphic framework. This geometry can be associated with a ramp geometry that extended from the Majella area, where the margin of the Apulia carbonate platform is exposed, to distal basin domain in the Cigno/Vallecupa oil fields, where a deeper burial due to a thicker foredeep succession are characterized the evolution of the petroleum system. The 2D modelling exercise highlights that the source rock, responsible for the oil occurrences known in the study area, is located to the north respect the Majella mountain, more deeply buried below the Cigno/Vallecupa oil fields. After the oil expulsion from the active source rock occurred in the Late Cretaceous, the most efficient mechanism for fluids movements is a vertical primary migration hydrocarbon towards the overlying reservoir rocks. Hydrocarbons are entrapped into the Late Miocene when seal formations, such as Hemipelagic Marls and Messinian evaporites, are deposited.

Then, a lateral migration is established through the pre-Pliocene fault systems and within Miocene reservoir intervals towards the Majella Mountain. Here the migration in the shallower reservoir has caused a gradual biodegradation of original hydrocarbon, as also demonstrated by the decrease of oil density from northwest to southeast sectors.

To conclude, based on these results and considerations, this study provides input and possible directions for future research to better constrain the geographical position of the source rock that have caused the hydrocarbon distributions. For this scope, an important data, for instance, is given by geochemical analysis of the generated oil. Thus, the results of my research will be useful to other geologists, geophysics and explorationists as an integrated analogue to support projects and exploration studies elsewhere. Moreover, this will improve the carbonate reservoir knowledge that is still poorly understood due to high heterogeneities related to fabric, texture, fractures that characterize those reservoirs.

Appendix A

Supporting Information for Chapter 1

- Figure SA.1: Examples of the ultrasonic waveforms, recorded for a high HHC-bearing sample at low (30°C) and high temperature (90°C) and the corresponding picking of the P- and S-wave arrivals. The signal of a representative high HHC-bearing samples shows a strong attenuation at higher temperature. The S-wave arrival has been picked when I observed a change in amplitude and wavelength of the S signal.

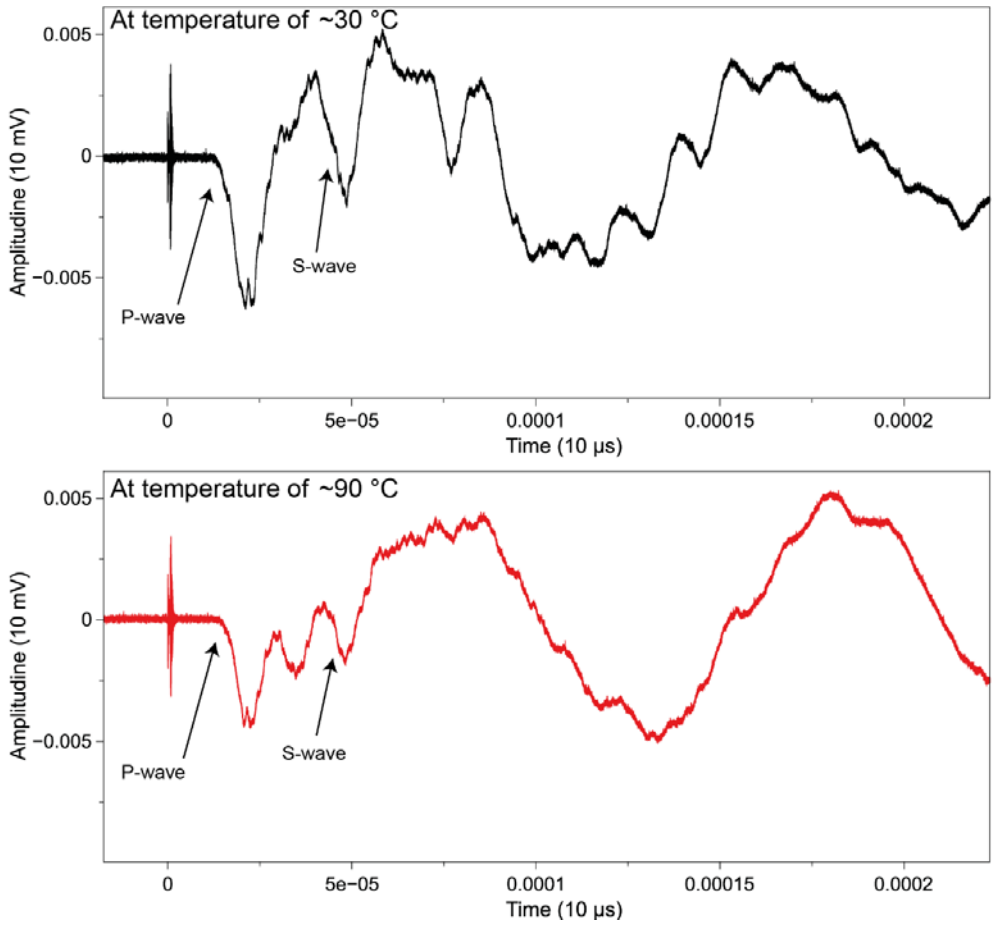

Figure SA.1*: Example of waveforms recorded at ambient pressure with S-type piezoelectric transducer at low (30°C-black line) and high temperature (90°C-red line).*

Appendix B

Supporting Information for Chapter 2

- Figure SB.1 illustrates the evolution of frictional strength as a function of displacement for all experiments conducted on calcite-shale mixtures at normal stress of 30, 50 and 100 MPa. The friction tests have been carried out at room-dry (left side) and under $CaCO_3$-equilibrated waters (right side) conditions.

- Figure SB.2 provides SEM detailed images of mixtures composed of 50 wt.% calcite and 50 wt.% shale that are sheared at normal stress of 100 MPa under room-dry and wet conditions.

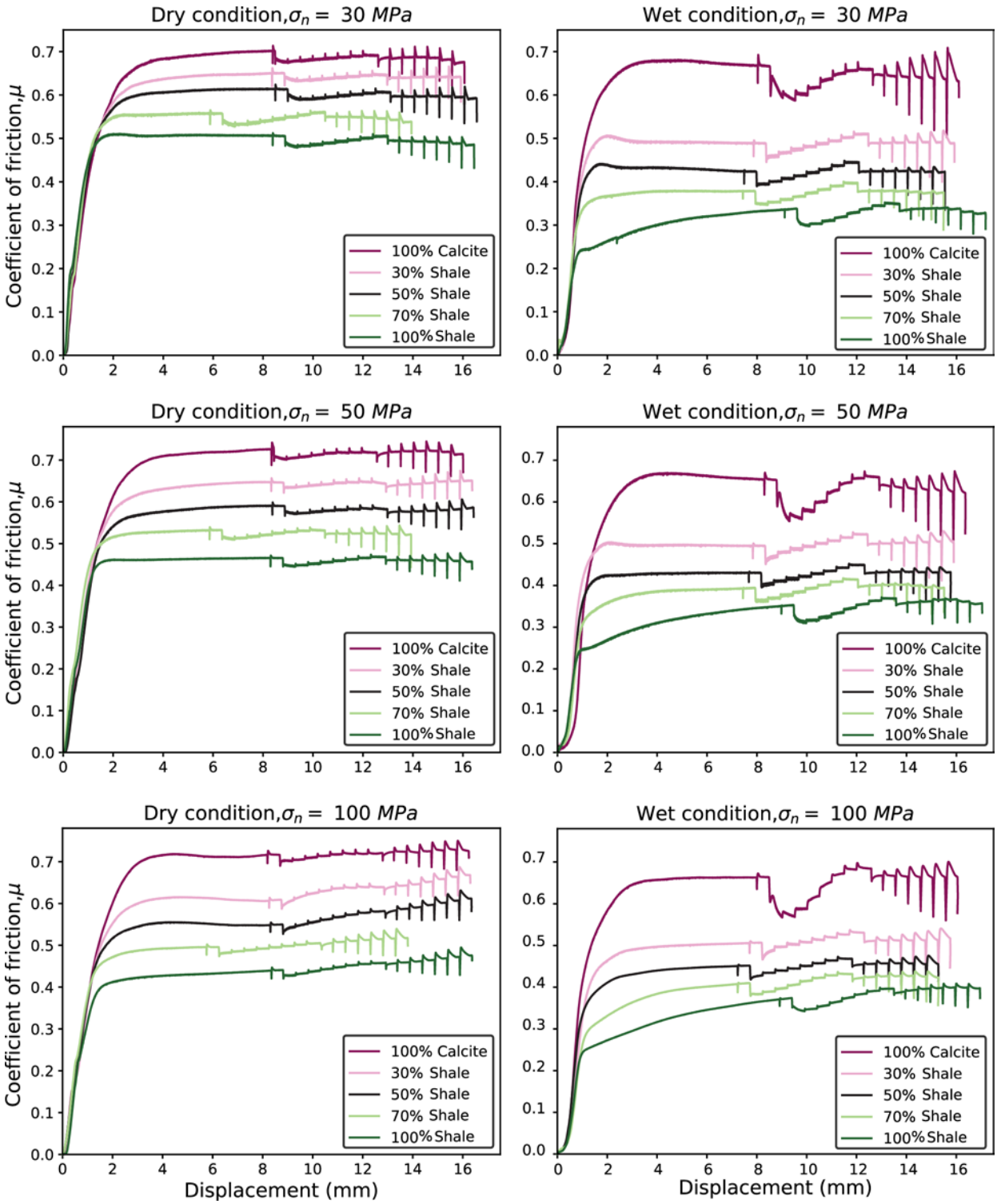

Figure SB.1. *The coefficient of friction ($\mu=\tau/\sigma_n$) is plotted against displacement (mm) for all experiments performed under different conditions: dry condition, i.e., room humidity, (left side) and $CaCO_3$-equilibrated water condition (right side). These experiments were performed on different fault gouge samples: shale content is increased from 0% to 100% in weight respect to the calcite content.*

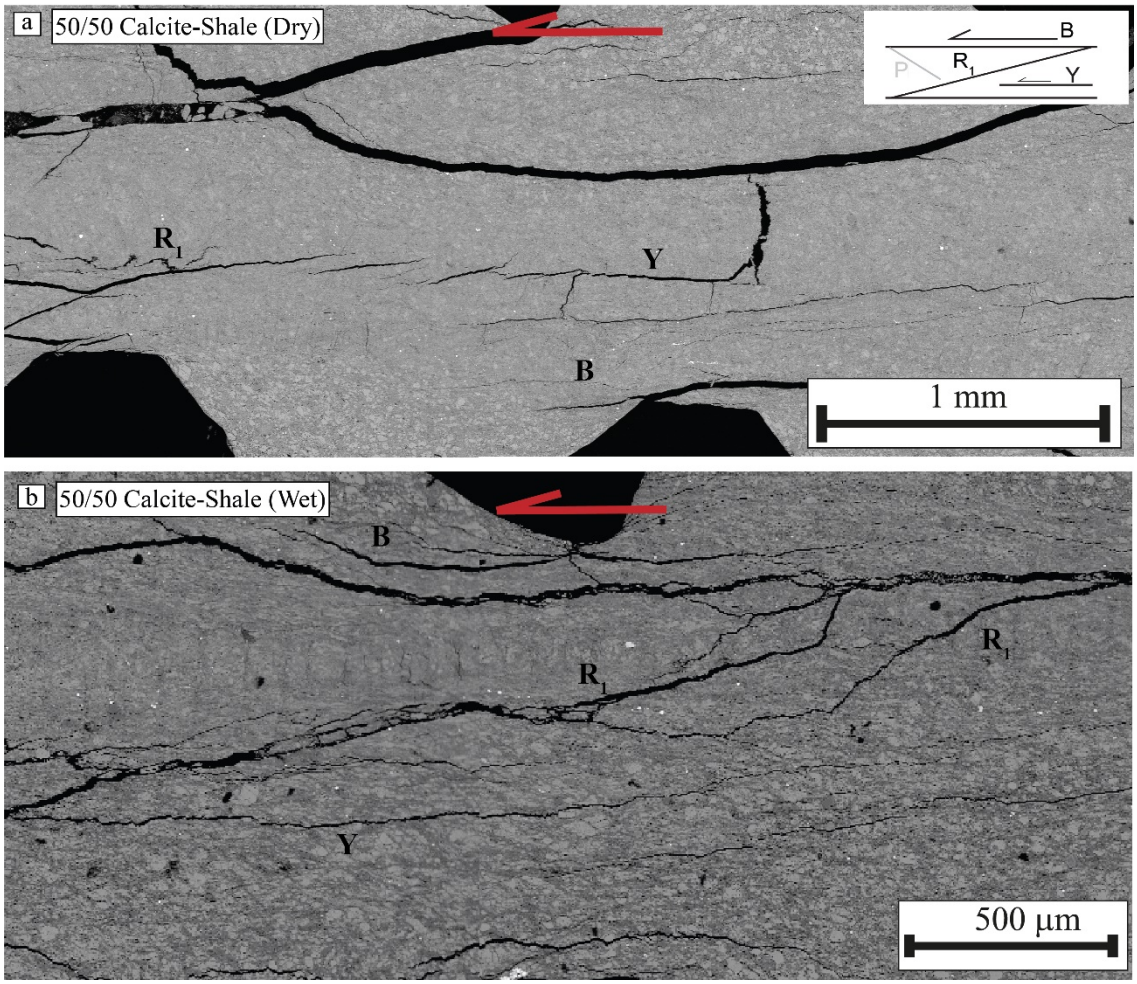

Figure SB.2. *SEM images of 50/50 calcite-shale mixtures collected after friction experiments conducted at normal stress of 100 MPa under (a) room-dry) and (b) wet conditions. A typical geometry of BYR$_1$ shear planes can be observed within the entire gouges.*

Appendix C

Supporting Information for Chapter 3

- Figure SC.1 shows the depth map of the Orte formation top that represents the reservoir top for the Cigno oil field.
- Figure SC.2 reports the boundary conditions, necessary in the fluid flow simulations to ensure the definition of the basic energetic conditions for temperature and burial history of the source rock and, consequently, for the maturation of organic matter through time Specifically, I reported the Paleo-Water-Depths, sediment water interface temperature (SWIT) and heat flow (HF).
- Figure SC.3 illustrates the evolution of paleo-temperature at the selected hemisphere and latitude (Northern Mediterranean and 42°) over geological time.

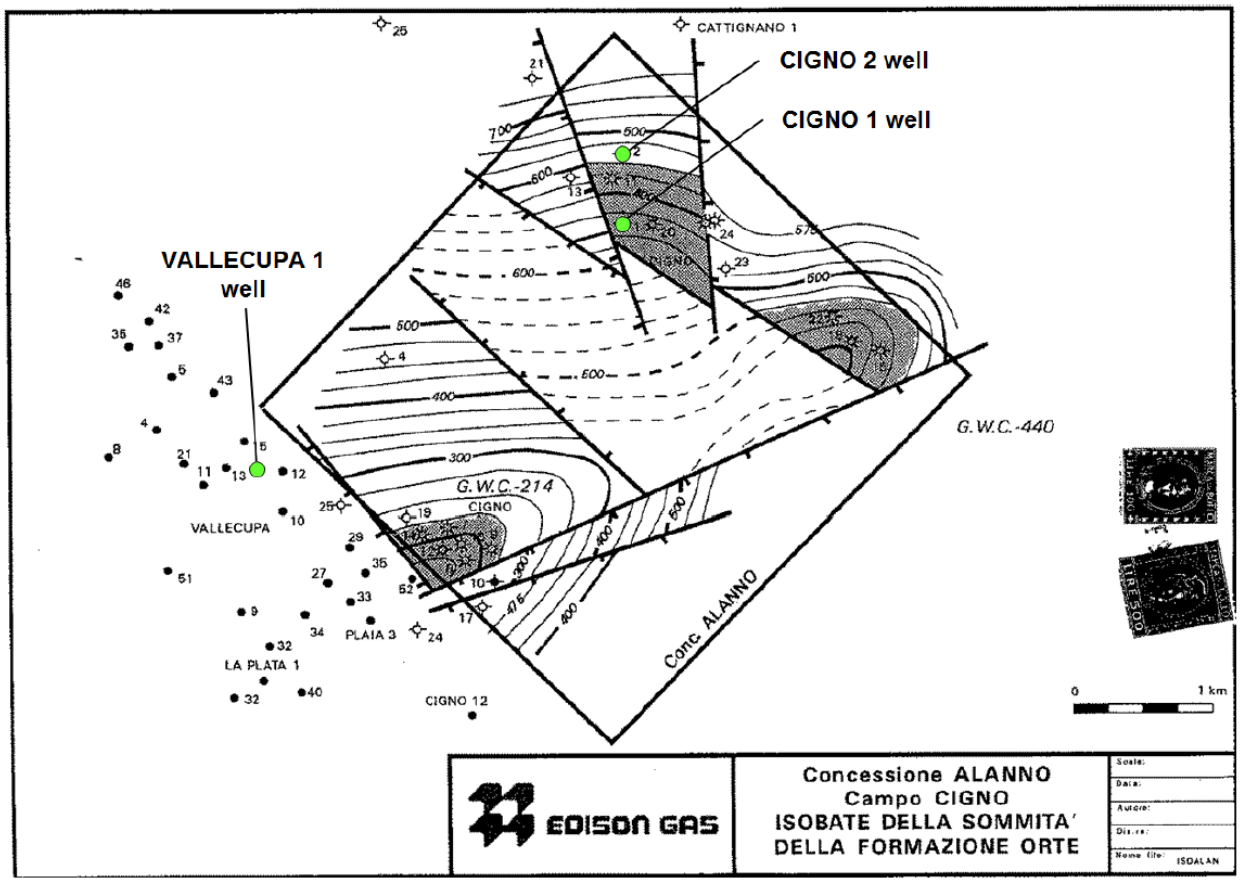

Figure SC.1: *Depth map of top reservoir (Orte formation), within the Alanno Production Concession at Cigno oil field (modified after Edison Gas, 1999).*

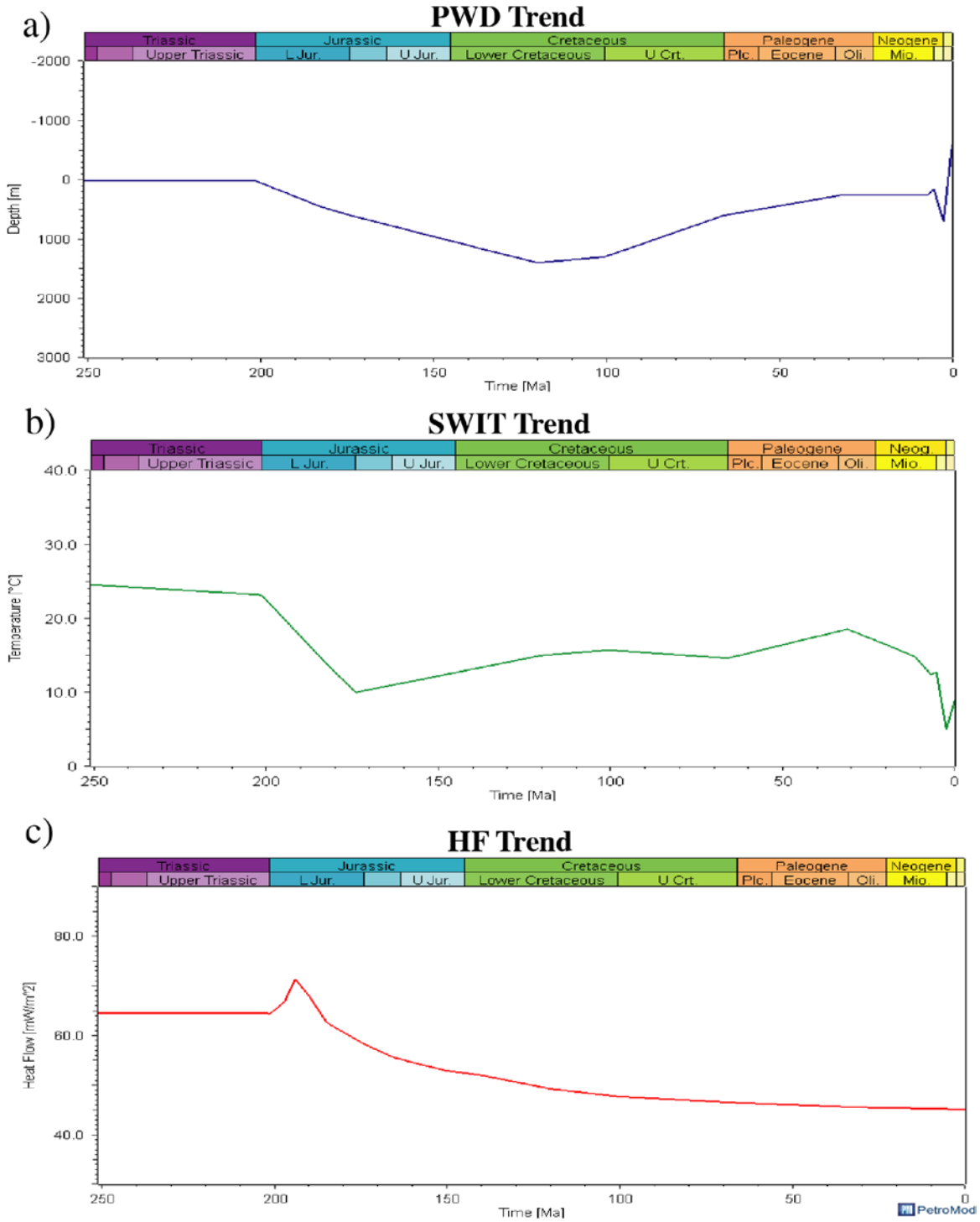

***Figure SC.2**: Boundary conditions trends for all simulation models. a) Paleo Water Depth, b) Sediment Water Interface Temperature and c) Heat Flow (45 mW/m2 at present-day).*

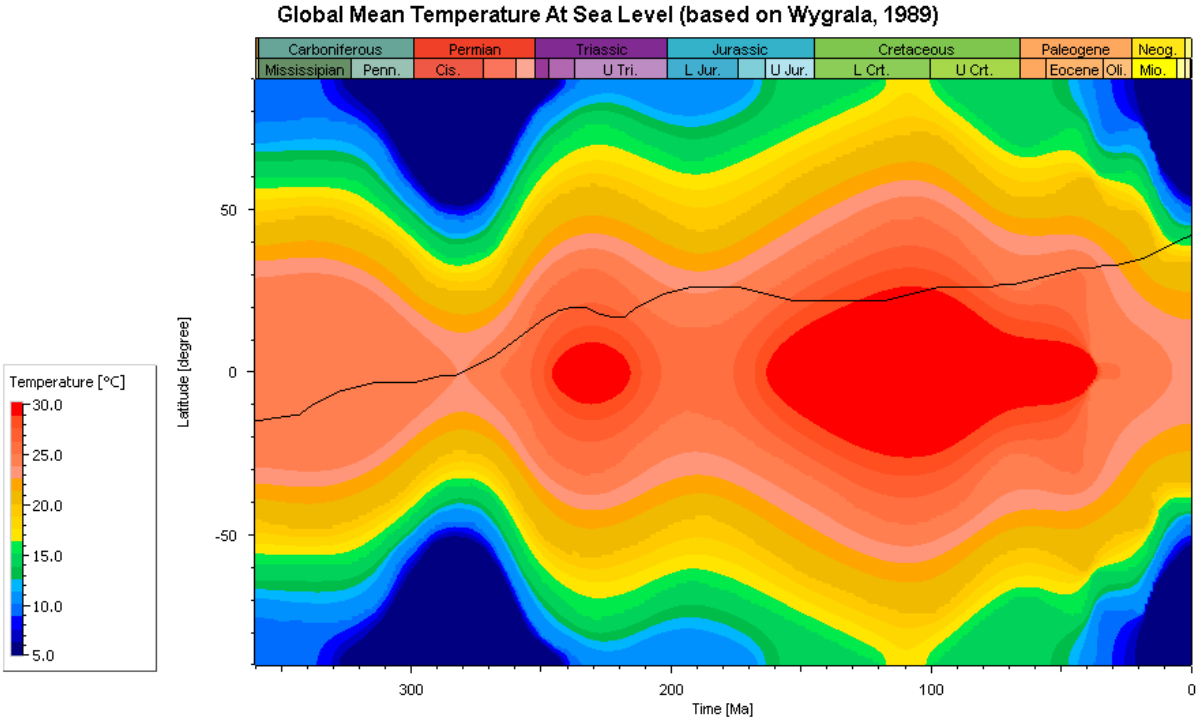

***Figure SC.3**: Paleo-temperature profile for the modelled area, reconstructed using the semiautomatic tool with the PetroMod software. It is based on Wygrala, (1989) and extracts a standard temperature at sea level over geological time setting the geographic location (North Mediterranean) and the latitude (42°).*

Appendix D

List of experiments

D1. Petrophysical characterization with increasing temperature (Chapter 1)

ID Sample	Measurements Description
ACF1-1	Porosity, P- and S-wave velocities at increasing temperature (25°-90°C)
ACF1-2	Porosity, P- and S-wave velocities at increasing temperature (25°-90°C)
ACF1-3	Porosity, P- and S-wave velocities at increasing temperature (25°-90°C)
ACF1-5	Porosity, P- and S-wave velocities at increasing temperature (25°-90°C)
CR1b	Porosity, P- and S-wave velocities at increasing temperature (25°-90°C)
CR1c	Porosity, P- and S-wave velocities at increasing temperature (25°-90°C)
CR1-2	Porosity, P- and S-wave velocities at increasing temperature (25°-90°C)
CR3-1	Porosity, P- and S-wave velocities at increasing temperature (25°-90°C)
CR3b	Porosity, P- and S-wave velocities at increasing temperature (25°-90°C)

D2. Petrophysical characterization with increasing pressure (Chapter 1)

ID Sample	Mesurements Description
ACF2a	Porosity, P- and S-wave velocities at increasing pressure (0.1-100 MPa)
ACF3b	Porosity, P- and S-wave velocities at increasing pressure (0.1-100 MPa)
ACF4a'	Porosity, P- and S-wave velocities at increasing pressure (0.1-100 MPa)
ACF4b	Porosity, P- and S-wave velocities at increasing pressure (0.1-100 MPa)
ACF4c	Porosity, P- and S-wave velocities at increasing pressure (0.1-100 MPa)
FDP1a'	Porosity, P- and S-wave velocities at increasing pressure (0.1-100 MPa)
FDP1c'	Porosity, P- and S-wave velocities at increasing pressure (0.1-100 MPa)
CAP1d	Porosity, P- and S-wave velocities at increasing pressure (0.1-100 MPa)
CR2a	Porosity, P- and S-wave velocities at increasing pressure (0.1-100 MPa)
CR2c	Porosity, P- and S-wave velocities at increasing pressure (0.1-100 MPa)
CR3a	Porosity, P- and S-wave velocities at increasing pressure (0.1-100 MPa)
CR3b	Porosity, P- and S-wave velocities at increasing pressure (0.1-100 MPa)
ACF5c"	Porosity, P- and S-wave velocities at increasing pressure (0.1-100 MPa)
ACF5a	Porosity, P- and S-wave velocities at increasing pressure (0.1-100 MPa)
ACF1f'	Porosity, P- and S-wave velocities at increasing pressure (0.1-100 MPa)
ACF1e'	Porosity, P- and S-wave velocities at increasing pressure (0.1-100 MPa)
ACF1c"	Porosity, P- and S-wave velocities at increasing pressure (0.1-100 MPa)
ACF1b'	Porosity, P- and S-wave velocities at increasing pressure (0.1-100 MPa)

D3. Friction Experiments under room-humidity conditions (Chapter 2)

Experiment number	Configuration Description
b769	double direct shear on gouge (5 cm x 5 cm nominal contact area)-Room Humidity
b770	double direct shear on gouge (5 cm x 5 cm nominal contact area)-Room Humidity
b771	double direct shear on gouge (5 cm x 5 cm nominal contact area)-Room Humidity
b772	double direct shear on gouge (5 cm x 5 cm nominal contact area)-Room Humidity
b773	double direct shear on gouge (5 cm x 5 cm nominal contact area)-Room Humidity
b779	double direct shear on gouge (5 cm x 5 cm nominal contact area)-Room Humidity
b780	double direct shear on gouge (5 cm x 5 cm nominal contact area)-Room Humidity
b781	double direct shear on gouge (5 cm x 5 cm nominal contact area)-Room Humidity
b782	double direct shear on gouge (5 cm x 5 cm nominal contact area)-Room Humidity
b784	double direct shear on gouge (5 cm x 5 cm nominal contact area)-Room Humidity
b786	double direct shear on gouge (5 cm x 5 cm nominal contact area)-Room Humidity
b787	double direct shear on gouge (5 cm x 5 cm nominal contact area)-Room Humidity
b796	double direct shear on gouge (5 cm x 5 cm nominal contact area)-Room Humidity
b797	double direct shear on gouge (5 cm x 5 cm nominal contact area)-Room Humidity
b798	double direct shear on gouge (5 cm x 5 cm nominal contact area)-Room Humidity

D4. Friction Experiments under wet conditions (Chapter 2)

Experiment number	Configuration Description
b799	double direct shear on gouge (5 cm x 5 cm nominal contact area)-Fluid Saturated
b800	double direct shear on gouge (5 cm x 5 cm nominal contact area)-Fluid Saturated
b801	double direct shear on gouge (5 cm x 5 cm nominal contact area)-Fluid Saturated
b802	double direct shear on gouge (5 cm x 5 cm nominal contact area)-Fluid Saturated
b803	double direct shear on gouge (5 cm x 5 cm nominal contact area)-Fluid Saturated
b806	double direct shear on gouge (5 cm x 5 cm nominal contact area)-Fluid Saturated
b807	double direct shear on gouge (5 cm x 5 cm nominal contact area)-Fluid Saturated
b808	double direct shear on gouge (5 cm x 5 cm nominal contact area)-Fluid Saturated
b809	double direct shear on gouge (5 cm x 5 cm nominal contact area)-Fluid Saturated
b810	double direct shear on gouge (5 cm x 5 cm nominal contact area)-Fluid Saturated
b811	double direct shear on gouge (5 cm x 5 cm nominal contact area)-Fluid Saturated
b812	double direct shear on gouge (5 cm x 5 cm nominal contact area)-Fluid Saturated
b814	double direct shear on gouge (5 cm x 5 cm nominal contact area)-Fluid Saturated
b815	double direct shear on gouge (5 cm x 5 cm nominal contact area)-Fluid Saturated
b816	double direct shear on gouge (5 cm x 5 cm nominal contact area)-Fluid Saturated

Acknowledgements

Looking back on all the exciting experiences I have had, and all the friends I have made during these three years of hard work, I feel extremely lucky and grateful to them.

First, I express my honest gratitude to my thesis supervisors, Prof. Fabio Trippetta. I am very glad that he has introduced me to such an interesting topic, Petroleum System Modelling, since when I was a bachelor student. It was an honor to work with such a great Professor who has excellent knowledge and expertise in this field. During these years, his continuous support and advises have been fundamental for my personal and scientific growth.

Many thanks to Prof. Cristiano Collettini, Prof.ssa Elisa Tinti, Prof. Marco Brandano and Dr. Marco Scuderi for all the support and helpfulness they showed me, always finding time to discuss and advise me during my scientific research.

I thank ENI oil company, in particular the research team composed by Dr. Marco Brignoli, Dr. Stefano Mantica, Dr. Stefania Petroselli, Dr. Lorenzo Osculati and Dr. Giorgio Volontè, with whom I had the opportunity to collaborate studying the frictional properties of carbonate-clay fault through friction tests.
Schlumberger is thanked for providing access to Petrel and PetroMod software: in particular I thank my Dr. Alessandro Romi from the Milan office for his support in developing the 3D geological model with Petrel Software.
I also thank INGV of Rome and all the researchers I met for their support and suggestions during the experiments, conducted in the HP-HT laboratory.

Some great thanks go indeed to Domenico Mannetta for the amazing thin sections he provided. Thanks for the infinite patience and availability.

CNIS laboratory (University of Rome, Sapienza) and FESEM laboratory of CNR-IGAG/Department of the Earth Sciences for their assistance during the microstructural analysis. Their support and help have been fundamental.

A great thank is for the reviewers of this thesis: Prof. Fabrizio Balsamo (University of Parma) and Prof. Andrea Bistacchi (University of Milan – Bicocca).

Finally, a special thanks goes to my family who, despite all the difficulties, have always been close to me and help, never making me miss anything to try to live these three years "peacefully".

A special thanks goes to my family who, despite all the difficulties, have always been close to me, helping and making me miss anything to try to live these three years "peacefully".

Thanks to all my friends and to my colleagues which provided much needed feedback and encouragement!

February 2021

Roberta Ruggieri

References

Websites

GeoThopica Database: http://geothopica.igg.cnr.it/

Shlumberger Oilfield Glossary: https://www.glossary.oilfield.slb.com/

Shlumberger Petrel software: https://www.software.slb.com/products/petrel

Shlumberger PetroMod software: https://www.software.slb.com/products/petromod

ViDEPI Project (2012). Visibility of petroleum exploration data in Italy. MISE, Ministero dello sviluppo economico DGRME, Società Geologica Italiana, and Assomineraria. http://unmig.sviluppoeconomico.gov.it/videpi/videpi.asp.

Printed Sources

ALBA (August 1942) - Campagna geologica ALBA – Scala 1:25.000, versante Nord-Ovest della Maiella – Quadro indice (10th of August 1942). ENI S.p.A. Historical Archives, Roma. (doc. n. 48449).

ALBA (July 1943) - Relazione sulla Campagna dei Sondaggi e Cubaggio accertato e probabile del giacimento asfaltico-bituminoso del versante settentrionale della Maiella. In Campagna Geologica ALBA. ENI S.p.A. Historical Archives, Roma. (doc. n. 48449).

Adam, L., Batzle, M., Lewallen, K. T., & van Wijk, K., (2009). Seismic wave attenuation in carbonates. Journal of Geophysical Research: Solid Earth, 114 (B6). https://doi.org/10.1029/2008JB005890.

Agosta, F., Prasad, M., Aydin, A., (2007). Physical properties of carbonate fault rocks, fucino basin (Central Italy): Implications for fault seal in platform carbonates. Geofluids 7, 19–32. https://doi.org/10.1111/j.1468-8123.2006.00158.x

Agosta, F., Alessandroni, M., Tondi, E., Aydin, A., (2009). Oblique normal faulting along the northern edge of the Majella Anticline, central Italy: Inferences on hydrocarbon migration and accumulation. J. Struct. Geol. 31, 674–690. https://doi.org/10.1016/j.jsg.2009.03.012

Agosta, F., Alessandroni, M., Antonellini, M., Tondi, E., & Giorgioni, M. (2010). From fractures to flow: A field-based quantitative analysis of an outcropping carbonate reservoir. Tectonophysics, 490(3-4), 197-213.

Allen, P. A., & Allen, J. R. (2013). Basin analysis: Principles and application to petroleum play assessment. John Wiley & Sons.

Anselmetti, F. S., and Eberli, G. P., (1993). Controls on sonic velocity in carbonates. Pure and Applied Geophysics, 141 (2-4), 287-323.

Anselmetti, F. S., G. P. Eberli, and D. Bernoulli, (1997). Seismic modelling of a carbonate platform margin (Montagna della Maiella, Italy): Variations in seismic facies and implications for sequence stratigraphy. Carbonate seismology: Society of Exploration Geophysicists Geophysical Developments Series 6, 373–406.

Athy, L. F. (1930). Density, porosity, and compaction of sedimentary rocks. Aapg Bulletin, 14(1), 1-24.

Aydin, A., (2000). Fractures, faults, and hydrocarbon entrapment, migration and flow. Mar. Pet. Geol. 17, 797–814. https://doi.org/10.1016/S0264-8172(00)00020-9

Baccheschi, P., De Gori, P., Villani, F., Trippetta, F., & Chiarabba, C. (2020). The preparatory phase of the Mw 6.1 2009 L'Aquila (Italy) normal faulting earthquake traced by foreshock time-lapse tomography. Geology, 48(1), 49-55.

Balsamo, F., & Storti, F. (2010). Grain size and permeability evolution of soft-sediment extensional sub-seismic and seismic fault zones in high-porosity sediments from the Crotone basin, southern Apennines, Italy. Marine and Petroleum Geology, 27(4), 822-837.

Barchi, M.R., Minelli, G., Pialli, G., (1998). The crop 03 profile: a synthesis of results on deep structures of the Northern Apennines. Mem. Soc. Geol. Ital. 52, 383e400.

Bardainne, T., Dubos-Sallée, N., Sénéchal, G., Gaillot, P., and Perroud, H. (2008) Analysis of the induced seismicity of the Lacq gas field (Southwestern France) and model of deformation. Geophys. J. Int. 172, 3, 1151-1162.

Barnes, P. M., Wallace, L. M., Saffer, D. M., Bell, R. E., Underwood, M. B., Fagereng, A., ... & Kitajima, H. (2020). Slow slip source characterized by lithological and geometric heterogeneity. Science Advances, 6(13), eaay3314.

Batzle, M., Hofmann, R., and Han, D. H., (2006). Heavy oils—Seismic properties. The Leading Edge, 25 (6), 750-756. doi:10.1190/1.2210074.

Baud, P., Vinciguerra, S., David, C., Cavallo, A., Walker, E., & Reuschlé, T. (2009). Compaction and failure in high porosity carbonates: Mechanical data and microstructural observations. Pure and Applied Geophysics, 166(5-7), 869-898.

Baud, P., Rolland, A., Heap, M., Xu, T., Nicolé, M., Ferrand, T., Reuschlé, T., Toussaint, R., Conil, N., (2016). Impact of stylolites on the mechanical strength of limestone. Tectonophysics 690, 4–20. https://doi.org/10.1016/j.tecto.2016.03.004

Baud, P., Exner, U., Lommatzsch, M., Reuschlé, T., Wong, T.F., 2017. Mechanical behaviour, failure mode, and transport properties in a porous carbonate. J. Geophys. Res. Solid Earth 122, 7363–7387. https://doi.org/10.1002/2017JB014060.

Beeler, N.M., (2007). Laboratory-observed faulting in intrinsically and apparently weak materials. In: Dixon, T.H., Moore, J.C. (Eds.), The Seismogenic Zone of Subduction Thrust Faults, pp. 370–449.

Behnsen, J., & Faulkner, D. R. (2012). The effect of mineralogy and effective normal stress on frictional strength of sheet silicates. Journal of Structural Geology, 42, 49–61. https://doi.org/10.1016/j.jsg.2012.06.015

Bernard, P., Briole, P., Meyer, B., Lyon-Caen, H., Gomez, J. M., Tiberi, C., ... & Lebrun, B. (1997). The M s= 6.2, June 15, 1995 Aigion earthquake (Greece): evidence for low angle normal faulting in the Corinth rift. Journal of Seismology, 1(2), 131-150.

Bigi, S., Conti, A., Casero, P., Ruggiero, L., Recanati, R., Lipparini, L., (2013). Geological model of the central Periadriatic basin (Apennines, Italy). Mar. Pet. Geol. 42, 107–121. https://doi.org/10.1016/j.marpetgeo.2012.07.005

Bistacchi, A., Mittempergher, S., Martinelli, M., & Storti, F. (2020). On a new robust workflow for the statistical and spatial analysis of fracture data collected with scanlines (or the importance of stationarity). Solid Earth Discussions, 1-18.

Blanpied, M.L., Marone, C.J., Lockner, D.A., Byerlee, J.D. & King, D.P., (1998). Quantitative measure of the variation in fault rheology due to fluid- rock interactions, J. geophys. Res., 103, 9691–9712.

Brandano, M., Scrocca, D., Lipparini, L., Petracchini, L., Tomassetti, L., Campagnoni, V., Meloni, D. and Mascaro, G. (2013). Physical stratigraphy and tectonic settings of Bolognano Formation (Majella): a potential carbonate reservoir. In Journal of Mediterranean Earth Sciences Pre-Congress Field trip guide, 151-176.

Brandano, M., Cornacchia, I., Raffi, I., and Tomassetti, L., (2016). The Oligocene–Miocene stratigraphic evolution of the Majella carbonate platform (Central Apennines, Italy). Sedimentary geology, 333, 1-14. doi:10.1016/j.sedgeo.2015.12.002

Brandano, M., Tomassetti, L., Trippetta, F., & Ruggieri, R. (2020). Facies heterogeneities and 3D porosity modelling in an Oligocene (upper Chattian) carbonate ramp, Salento Peninsula, southern Italy. Journal of Petroleum Geology, 43 (2), 191-208.

Bullock, R.J., De Paola, N., Holdsworth, R.E., Trabucho-Alexandre, J., (2014). Lithological controls on the deformation mechanisms operating within carbonate-hosted faults during the seismic cycle. J. Struct. Geol. 58, 22–42. https://doi .org /10. 1016 /j.jsg .2013 .10 .008.

Burchfiel, B.C., Royden, L.H., van der Hilst, R.D., Hager, B.H., Chen, Z., King, R.W., Li, C., Lü, J., Yao, H., Kirby, E., (2008). A geological and geophysical context for the Wenchuan earthquake of 12 May 2008, Sichuan, People's Republic of China. GSA Today 18, 4. http://dx.doi.org/10.1130/gsatg18a.1.

Byerlee, J. D. (1978), Friction of rocks, Pure Appl. Geophys., 116, 615–626, doi:10.1007/BF00876528.

Caine, J.S., Evans, J.P., Forster, C.B., 1996. Fault zone architecture and permeability structure. Geology 24, 1025–1028.

Campana, F., Fantoni, R., Masetti, D., & Scotti, P. (2017). Stratigraphic and naphthogenic characterization of the Sparviero 1 bis Mesozoic succession (Southern Adriatic basin, Italy). Journal of Mediterranean Earth Sciences, 9, 89-93.

Cappa, F., Scuderi, M. M., Collettini, C., Guglielmi, Y., & Avouac, J. P. (2019). Stabilization of fault slip by fluid injection in the laboratory and in situ. Science advances, 5(3), eaau4065.

Carminati, E., Corda, L., Mariotti, G., Scifoni, A., & Trippetta, F. (2013). Mesozoic syn-and postrifting evolution of the central Apennines, Italy: the role of triassic evaporites. The Journal of Geology, 121(4), 327-354.

Carpenter, B. M., C. Marone, and D. M. Saffer (2011), Weakness of the San Andreas Fault revealed by samples from the active fault zone, Nat. Geosci., 4, 251–254, doi:10.1038/ngeo1089

Carpenter, B.M., Collettini, C., Viti, C., Cavallo, A., (2016). The influence of normal stress and sliding velocity on the frictional behaviour of calcite at room temperature: insights from laboratory experiments and microstructural observations. Geophys. J. Int. 205 (1), 548e561

Cazzini, F., Zotto, O.D., Fantoni, R., Ghielmi, M., Ronchi, P., Scotti, P., (2015). Oil and Gas in the Adriatic Foreland , Italy. J. Pet. Geol. 38, 255–279.

Chen, X., Rabbani A., Schmitt D., and Kofman R., (2015a). Laboratory study of the seismic properties on bitumen saturated carbonates from Grosmont Formation, Alberta: 3rd International workshop on rock physics, 1-3.

Chen, J., B. A. Verberne, and C. J. Spiers (2015b), Effects of healing on the seismogenic potential of carbonate fault rocks: Experiments on samples from the Longmenshan Fault, Sichuan, China, J. Geophys. Res. Solid Earth, 120, 5479–5506, doi:10.1002/2015JB012051

Chiarabba, C., Piccinini, D., de Gori, P., (2009). Velocity and attenuation tomography of the Umbria Marche 1997 fault system: Evidence of a fluid-governed seismic sequence. Tectonophysics 476, 73–84. https://doi.org/10.1016/j.tecto.2009.04.004

Chopra, S., Lines, L. R., Schmitt, D. R., and Batzle, M. L. (Eds.)., (2010). Heavy oils: reservoir characterization and production monitoring. Society of Exploration Geophysicists.

Cilona, A., Baud, P., Tondi, E., Agosta, F., Vinciguerra, S., Rustichelli, A., Spiers, C.J., (2012). Deformation bands in porous carbonate grainstones : Field and laboratory observations. J. Struct. Geol. 45, 137–157. https://doi.org/10.1016/j.jsg.2012.04.012

Collettini, C., and R. E. Holdsworth (2004), Fault zone weakening and character of slip along low-angle normal faults: Insights from the Zuccale fault, Elba, Italy, J. Geol. Soc., 161, 1039–1051, doi:10.1144/0016-764903-179.

Collettini, C., Viti, C., Smith, S.A.F., Holdsworth, R.E., (2009). The development of interconnected talc networks and weakening of continental low-angle normal faults. Geology 37, 567–570.

Collettini, C., Carpenter, B. M., Viti, C., Cruciani, F., Mollo, S., Tesei, T., ... & Chiaraluce, L. (2014a). Fault structure and slip localization in carbonate-bearing normal faults: An example from the Northern Apennines of Italy. Journal of Structural Geology, 67, 154-166.

Collettini, C., G. Di Stefano, B. M. Carpenter, P. Scarlato, T. Tesei, S. Mollo, F. Trippetta, C. Marone, G. Romeo, and L. Chiaraluce (2014b), A novel and versatile apparatus for brittle rock deformation, Int. J. Rock Mech. Min., 66, 114–123, doi:10.1016/j.ijrmms.2013.12.005.

Collettini, C., Tesei, T., Scuderi, M. M., Carpenter, B. M., & Viti, C. (2019). Beyond Byerlee friction, weak faults and implications for slip behaviour. Earth and Planetary Science Letters, 519, 245-263.

Cosentino L. (2001) Integrated reservoir studies, Paris, Technip.

Cosentino, D., Cipollari, P., Marsili, P., & Scrocca, D. (2010). Geology of the central Apennines: a regional review. Journal of the Virtual Explorer, 36(11), 1-37.

Crawford, B. R., D. R. Faulkner, and E. H. Rutter (2008), Strength, porosity, and permeability development during hydrostatic and shear loading of synthetic quartz-clay fault gouge, J. Geophys. Res., 113, B03207, doi:10.1029/2006JB004634.

Crescenti, U., A. Crostella, G. Donzelli, and G. Raffi, (1969). Stratigrafia della serie calcarea dal Lias al Miocene nella regione marchigiano abruzzese: Parte II. Litostratigrafia, biostratigrafia, paleogeografia: Memorie della Societa Geologica Italiana, v. 9, 343–420.

Croizé, D., Ehrenberg, S.N., Bjørlykke, K., Renard, F., Jahren, J., (2010). Petrophysical properties of bioclastic platform carbonates: Implications for porosity controls during burial. Mar. Pet. Geol. 27, 1765–1774. https://doi.org/10.1016/j.marpetgeo.2009.11.008

David, C., Dautriat, J., Sarout, J., Delle Piane, C., Menéndez, B., Macault, R., Bertauld, D., (2015). Mechanical instability induced by water weakening in laboratory fluid injection tests. J. Geophys. Res. Solid Earth 120, 4171–4188. https://doi.org/10.1002/2015JB011894

De Paola, N., Faulkner, D. R., & Collettini, C. (2009). Brittle versus ductile deformation as the main control on the transport properties of low-porosity anhydrite rocks. Journal of Geophysical Research: Solid Earth, 114(B6).

Della Vedova, B., Bellani, S., Pellis, G., & Squarci, P. (2001). Deep temperatures and surface heat flow distribution. In Anatomy of an orogen: the Apennines and adjacent Mediterranean basins (pp. 65-76). Springer, Dordrecht.

Demaison, G., Huizinga, B.J., (1994). Genetic classification of petroleum systems using three factors: charge, migration and entrapment. AAPG Mem 60, 73–92. https://doi.org/10.1306/0C9B29BB-1710-11D7-8645000102C1865D.

Den Hartog, S. A., & Spiers, C. J. (2014). A microphysical model for fault gouge friction applied to subduction megathrusts. Journal of Geophysical Research: Solid Earth, 119(2), 1510-1529.

Dieterich, J. H. (1978), Time-dependent friction and the mechanics of stick-slip, Pure Appl. Geophys., 116, 790–805.

Dieterich, J. H. (1979), Modelling of rock friction: 1. Experimental results and constitutive equations, J. Geophys. Res., 84, 2161–2168,

Domenico, S. N. (1984). Rock lithology and porosity determination from shear and compressional wave velocity. Geophysics, 49 (8), 1188-1195. doi:10.1190/1.1441748

Donzelli G. (1968). *Studio geologico della Maiella*. Ed. Università Gabriele D'Annunzio, (Chieti-Pescara).

Eastwood, J. (1993). Temperature-dependent propagation of P-and S-waves in Cold Lake oil sands: Comparison of theory and experiment. Geophysics, 58 (6), 863-872. doi:10.1190/1.1443470

Eberli, G.P., Baechle, G.T., Anselmetti, F.S., Incze, M.L., (2003). Factors controlling elastic properties in carbonate sediments and rocks. Lead. Edge 22, 654–660. doi:10.1190/1.1599691

Ehrenberg, S. N., Eberli, G. P., Keramati, M., & Moallemi, S. A. (2006). Porosity-permeability relationships in interlayered limestone-dolostone reservoirs. Aapg Bulletin, 90(1), 91-114.

England, W. A., Mackenzie, A. S., Mann, D. M., & Quigley, T. M. (1987). The movement and entrapment of petroleum fluids in the subsurface. Journal of the Geological Society, 144(2), 327-347.

Eyre, T. S., Eaton, D. W., Garagash, D. I., Zecevic, M., Venieri, M., Weir, R., & Lawton, D. C. (2019). The role of aseismic slip in hydraulic fracturing–induced seismicity. Science advances, 5(8), eaav7172.

Fabricius, I. L., Bächle, G. T., & Eberli, G. P. (2010). Elastic moduli of dry and water-saturated carbonates—Effect of depositional texture, porosity, and permeability. Geophysics, 75(3), N65-N78.

Fagereng, Å., and R. H. Sibson (2010), Melange rheology and seismic style, Geology, 38, 751–754, doi:10.1130/G30868.1.

Faulkner, D. R., A. C. Lewis, and E. H. Rutter (2003), On the internal structure and mechanics of large strike-slip fault zones: Field observations of the Carboneras fault in southeastern Spain, Tectonophysics, 367, 235–251, doi:10.1016/S0040-1951(03)00134-3.

Faulkner, D.R., Jackson, C.A.L., Lunn, R.J., Schlische, R.W., Shipton, Z.K., Wibberley, C.A.J., Withjack, M.O., (2010). A review of recent developments concerning the structure, mechanics, and fluid flow properties of fault zones. J. Struct. Geol. 32, 1557–1575. https://doi.org/10.1016/j.jsg.2010.06.009.

Gassmann, F., (1951). Elastic waves through a packing of spheres. Geophysics, 16 (4), 673-685. doi.org/10.1190/1.1437718

Géraud, Y., Diraison, M., & Orellana, N. (2006). Fault zone geometry of a mature active normal fault: A potential high permeability channel (Pirgaki fault, Corinth rift, Greece). Tectonophysics, 426(1-2), 61-76.

Ghisetti, F., Vezzani, L., (2002). Normal faulting, extension and uplift in the outer thrust belt of the central Apennines (Italy): Role of the Caramanico fault. Basin Res. 14, 225–236. https://doi.org/10.1046/j.1365-2117.2002.00171.x

Giorgetti, C., Carpenter, B.M. & Collettini, C., (2015), Frictional behaviour of talc-calcite mixtures, J. geophys. Res., 120, 6614–6633. Doi:10.1002/2015JB011970.

Giorgioni, M., Cilona, A., Tondi, E., & Agosta, F. (2011). Fault Zone Properties In The Roman Valley Quarry Reservoir Analogue: Insight For Well Logs, Core And Field Data. In Offshore Mediterranean Conference and Exhibition. Offshore Mediterranean Conference.

Gratier, J.P., Dysthe, D.K., Renard, F., (2013). The role of pressure solution creep in the ductility of the Earth's upper crust. Adv. Geophys 54:47-179.

Grindrod, P. M., Heap, M. J., Fortes, A. D., Meredith, P. G., Wood, I. G., Trippetta, F., & Sammonds, P. R. (2010). Experimental investigation of the mechanical properties of synthetic magnesium sulfate hydrates: Implications for the strength of hydrated deposits on Mars. Journal of Geophysical Research: Planets, 115(E6).

Gross, M. R., Fischer, M. P., Engelder, T., & Greenfield, R. J. (1995). Factors controlling joint spacing in interbedded sedimentary rocks: integrating numerical models with field observations from the Monterey Formation, USA. Geological Society, London, Special Publications, 92(1), 215-233.

Gudmundsson, A., (2011). Rock fractures in geological processes. Cambridge University Press.

Hairabian, A., Fournier, F., Borgomano, J., Nardon, S., (2014). Depositional facies, pore types and elastic properties of deep-water gravity flow carbonates. J. Pet. Geol. 37, 231–249. https://doi.org/10.1111/jpg.12581

Hairabian, A., Borgomano, J., Masse, J. P., & Nardon, S. (2015). 3-D stratigraphic architecture, sedimentary processes and controlling factors of Cretaceous deep-water resedimented carbonates (Gargano Peninsula, SE Italy). Sedimentary Geology, 317, 116-136.

Halliday, D., Resnick, R., & Walker, J., (2013). Fundamentals of physics. John Wiley & Sons.

Han, D. H., Liu, J., and Batzle, M., (2006). Acoustic property of heavy oil—measured data. In SEG Technical Program Expanded Abstracts 1903-1907. doi:10.1190/1.2369898

Han, D. H., Liu, J., and Batzle, M., (2007). Shear velocity as the function of frequency in heavy oils. In SEG Technical Program Expanded Abstracts 1716-1719. doi:10.1190/1.2792824.

Han, D. H., Liu, J., and Baztle, M., (2008). Seismic properties of heavy oils—Measured data. The Leading Edge, 27 (9), 1108-1115. doi:10.1190/1.2978972.

Hantschel, T., & Kauerauf, A. I. (2009). Fundamentals of basin and petroleum systems modelling. Springer Science & Business Media.

Hayman, N.W., (2006). Shallow crustal rocks from the Black Mountains detachments, Death Valley, CA. J. Struct. Geol. 28, 1767–1784.

Heap, M. J., & Faulkner, D. R. (2008). Quantifying the evolution of static elastic properties as crystalline rock approaches failure. International Journal of Rock Mechanics and Mining Sciences, 45(4), 564-573.

Heap, M. J., Faulkner, D. R., Meredith, P. G., & Vinciguerra, S. (2010). Elastic moduli evolution and accompanying stress changes with increasing crack damage: implications for stress changes around fault zones and volcanoes during deformation. Geophysical Journal International, 183(1), 225-236.

Heap, M. J., Baud, P., Meredith, P. G., Vinciguerra, S., Bell, A. F., & Main, I. G. (2011). Brittle creep in basalt and its application to time-dependent volcano deformation. Earth and Planetary Science Letters, 307(1-2), 71-82.

Heap, M.J., Baud, P., Meredith, P.G., Vinciguerra, S., Reuschlé, T., (2014). The permeability and elastic moduli of tuff from Campi Flegrei, Italy: Implications for ground deformation modelling. Solid Earth 5, 25–44. https://doi.org/10.5194/se-5-25-2014

Heap, M. J., Villeneuve, M., Kushnir, A. R., Farquharson, J. I., Baud, P., & Reuschlé, T. (2019). Rock mass strength and elastic modulus of the Buntsandstein: an important lithostratigraphic unit for geothermal exploitation in the Upper Rhine Graben. Geothermics, 77, 236-256.

Hinkle, A., and Batzle, M., (2006). Heavy oils: A worldwide overview. The Leading Edge, 25 (6), 742-749. doi:10.1190/1.2210073.

Hobbs, D. W. (1967). The formation of tension joints in sedimentary rocks: an explanation. Geol. Mag, 104(6), 550-556.

Iadanza, A., Sampalmieri, G., Cipollari, P., (2015). Deep-seated hydrocarbons in the seep “Brecciated Limestones” of the Maiella area (Adriatic foreland basin): Evaporitic sealing and oil re-mobilization effects linked to the drawdown of the Messinian Salinity Crisis. Mar. Pet. Geol. 66, 177–191. https://doi.org/10.1016/j.marpetgeo.2015.03.006

Ikari, M. J., Saffer, D. M., & Marone, C., (2009). Frictional and hydrologic properties of clay-rich fault gouge. Journal of Geophysical Research: Solid Earth, 114(B5).

Ikari, M. J., C. Marone, and D. M. Saffer, (2011), On the relation between fault strength and frictional stability, Geology, 39, 83–86, doi:10.1130/G31416.1.

Improta, L., Bagh, S., De Gori, P., Valoroso, L., Pastori, M., Piccinini, D., …Buttinelli, M. (2017). Reservoir structure and wastewater-induced seismicity at the Val d'Agri oilfield (Italy) shown by three-dimensional Vp and Vp/Vs local earthquake tomography. Journal of Geophysical Research: Solid Earth, 122. https://doi.org/10.1002/2017JB014725

Jaeger, J.C., John C., Cook, N.G.W., Zimmerman, R.W., (2007). Fundamentals of rock mechanics, Blackwell Publishing. Blackwell Pub.

Javanbakhti, A., Lines, L. R., and Gray, D., (2018). Analysis of temperature dependency of elastic moduli in heavy oil deposits. The Leading Edge, 37 (5), 372-380. doi:10.1190/tle37050372.1.

Jefferies, S.P., Holdsworth, R.E., Wibberley, C.A.J., Shimamoto, T., Spiers, C.J., Niemeier, A.R., Lloyd, G.E., (2006). The nature and importance of phyllonite development in crustal-scale fault cores: an example from the Median Tectonic Line, Japan. J. Struct. Geol. 28, 220–235.

Jones, D. M., Head, I. M., Gray, N. D., Adams, J. J., Rowan, A. K., Aitken, C. M., ... & Oldenburg, T. (2008). Crude-oil biodegradation via methanogenesis in subsurface petroleum reservoirs. Nature, 451(7175), 176-180.

Kaduri, M., Gratier, J.P., Renard, F., Çakir, Z., Lasserre, C., (2017). The implications of fault zone transformation on aseismic creep: example of the North Ana- tolian Fault, Turkey. J. Geophys. Res., Solid Earth 122. https://doi.org/10.1002/ 2016JB013803.

Kato, A., Onozuka S., and Nakayama T., (2008). Elastic property changes in a bitumen reservoir during steam injection: The Leading Edge, 27, 1124– 1131, doi: 10.1190/1.2978974.

Katz B. J., Dittmar E. I., and Ehret G. E. (2000). A geochemical review of carbonate source rocks in Italy. Journal of Petroleum Geology, vol. 23(4), October 2000, pp 399-424

Keranen, K. M., Weingarten, M., Abers, G. A., Bekins, B. A., & Ge, S. (2014). Sharp increase in central Oklahoma seismicity since 2008 induced by massive wastewater injection. Science, 345(6195), 448-451.

Kimura, G., Yamaguchi, A., Hojo, M., Kitamura, Y., Kameda, J., Ujiie, K., Hamada, Y., Hamahashi, M., Hina, S., (2012). Tectonic mélange as fault rock of subduction plate boundary. Tectonophysics 568–569, 25–38. https://doi.org/10.1016/j.tecto.2011.08.025.

Kohli, A. H., & Zoback, M. D. (2013). Frictional properties of shale reservoir rocks. Journal of geophysical research: solid earth, 118(9), 5109-5125.

Lacroix, B., Buatier, M., Labaume, P., Travè, A., Dubois, M., Charpentier, D., Ven- talon, S., Convert-Gaubier, D., (2011). Tectonic and geochemical characterization of thrusting in a foreland basin: example of the South-Pyrenean orogenic wedge (Spain). J. Struct. Geol. 33, 1359–1377. https://doi.org/10.1016/j.jsg.2011.06.006.

Lavenu, A.P.C., Lamarche, J., Salardon, R., Gallois, A., Marié, L., Gauthier, B.D.M., (2014). Relating background fractures to diagenesis and rock physical properties in a platform-slope transect. Example of the Maiella Mountain (central Italy). Mar. Pet. Geol. 51, 2–19. https://doi.org/10.1016/j.marpetgeo.2013.11.012

Lézin, C., Odonne, F., Massonnat, G.J., Escadeillas, G., (2009). Dependence of joint spacing on rock properties in carbonate strata. Am. Assoc. Pet. Geol. Bull. 93, 271–290. https://doi.org/10.1306/09150808023.

Li, H., Zhao, L., Han, D. H., Sun, M., and Zhang, Y., (2016). Elastic properties of heavy oil sands: Effects of temperature, pressure, and microstructure. Geophysics, 81 (4), D453-D464. doi:10.1190/geo2015-0351.1.

Lines, L., Zou, Y., and Embleton, J., (2005a). Reservoir characterization and heavy oil production. CSEG Recorder, 30, 26-29.

Lines, L., Zou, Y., Zhang, A., Hall, K., Embleton, J., Palmiere, B., Reine, C., Bessette, P., Cary, P. and Secord, D., (2005b). Vp/Vs characterization of a heavy-oil reservoir. The Leading Edge, 24 (11), 1134-1136. doi:10.1190/1.2135111

Lipparini, L., Trippetta, F., Ruggieri, R., Brandano, M., and Romi, A., (2018). Oil distribution in outcropping carbonate-ramp reservoirs (Maiella Mountain, Central Italy): Three-dimensional models constrained by dense historical well data and laboratory measurements. AAPG Bulletin, 102 (7), 1273-1298. doi:10.1306/09261717202

Logan, J. M., C. A. Dengo, N. G. Higgs, and Z. Z. Wang, (1992). Fabric of experimental fault zone: Their development and relationship to mechanical behaviour, in Fault Mechanics and Transport Properties of Rocks, edited by B. Evans and T. Wong, pp. 33–67, Elsevier Academic, San Diego, Calif., doi:10.1016/S0074-6142(08)62814-4.

Lucia, F. J., (2007). Carbonate reservoir characterization: An integrated approach. Springer Science & Business Media.

Magoon, L. B., & Dow, W. G. (1994). The petroleum system: chapter 1: Part I. Introduction.

Mair, K., and C. Marone (1999), Friction of simulated fault gouge for a wide range of velocities and normal stresses, J. Geophys. Res., 104(B12), 28, 899–28, 914, doi:10.1029/1999JB900279.

Mao, X. B., Zhang, L. Y., Li, T. Z., & Liu, H. S. (2009). Properties of failure mode and thermal damage for limestone at high temperature. Mining Science and Technology (China), 19(3), 290-294.

Marone, C., Raleigh, C. B., & Scholz, C. H. (1990). Frictional behaviour and constitutive modelling of simulated fault gouge. Journal of Geophysical Research: Solid Earth, 95(B5), 7007-7025.

Marone, C. (1998a), Laboratory-derived friction laws and their application to seismic faulting, Annu. Rev. Earth Planet. Sci., 26, 643–696, doi:10.1146/annurev.earth.26.1.643.

Marone, C., (1998b), The effect of loading rate on static friction and the rate of fault healing during the earthquake cycle, Nature, 391, 69–72.

Masini, M., Bigi, S., Poblet, J., Bulnes, M., Cuia, R.D., Casabianca, D., (2011). Kinematic evolution and strain simulation, based on cross-section restoration, of the Maiella Mountain: an analogue for oil fields in the Apennines (Italy). Geol. Soc. London, Spec. Publ. 349, 25–44. https://doi.org/10.1144/SP349.2

Mattavelli, L., Novelli, L. (1990). Geochemistry and habitat of oils in Italy. American Association of Geochemistry and habitat of oils in Italy. American Association of Petroleum Geologists Bulletin. Bulletin V. 74. No. 10 (1990), pp. 1623·1639.

Mauldon, M., & Mauldon, J. G. (1997). Fracture sampling on a cylinder: from scanlines to boreholes and tunnels. Rock Mechanics and Rock Engineering, 30(3), 129-144.

Mavko, G., Mukerji, T., Dvorkin, J., (2009). The rock physics handbook : tools for seismic analysis of porous media. Cambridge University Press.

McCormack, M. D., Dunbar, J. A., and Sharp, W. W., (1984). A case study of stratigraphic interpretation using shear and compressional seismic data. Geophysics, 49 (5), 509-520. doi:10.1190/1.1441686

McGinnis, R. N., Ferrill, D. A., Morris, A. P., Smart, K. J., & Lehrmann, D. (2017). Mechanical stratigraphic controls on natural fracture spacing and penetration. Journal of Structural Geology, 95, 160-170.

Mehrgini B., Memarian H., Dusseault M. B., Eshraghi H., Goodarzi B., Ghavidel A. & Hassanzadeh M., (2016). "Geomechanical characterization of a south Iran carbonate reservoir rock at ambient and reservoir temperatures." Journal of Natural Gas Science and Engineering, 34, 269-279. doi.org/10.1016/j.jngse.2016.06.069

Mercuri, M.; Scuderi, M.; Tesei, T.; Carminati, E.; Collettini, C. (2018), Strength evolution of simulated carbonate bearing faults: The role of normal stress and slip velocity. J. Struct. Geol. 2018, 109, 1–9.

Meyer, R. F., Attanasi, E. D., and Freeman, P. A., (2007). Heavy oil and natural bitumen resources in geological basins of the world (No. 2007-1084). US Geological Survey.

Michie, E.A.H., Haines, T.J., (2016). Variability and heterogeneity of the petrophysical properties of extensional carbonate fault rocks , Malta. Pet. Geosci. 22, 136–152. https://doi.org/10.1144/petgeo2015-027

Miller, S.A., Collettini, C., Chiaraluce, L., Cocco, M., Barchi, M.R., Kaus, B.J.P., (2004). Aftershocks driven by a high-pressure CO2 source at depth. Nature 427, 724–727- http://dx.doi.org/10.1038/nature02251.

Mirabella, F., Barchi, M.R., Lupattelli, A., Stucchi, E., Ciaccio, M.G., (2008). Insights on the seismogenic layer thickness from the upper crust structure of the Umbria-Marche Apennines (central Italy). Tectonics 27. http://dx.doi.org/10.1029/2007tc002134.

Mochinaga, H., Onozuka, S., Kono, F., Ogawa, T., Takahashi, A., and Torigoe, T., (2006). Properties of Oil sands and Bitumen in Athabasca. In The Canadian Society of Exploration Geologists CSPG–CSEG–CWLS Convention, 39-44.

Montone, P., & Mariucci, M. T. (2016). The new release of the Italian contemporary stress map. Geophysical Journal International, 205(3), 1525-1531.

Moore, D. E., & Lockner, D. A. (2004). Crystallographic controls on the frictional behaviour of dry and water-saturated sheet structure minerals. Journal of Geophysical Research, 109, B03401. https://doi.org/10.1029/2003JB002582

Moore, D. E., and D. A. Lockner (2011), Frictional strengths of talc-serpentine and talc-quartz mixtures, J. Geophys. Res., 116, B01403, doi:10.1029/2010JB007881.

Moretti, I. (1998). The role of faults in hydrocarbon migration. Petroleum Geoscience, 4(1), 81-94.

Morrow, C. A., B. Radney, and J. Byerlee (1992), Frictional strength and he effective pressure law of montmorillonite and illite clays, in Fault Mechanics And Transport Properties of Rocks, pp. 69–88, Academic, San Diego, Calif.

Morrow, C. A., D. E. Moore, and D. A. Lockner (2000), The effect of mineral bond strength and adsorbed water on fault gouge frictional strength, Geophys. Res. Lett., 27(6), 815–818, doi:10.1029/1999GL008401.

Mutti, M., & Bernoulli, D. (2003). Early marine lithification and hardground development on a Miocene ramp (Maiella, Italy): key surfaces to track changes in trophic resources in nontropical carbonate settings. Journal of Sedimentary Research, 73(2), 296-308.

Nicolas, A., Fortin, J., Regnet, J.B., Dimanov, A., Geguen, Y., (2016). Brittle and semi-brittle behaviours of a carbonate rock: Influence of water and temperature. Geophys. J. Int. 206, 438–456. https://doi.org/10.1093/gji/ggw154

Niemeijer, A.R., Spiers, C.J., (2006). Velocity dependence of strength and healing behaviour in simulated phyllosilicate-bearing fault gouge. Tectonophysics 427, 231–253. http://dx.doi.org/10.1016/j.tecto.2006.03.048.

Niemeijer, A., Marone, C., & Elsworth, D. (2010). Fabric induced weakness of tectonic faults. Geophysical Research Letters, 37(3).

Nur, A., Tosaya, C., & Vo-Thanh, D., (1984). Seismic monitoring of thermal enhanced oil recovery processes. In SEG Technical Program Expanded Abstracts 337-340.

Okamoto, A. S., Verberne, B. A., Niemeijer, A. R., Takahashi, M., Shimizu, I., Ueda, T., & Spiers, C. J. (2019). Frictional properties of simulated chlorite gouge at hydrothermal conditions: Implications for subduction megathrusts. Journal of Geophysical Research: Solid Earth, 124, 4545–4565. https://doi.org/10.1029/ 2018JB017205

Okamoto, A. S., Niemeijer, A. R., Takeshita, T., Verberne, B. A., & Spiers, C. J. (2020). Frictional properties of actinolite-chlorite gouge at hydrothermal conditions. Tectonophysics, 779, 228377.

Orellana, L. F., Scuderi, M. M., Collettini, C., & Violay, M. (2018). Frictional properties of Opalinus Clay: Implications for nuclear waste storage. Journal of Geophysical Research: Solid Earth, 123, 157–175. https://doi.org/10.1002/2017JB014931

Patacca, E., Scandone, P., Di Luzio, E., Cavinato, G.P., Parotto, M., (2008). Structural architecture of the central Apennines: Interpretation of the CROP 11 seismic profile from the Adriatic coast to the orographic divide. Tectonics 27, 1–36. https://doi.org/10.1029/2005TC001917

Peacock, S.M., Christensen, N.I., Bostock, M.G., Audet, P., (2011). High pore pressures and porosity at 35 km depth in the Cascadia subduction zone. Geology 39, 471–474. https://doi.org/10.1130/G31649.1

Pepper, A. S., & Corvi, P. J. (1995). Simple kinetic models of petroleum formation. Part I: oil and gas generation from kerogen. Marine and petroleum geology, 12(3), 291-319.

Peters, K. E., Curry, D. J., & Kacewicz, M. (2012). An overview of basin and petroleum system modelling: Definitions and concepts.

Pytte, A. M., & Reynolds, R. C. (1989). The thermal transformation of smectite to illite. In Thermal history of sedimentary basins (pp. 133-140). Springer, New York, NY.

Rabbani, A., Schmitt, D. R., Kofman, R., and Nycz, J., (2014). Laboratory studies of the seismic properties of bitumen saturated Grosmont carbonates. GeoConvention 2014.

Rabbani, A., Ong, O., Chen, X., Schmitt, D., Nycz, J., and Gray, K., (2016). Rock physics laboratory experiments on bitumen-saturated carbonates from the Grosmont Formation, Alberta. In SEG Technical Program Expanded Abstracts 3464-3467. doi:10.1190/segam2016-13972165.1

Rabbani, A., Schmitt, D. R., Nycz, J., and Gray, K., (2017). Pressure and temperature dependence of acoustic wave speeds in bitumen-saturated carbonates: Implications for seismic monitoring of the Grosmont Formation. Geophysics, 82 (5), MR133-MR151. doi:10.1190/geo2016-0667.1

Rabbani, A., & Schmitt, D. R., (2018). Ultrasonic shear wave reflectometry applied to the determination of the shear moduli and viscosity of a viscoelastic bitumen. Fuel, 232, 506-518.

Rabbani, A., and Schmitt, D. R., (2019). The Longitudinal Modulus of Bitumen: Pressure and Temperature Dependencies. Geophysics, 84 (4), 1-56.

Rabinowitz, H. S., Savage, H. M., Skarbek, R. M., Ikari, M. J., Carpenter, B. M., & Collettini, C. (2018). Frictional behaviour of input sediments to the Hikurangi Trench, New Zealand. Geochemistry, Geophysics, Geosystems, 19(9), 2973-2990.

Rajabzadeh, M.A., Moosavinasab, Z., Rakhshandehroo, G., Neyriz, T., (2012). Effects of Rock Classes and Porosity on the Relation between Uniaxial Compressive Strength and Some Rock Properties for Carbonate Rocks 113–122. https://doi.org/10.1007/s00603-011-0169-y

Reinen, L.A. & Weeks, J.D., (1993). Determination of rock friction constitutive parameters using an iterative least-squares inversion method, J. geophys. Res., 98, 15 937–15 950.

Renard, F., Ortoleva, P., Gratier, J.P. (1997) Pressure solution in sandstones: influence of clays and dependence on temperature and stress. Tectonophysics 280:257–266

Risnes, R., Madland, M. V., Hole, M., Kwabiah, N.K., (2005). Water weakening of chalk - Mechanical effects of water-glycol mixtures. J. Pet. Sci. Eng. 48, 21–36. https://doi.org/10.1109/MAP.2007.4395340

Ronchi, P., Di Giulio, A., Ceriani, A., & Scotti, P. (2010). Contrasting fluid events giving rise to apparently similar diagenetic products; late-stage dolomite cements from the Southern Alps and central Apennines, Italy. Geological Society, London, Special Publications, 329(1), 397-413.

Ruggieri, R., & Trippetta, F. (2020). Petrophysical properties variation of bitumen-bearing carbonates at increasing temperatures from laboratory to model. Geophysics, 85(5), 1-52.

Ruggieri, R., Scuderi, M. M., Tinti, E., Trippetta, F., Collettini, C., Brignoli, M., Mantica, S., Petroselli, S., Osculati, L. & Volonté, G. (2021). Effects of illite content on frictional properties of experimental carbonate faults. Tectonophysics (in press).

Ruina, A. (1983), Slip instability and state variable friction laws, J. Geophys. Res., 88, 10, 359–10, 370. doi:10.1029/JB088iB12p10359.

Rusciadelli, G. (2005). Provenance of Upper Pliocene conglomerates of the Mutignano Formation (Abruzzo, Italy): implications for unraveling the uplift history of the Central Apennines external zones. Bollettino della Società geologica italiana, 124(3), 645-659.

Rustichelli, A., Torrieri, S., Tondi, E., Laurita, S., Strauss, C., Agosta, F., Balsamo, F., (2016). Fracture characteristics in Cretaceous platform and overlying ramp carbonates: An outcrop study from Maiella Mountain (central Italy). Mar. Pet. Geol. 76, 68–87. https://doi.org/10.1016/j.marpetgeo.2016.05.020

Saffer, D., K. Frye, C. Marone, and K. Mair (2001), Laboratory results indicating complex and potentially unstable frictional behaviour of smectite clay, Geophys. Res. Lett., 28, 2297–2300, doi:10.1029/2001GL012869.

Saffer, D. M., and C. Marone (2003), Comparison of smectite- and illite-rich gouge frictional properties: Application to the updip limit of the seismogenic zone along subduction megathrusts, Earth Planet. Sci. Lett., 215, 219–235. doi:10.1016/S0012-821X(03)00424-2.

Sayers, C.M., (2008). The elastic properties of carbonates. Lead. Edge August, 1020–1024.

Schmitt, D. R., (1999). Seismic attributes for monitoring of a shallow heated heavy oil reservoir: A case study. Geophysics, 64 (2), 368-377. doi:10.1190/1.1444541

Scisciani, V., Tavarnelli, E., & Calamita, F. (2002). The interaction of extensional and contractional deformations in the outer zones of the Central Apennines, Italy. Journal of Structural Geology, 24(10), 1647-1658.

Scrocca, D., Brandano, M., Petracchini, L., Lipparini, L., (2013). Analysis of an Exhumed Oil Accumulation: the Oligo-Miocene Carbonate Ramp Deposits of the Majella Mountain (Central Italy), AAPG-ER Newsletter.

Scuderi, M. M., & Collettini, C. (2018). Fluid injection and the mechanics of frictional stability of shale-bearing faults. Journal of Geophysical Research: Solid Earth, 123(10), 8364-8384.

Sibson, R.H., (1977). Fault rocks and fault mechanisms. J. Geol. Soc. 133, 191–213. http://dx.doi.org/10.1144/gsjgs.133.3.0191.

Smeraglia, L., Trippetta, F., Carminati, E., Mollo, S., (2014). Tectonic control on the petrophysical properties of foredeep sandstone in the Central Apennines, Italy. J. Geophys. Res. Solid Earth 119, 9077–9094. https://doi.org/10.1002/2014JB011221.

Smeraglia, L., Billi, A., Carminati, E., Cavallo, A., Di Toro, G., Spagnuolo, E., & Zorzi, F. (2017). Ultra-thin clay layers facilitate seismic slip in carbonate faults. Scientific reports, 7(1), 1-10.

Smith, S.A.F., Billi, A., Di Toro, G., Spiess, R., (2011). Principal slip zones in limestone: microstructural characterization and implications for the seismic cycle (tre Monti fault, central Apennines, Italy). Pure Appl. Geophys. 168, 2365–2393. http://dx.doi.org/10.1007/s00024-011-0267-5.

Solum, G.S., van der Pluijm, B.A., (2009). Quantification of fabrics in clay gouge from the Carboneras fault, Spain and implications for fault behaviour. Tectono-physics 475, 554–562. https://doi .org /10 .1016 /j.tecto .2009 .07.006.

Stanchits, S., Mayr, S., Shapiro, S., Dresen, G., (2011). Fracturing of porous rock induced by fluid injection. Tectonophysics 503, 129–145. https://doi.org/10.1016/j.tecto.2010.09.022

Sweeney, J. J., & Burnham, A. K. (1990). Evaluation of a simple model of vitrinite reflectance based on chemical kinetics. AAPG bulletin, 74(10), 1559-1570.

Tatham, R. H., and Stoffa, P. L., (1976). Vp/Vs- A potential hydrocarbon indicator. Geophysics, 41 (5), 837-849. doi:10.1190/1.1440668

Tembe, S., D. A. Lockner, and T.-F. Wong (2010), Effect of clay content and mineralogy on frictional sliding behaviour of simulated gouges: Binary and ternary mixtures of quartz, illite, and montmorillonite, J. Geophys. Res., 115, B03416, doi:10.1029/2009JB006383.

Terzaghi, R. D. (1965). Sources of error in joint surveys. Geotechnique, 15(3), 287-304.

Tesei, T., C. Collettini, B. M. Carpenter, C. Viti, and C. Marone (2012), Frictional strength and healing behaviour of phyllosilicate-rich faults, J. Geophys. Res., 117, B09402, doi:10.1029/2012JB009204.

Tesei, T., Collettini, C., Viti, C., Barchi, M.R., (2013). Fault architecture and deformation mechanisms in exhumed analogues of seismogenic carbonate-bearing thrusts. J. Struct. Geol. 55. https://doi .org /10 .1016 /j.jsg .2013 .07.007.

Tesei, T., Collettini, C., Barchi, M. R., Carpenter, B. M., & Di Stefano, G., (2014). Heterogeneous strength and fault zone complexity of carbonate-bearing thrusts with possible implications for seismicity. Earth and Planetary Science Letters, 408, 307-318.

Tesei, T., Lacroix, B., Collettini, C., (2015). Fault strength in thin-skinned tectonic wedges across the smectite-illite transition: constraints from friction experi- ments and critical tapers. Geology. https://doi.org/10.1130/G36978.1.

Tosaya, C., Nur, A., Vo-Thanh, D., and Da Prat, G., (1987). Laboratory seismic methods for remote monitoring of thermal EOR. SPE Reservoir Engineering, 2 (02), 235-242. doi:10.2118/12744-PA

Trippetta, F., Collettini, C., Vinciguerra, S., Meredith, P.G., (2010). Laboratory measurements of the physical properties of Triassic Evaporites from Central Italy and correlation with geophysical data. Tectonophysics 492, 141–149.

Trippetta, F., Collettini, C., Meredith, P. G., & Vinciguerra, S. (2013). Evolution of the elastic moduli of seismogenic Triassic Evaporites subjected to cyclic stressing. Tectonophysics, 592, 67-79.

Trippetta, F., & Geremia, D., (2019). The seismic signature of heavy oil on carbonate reservoir through laboratory experiments and AVA modelling. Journal of Petroleum Science and Engineering, 177, 849-860. doi:10.1016/j.petrol.2019.03.002

Trippetta, F., Ruggieri, R., Brandano, M., & Giorgetti, C. (2020). Petrophysical properties of heavy oil-bearing carbonate rocks and their implications on petroleum system evolution: Insights from the Majella Massif. Marine and Petroleum Geology, 111, 350-362. doi:10.1016/j.marpetgeo.2019.08.035

Valoroso, L., Chiaraluce, L., Collettini, C., (2014). Earthquakes and fault zone structure. Geology 42, 343–346. http://dx.doi.org/10.1130/g35071.1.

Vannucchi, P., Spagnuolo, E., Aretusini, S., Di Toro, G., Ujiie, K., Tsutsumi, A., & Nielsen, S. (2017). Past seismic slip-to-the-trench recorded in Central America megathrust. Nature Geoscience, 10(12), 935–940. https://doi.org/10.1038/s41561-017-0013-4

Vecsei, A., Sanders, D. G., Bernoulli, D., Eberli, G. P., & Pignatti, J. S., (1998). Cretaceous to Miocene sequence stratigraphy and evolution of the Maiella carbonate platform margin, Italy. SEMP special Publication, 60, pp 53-73.

Verberne, B.A., He, C., Spiers, C.J., 2010. Frictional properties of sedimentary rocks and natural fault gouge from the Longmenshan Fault Zone, Sichuan, China. Bull. Seismol. Soc. Am.100, 2767–2790.

Verberne, B.A., De Bresser, J.H.P., Niemeijer, A.R. & Spiers, C.J., (2015), Mechanical behaviour and microstructure of simulated calcite fault gouge sheared at 20–600 ◦C: implications for natural faults in limestones, J. geophys. Res., doi:10.1002/2015JB012292.

Vezzani L., and Ghisetti F. (1998). Carta geologica dell'Abruzzo 1:100.000Firenze.

Vezzani, L., Festa, A., Ghisetti, F.C., (2010). Geology and tectonic evolution of the Central-Southern Apennines, Italy, Special Paper of the Geological Society of America. https://doi.org/10.1130/2010.2469

Viti C and Collettini C. (2009). Growth and deformation mechanisms of talc along a natural fault: a micro/nanostructural investigation. Contributions to Mineralogy and Petrology, vol. 158; p. 529-542, ISSN: 0010-7999.

Viti, C., Collettini, C., Tesei, T., (2014). Pressure solution seams in carbonatic fault rocks: mineralogy, micro/nanostructures and deformation mechanism. Contrib. Mineral. Petrol. 167. http://dx.doi.org/10.1007/s00410-014-0970-1.

Vrolijk, P., and B. A. van der Pluijm (1999), Clay gouge, J. Struct. Geol., 21, 1039–1048, doi:10.1016/S0191-8141(99)00103-0.

Wang, Z., & Nur, A., (1988). Effect of Temperature on Wave Velocities in Sands and Sandstones With Heavy Hydrocarbons. SPE Reservoir Engineering, 3 (01), 158-164. doi:10.2118/15646-PA.

Wintsch, R. P., Christoffersen, R., & Kronenberg, A. K. (1995). Fluid-rock reaction weakening of fault zones. Journal of Geophysical Research: Solid Earth, 100(B7), 13021-13032.

Wolf, K., (2010). Laboratory measurements and reservoir monitoring of bitumen-sand reservoir: Ph.D. Thesis, Stanford University.

Yuan, H., Han, D. H., & Zhang, W. (2015a). Heavy oil sands measurement and rock-physics modelling. Geophysics, 81 (1), D57-D70. doi:10.1190/GEO2014-0573.1

Yuan, H., Han, D. H., & Zhang, W., (2015b). The Effect of Pressure and Temperature on Bitumen Saturated Carbonate. In SEG Technical Program Expanded Abstracts 3151-3155. doi.org/10.1190/segam2015-5907385.1

Yuan, H., Han D., Li H., and Zhang W., (2017). A comparison of bitumen sands and bitumen carbonates: measured data: Geophysics, 82 (1), MR39-MR50. doi:10.1190/geo2015-0657.1

Yuan, H., Han, D. H., Zhao, L., Huang, Q., & Zhang, W., (2018). Rock-physics characterization of bitumen carbonates: A case study. Geophysics, 83 (3), B119-B132. doi:10.1190/geo2017-0319.1

Zappaterra, E. (1990). Carbonate paleogeographic sequences of the Periadriatic Region. Bollettino della Società Geologica Italiana, vol. 109 (1), 5-20.

Zappaterra, E. (1994). Source-rock distribution model of the Periadriatic region. AAPG bulletin, 78(3), 333-354.

Zhao, Y., & Machel, H. G., (2012). Viscosity and other rheological properties of bitumen from the Upper Devonian Grosmont reservoir, Alberta, Canada. AAPG bulletin, 96 (1), 133-153. doi:10.1306/04261110180